ISSN 1997-308X
eISSN 2412-8767

ИЗВЕСТИЯ ВУЗОВ
ПОРОШКОВАЯ МЕТАЛЛУРГИЯ И ФУНКЦИОНАЛЬНЫЕ ПОКРЫТИЯ

POWDER METALLURGY AND FUNCTIONAL COATINGS

2024
Том Vol. 18 № No. 5
powder.misis.ru

ISSN 1997-308X
eISSN 2412-8767

POWDER METALLURGY AND FUNCTIONAL COATINGS

Scientific and Technical Journal

Founded in 2007
Six issues per year

2024
Том 18 № 5
Vol. 18 No. 5

ИЗВЕСТИЯ ВУЗОВ
ПОРОШКОВАЯ МЕТАЛЛУРГИЯ И ФУНКЦИОНАЛЬНЫЕ ПОКРЫТИЯ

Научно-технический журнал

Основан в 2007 г.
Выходит 6 раз в год

POWDER METALLURGY AND FUNCTIONAL COATINGS

Scientific and Technical Journal
Founded in 2007
Six issues per year

http://powder.misis.ru

ISSN 1997-308X
eISSN 2412-8767

Founder: MISIS University of Science and Technology

National University of Science and Technology "MISIS"
Address: 1 Bld, 4 Leninskiy Prosp., Moscow 119049, Russian Federation
http://www.misis.ru

Editor-in-Chief

Evgeny A. Levashov
Prof., Dr. Sci. (Eng.), Acad. of the RANS, NUST MISIS, Moscow, Russian Federation

Journal is included into the List of peer-reviewed scientific publications recommended by the Highest Attestation Commission of the Ministry of Education and Science of the Russian Federation for publishing the results of doctoral and candidate dissertations. Abstracting/Indexing: Scopus, Russian Science Citation Index (RSCI), Ulrich's Periodicals Directory, VINITI Database (Abstract Journal).

Editorial Board

M. I. Alymov – Dr. Sci. (Eng.), Corresponding Member of the RAS, Merzhanov Institute of Structural Macrokinetics and Materials Sciences of the RAS, Chernogolovka, Russia
A. P. Amosov – Prof., Dr. Sci. (Phys.-Math.), Samara State Technical University, Samara, Russia
G. A. Bagliuk – Prof., Dr. Sci. (Eng.), Acad. of the NASU, IPMS NASU, Kiev, Ukraine
I. V. Blinkov – Prof., Dr. Sci. (Eng.), NUST MISIS, Moscow, Russia
M. V. Chukin – Prof., Dr. Sci. (Eng.), Magnitogorsk State Technical University, Magnitogorsk, Russia
H. Danninger – Prof., Dr. Sci., Vienna University of Technology, Vienna, Austria
B. Derin – Assoc. Prof., Dr. Sci. (Phil.), Istanbul Technical University, Maslak, Istanbul, Turkey
V. Yu. Dorofeyev – Prof., Dr. Sci. (Eng.), South-Russian State Polytechnical University (NPI), Novocherkassk, Russia
Yu. Estrin – Prof., Dr. Sci. (Nat.), Monash University, Clayton, Australia
A. Ph. Ilyushchanka – Prof., Dr. Sci. (Eng.), Acad. of the NAS of Belarus, State Research and Production Powder Metallurgy Association, Minsk, Belarus
Yu. R. Kolobov – Prof., Dr. Sci. (Phys.-Math.), Federal Research Center of Problems of Chemical Pfysics and Medicinal Chemistry of the RAS, Chernogolovka, Russia
V. S. Komlev – Prof., Dr. Sci. (Eng.), Corresponding Member of the RAS, Institute of Metallurgy of the RAS, Moscow, Russia
I. Konyashin – Prof., Dr. Sci. (Econ.), Element Six GmbH, Burghaun, Germany
Yu. M. Korolyov – Prof., Dr. Sci. (Eng.), Scientific and Technical Association "Powder Metallurgy", Moscow, Russia
D. Yu. Kovalev – Dr. Sci. (Phys.-Math.), Merzhanov Institute of Structural Macrokinetics and Materials Sciences of the RAS, Chernogolovka, Russia
S. A. Kulinich – Assoc. Prof., PhD (Chem.), Tokai University, Hiratsuka, Kanagawa, Japan
S. V. Kuzmin – Prof., Dr. Sci. (Eng.), Corresponding Member of the RAS, Volgograd State Technical University, Volgograd, Russia
V. P. Kuznetsov – Prof., Dr. Sci. (Eng.), Ural Federal University, Ekaterinburg, Russia
Yu. V. Levinsky – Prof., Dr. Sci. (Eng.) Merzhanov Institute of Structural Macrokinetics and Materials Sciences of the RAS, Chernogolovka, Russia
A. E. Ligachyov – Prof., Dr. Sci. (Phys.-Math.), Prokhorov General Physics Institute of the RAS, Moscow, Russia
V. Yu. Lopatin – Cand. Sci., NUST MISIS, Moscow, Russia
A. A. Lozovan – Prof., Dr. Sci (Eng.), Moscow Aviation Institute (NRU), Moscow, Russia
V. I. Lysak – Prof., Dr. Sci. (Eng.), Acad. of the RAS, Volgograd State Technical University, Volgograd, Russia
A. V. Makarov – Dr. Sci. (Eng.), Corresponding Member of the RAS, M.N. Mikheev Institute of Metal Physics of the Ural Branch of the RAS, Ural Federal University, Ekaterinburg, Russia
L. L. Mishnaevsky – Dr. Habil. (Eng.), Technical University of Denmark, Roskilde, Denmark
A. S. Mukasyan – Prof., Dr. Sci. (Phys.-Math.), University of Notre Dame, Notre Dame, USA
S. A. Oglezneva – Prof., Dr. Sci. (Eng.), Perm National Research Polytechnical University, Perm, Russia
R. Orrù – Prof., Dr. Sci. (Eng.), University of Cagliari, Cagliari, Italy
I. B. Panteleev – Prof., Dr. Sci. (Eng.), St. Petersburg State Technological Institute (Technical University), St. Petersburg, Russia
F. Peizhong – Prof., Dr. Sci., China University of Mining and Technology, Xuzhou, P.R. China
C. Pengwan – Prof., Dr. Sci., Beijing Institute of Technology, Beijing, P.R. China
M. I. Petrzhik – Dr. Sci. (Eng.), NUST MISIS, Moscow, Russia
Yu. S. Pogozhev – Assoc. Prof., Cand. Sci. (Eng.), NUST MISIS, Moscow, Russia
V. V. Polyakov – Prof., Dr. Sci. (Phys.-Math.), Altai State University, Barnaul, Russia
A. A. Popovich – Prof., Dr. Sci. (Eng.)., Corresp. Member of the RANS, St. Petersburg State Polytechnical University (National Research University), St. Petersburg, Russia
S. E. Porozova – Dr. Sci. (Eng.), Perm National Research Polytechnical University, Perm, Russia
A. A. Rempel – Prof., Dr. Sci. (Phys.-Math.), Acad. of the RAS, Institute of Metallurgy of the Ural Branch of the RAS, Ekaterinburg, Russia
F. Rustichelli – Prof., Dr. Sci. (Phys.), University of Marches, Ancona, Italy
S. D. Shlyapin – Prof., Dr. Sci. (Eng.), Moscow Aviation Institute (NRU), Moscow, Russia
D. V. Shtansky – Prof., Dr. Sci. (Phys.-Math.), NUST MISIS, Moscow, Russia
A. N. Timofeev – Dr. Sci. (Eng.), JSC "Komposite", Korolev, Russia
P. A. Vityaz' – Prof., Dr. Sci. (Eng.), Acad. of the NAS of Belarus, Minsk, Belarus
A. A. Zaitsev – Assoc. Prof., Cand. Sci. (Eng.), NUST MISIS, Moscow, Russia
Zheng YongTing – Prof., Dr. Sci., Harbin Institute of Technology, Harbin, P.R. China
F. Zhengyi – Prof., Dr. Sci., Wuhan University of Technology, Wuhan, P.R. China

Editorial Staff

Address: NUST MISIS,
1 Bld, 4 Leninskiy Prosp., Moscow 119049, Russian Federation

Phone: +7 (495) 638-45-35. ***E-mail:*** izv.vuz@misis.ru

Certificate of registration **No. FS77-27955** (12.04.2007)
Re-registration **PI No. FS77-79230** (25.09.2020)

Leading Editor: A.A. Kudinova
Executive Editor: O.V. Sosnina
Layout Designer: V.V. Rasenets

Signed print 21.10.2024. Format 60×90 $^1/_8$
Offset paper No. 1. Digital printing. Quires 9.25
Order 20702. Free price
Printed in the printing house of the MISIS Publish House
1 Bld, 4 Leninskiy Prosp., Moscow, 119049 Russian Federation
Phone/fax: +7 (499) 236-76-17

PM & FC © NUST MISIS, Moscow, 2024

Articles are available under Creative Commons Attribution Non-Commercial No Derivatives

ИЗВЕСТИЯ ВУЗОВ ПОРОШКОВАЯ МЕТАЛЛУРГИЯ И ФУНКЦИОНАЛЬНЫЕ ПОКРЫТИЯ

Научно-технический журнал
Основан в 2007 г.
Выходит 6 раз в год

http://powder.misis.ru

ISSN 1997-308X
eISSN 2412-8767

Учредитель: МИСИС
УНИВЕРСИТЕТ НАУКИ И ТЕХНОЛОГИЙ

ФГАОУ ВО Национальный исследовательский технологический университет «МИСИС»
Адрес: 119049, Москва, Ленинский пр-т, 4, стр. 1
https://www.misis.ru

Главный редактор

Евгений Александрович Левашов
д.т.н., академик РАЕН, профессор, НИТУ МИСИС, г. Москва

Журнал включен в Перечень рецензируемых научных изданий, рекомендованных ВАК Минобрнауки РФ
для публикации результатов диссертаций на соискание ученых степеней.
Журнал включен в базы данных: Scopus, Russian Science Citation Index (RSCI), Ulrich's Periodicals Directory, РИНЦ, БД/РЖ ВИНИТИ.

Редакционная коллегия

М. И. Алымов – д.т.н., чл.-корр. РАН, проф., ИСМАН, г. Черноголовка
А. П. Амосов – д.ф.-м.н., проф., СамГТУ, г. Самара
Г. А. Баглюк – д.т.н., акад. НАНУ, проф., ИПМ НАН Украины, г. Киев
И. В. Блинков – д.т.н., проф., НИТУ МИСИС, г. Москва
П. А. Витязь – д.т.н., акад. НАНБ, проф., НАН Беларуси, г. Минск
В. Ю. Дорофеев – д.т.н., проф., ЮРГПУ (НПИ), г. Новочеркасск
А. А. Зайцев – к.т.н., доц., НИТУ МИСИС, г. Москва
А. Ф. Ильющенко – д.т.н., акад. НАН Беларуси, проф., ГНПО ПМ НАН Беларуси, г. Минск
Д. Ю. Ковалев – д.ф.-м.н., ИСМАН, г. Черноголовка
Ю. Р. Колобов – д.ф.-м.н., проф., ФИЦ ПХФ и МХ РАН, г. Черноголовка
В. С. Комлев – д.т.н., чл.-корр. РАН, проф., ИМЕТ РАН, г. Москва
Ю. М. Королев – д.т.н., проф., НТА «Порошковая металлургия», г. Москва
В. П. Кузнецов – д.т.н., проф., УрФУ, г. Екатеринбург
С. В. Кузьмин – д.т.н., чл.-корр. РАН, проф., ВолгГТУ, г. Волгоград
Ю. В. Левинский – д.т.н., проф., ИСМАН, г. Черноголовка
А. Е. Лигачев – д.ф.-м.н., проф., ИОФ РАН, г. Москва
А. А. Лозован – д.т.н., проф., МАИ (НИУ), г. Москва
В. Ю. Лопатин – к.т.н., доц., НИТУ МИСИС, г. Москва
В. И. Лысак – д.т.н., акад. РАН, проф., ВолгГТУ, г. Волгоград
А. В. Макаров – д.т.н., чл.-корр. РАН, ИФМ УрО РАН, УрФУ, г. Екатеринбург
С. А. Оглезнева – д.т.н., проф., ПНИПУ, г. Пермь
И. Б. Пантелеев – д.т.н., проф., СПбГТИ (ТУ), г. Санкт-Петербург
М. И. Петржик – д.т.н., проф., НИТУ МИСИС, г. Москва
Ю. С. Погожев – к.т.н., доц., НИТУ МИСИС, г. Москва
В. В. Поляков – д.ф.-м.н., проф., АлтГУ, г. Барнаул
А. А. Попович – д.т.н., чл.-корр. РАЕН, проф., СПбГПУ, г. Санкт-Петербург
С. Е. Порозова – д.т.н., проф., ПНИПУ, г. Пермь
А. А. Ремпель – д.ф.-м.н., акад. РАН, проф., ИМЕТ УрО РАН, г. Екатеринбург
А. Н. Тимофеев – д.т.н., АО «Композит», г. Королев
М. В. Чукин – д.т.н., проф., МГТУ, г. Магнитогорск
С. Д. Шляпин – д.т.н., проф., МАИ (НИУ), г. Москва
Д. В. Штанский – д.ф.-м.н., проф., НИТУ МИСИС, г. Москва
H. Danninger – Dr. Sci., Prof., Vienna University of Technology, Vienna, Austria
B. Derin – Dr. Sci. (Phil.), Assoc. Prof., Istanbul Technical University, Maslak, Istanbul, Turkey
Yu. Estrin – Dr. Sci. (Nat.), Prof., Monash University, Clayton, Australia
I. Konyashin – Dr. Sci. (Econ.), Prof., Element Six GmbH, Burghaun, Germany
S. A. Kulinich – PhD (Chem.), Associate Prof., Tokai University, Hiratsuka, Kanagawa, Japan
L. L. Mishnaevsky – Dr. Habil. (Eng.), Technical University of Denmark, Roskilde, Denmark
A. S. Mukasyan – Dr. Sci. (Phys.-Math.), Prof., University of Notre Dame, Notre Dame, USA
R. Orrù – Dr. Sci. (Eng.), Prof., University of Cagliari, Cagliari, Italy
F. Peizhong – Dr. Sci., Prof., China University of Mining and Technology, Xuzhou, P.R. China
C. Pengwan – Dr. Sci., Prof., Beijing Institute of Technology, Beijing, P.R. China
F. Rustichelli – Dr. Sci. (Phys.), Prof., University of Marches, Ancona, Italy
Zheng YongTing – Dr. Sci., Prof., Harbin Institute of Technology, Harbin, P.R. China
F. Zhengyi – Dr. Sci., Prof., Wuhan University of Technology, Wuhan, P.R. China

Редакция журнала

Адрес: 119049, Москва,
Ленинский пр-т, 4, стр. 1. НИТУ МИСИС

Тел.: +7 (495) 638-45-35. ***Эл. почта:*** izv.vuz@misis.ru

Свидетельство о регистрации № **ФС77-27955** от 12.04.2007 г.
Перерегистрация 25.09.2020 г. **ПИ № ФС77-79230**

ПМ и ФП ИЗВЕСТИЯ ВУЗОВ

© НИТУ МИСИС, Москва, 2024

Статьи доступны под лицензией Creative Commons Attribution Non-Commercial No Derivatives

Ведущий редактор: А.А. Кудинова
Выпускающий редактор: О.В. Соснина
Дизайн и верстка: В.В. Расенець

Подписано в печать 21.10.2024. Формат 60×90 $^1/_8$
Бум. офсетная № 1. Печать цифровая. Усл. печ. л. 9,25
Заказ 20702. Цена свободная
Отпечатано в типографии Издательского Дома МИСИС
119049, г. Москва, Ленинский пр-т, 4, стр. 1
Тел./факс: +7 (499) 236-76-17

Contents

Production Processes and Properties of Powders

Refractory, Ceramic, and Composite Materials

Nanostructured Materials and Functional Coatings

Materials and Coatings Fabricated Using the Additive Manufacturing Technologies

Application of Powder Materials and Functional Coatings

Содержание

Процессы получения и свойства порошков

Тугоплавкие, керамические и композиционные материалы

Наноструктурированные материалы и функциональные покрытия

Материалы и покрытия, получаемые методами аддитивных технологий

Применение порошковых материалов и функциональных покрытий

Production Processes and Properties of Powders
Процессы получения и свойства порошков

UDC 621.762

https://doi.org/10.17073/1997-308X-2024-5-5-12

Research article
Научная статья

Structure and magnetic properties of strontium hexaferrite powder after milling in a beater mill in a magnetoliquefied layer followed by annealing

I. N. Egorov[1], N. Ya. Egorov[1], Yu. V. Rusalev[1], S. I. Egorova[2]

[1] **Southern Federal University**
105/42 Bolshaya Sadovaya Str., Rostov-on-Don 344006, Russia
[2] **Don State Technical University**
1 Gagarin Sq., Rostov-on-Don 344000, Russia

siyegorova@gmail.com

Abstract. This study examines the effectiveness of processing dispersed strontium hexaferrite material in a beater mill within a magnetoliquefied layer formed by magnetic fields – an inhomogeneous alternating field with a frequency of 50 Hz and an induction gradient of 90 mT/m, and a constant field with an induction of 15.3 mT – under conditions where milling is accompanied by particle aggregation. The magnetic field lines are mutually perpendicular and parallel to the plane of the milling bodies. A comprehensive investigation of the changes in the dispersed composition and structural characteristics of the strontium hexaferrite powder with increased milling duration was conducted using scanning electron microscopy and *X*-ray diffraction analysis. The results show that processing the strontium hexaferrite dispersed system with an initial average particle size of 1558.5 µm in a magnetoliquefied layer for 120 min does not alter the phase composition of the powder. However, milling reduces the average particle size to 0.57 µm, decreases the size of the coherent scattering regions, increases the lattice microstrain of the $SrFe_{12}O_{19}$ phase, and raises the dislocation density. Magnetic properties of the powder samples before and after annealing were studied using a vibrating sample magnetometer at room temperature and normal atmospheric pressure. The conducted research allows for the assessment of the technological outcomes of processing the dispersed system in a magnetoliquefied layer, considering the collective effects that accompany milling.

Keywords: powder metallurgy, strontium hexaferrite, mechanical milling, *X*-ray diffraction analysis, scanning electron microscopy, vibrating sample magnetometer

For citation: Egorov I.N., Egorov N.Ya., Rusalev Yu.V., Egorova S.I. Structure and magnetic properties of strontium hexaferrite powder after milling in a beater mill in a magnetoliquefied layer followed by annealing. *Powder Metallurgy and Functional Coatings*. 2024;18(5):5–12. https://doi.org/10.17073/1997-308X-2024-5-5-12

Структура и магнитные свойства порошка гексаферрита стронция после измельчения в бильной мельнице в магнитоожиженном слое с последующим отжигом

И. Н. Егоров[1], Н. Я. Егоров[1], Ю. В. Русалев[1], С. И. Егорова[2]

[1] **Южный федеральный университет**
Россия, 344006, г. Ростов-на-Дону, ул. Большая Садовая, 105/42
[2] **Донской государственный технический университет**
Россия, 344000, г. Ростов-на-Дону, пл. Гагарина, 1

siyegorova@gmail.com

Аннотация. В работе рассмотрена эффективность обработки дисперсного материала гексаферрита стронция в бильной мельнице в магнитоожиженном слое, образованном в магнитных полях – неоднородном переменном с частотой 50 Гц, градиентом индукции 90 мТл/м и постоянном с индукцией 15,3 мТл – в условиях, когда измельчение сопровождается агрегацией частиц. Линии магнитной индукции полей взаимно перпендикулярны и параллельны плоскости вращения бил. Методами растровой электронной микроскопии и рентгеноструктурного анализа проведено комплексное исследование особенностей изменения дисперсного состава и структурных характеристик порошка гексаферрита стронция при увеличении продолжительности измельчения. Показано, что при обработке дисперсной системы гексаферрита стронция со средним размером частиц 1558,5 мкм в магнитоожиженном слое в течение 120 мин не происходит изменения фазового состава порошка, измельчение приводит к уменьшению среднего размера частиц порошка до 0,57 мкм, снижению размера областей когерентного рассеяния, увеличению микродеформации решетки фазы $SrFe_{12}O_{19}$ и плотности дислокаций. С помощью вибрационного магнитометра при комнатной температуре и нормальном атмосферном давлении изучены магнитные характеристики порошковых образцов до и после отжига. Проведенные исследования позволяют оценить технологический результат обработки дисперсной системы в магнитоожиженном слое с учетом совокупности основных явлений, сопровождающих измельчение.

Ключевые слова: порошковая металлургия, гексаферрит стронция, механическое измельчение, рентгеноструктурный анализ, растровая электронная микроскопия, вибрационный магнитометр

Для цитирования: Егоров И.Н., Егоров Н.Я., Русалев Ю.В., Егорова С.И. Структура и магнитные свойства порошка гексаферрита стронция после измельчения в бильной мельнице в магнитоожиженном слое с последующим отжигом. *Известия вузов. Порошковая металлургия и функциональные покрытия*. 2024;18(5):5–12. https://doi.org/10.17073/1997-308X-2024-5-5-12

Introduction

Hexagonal ferrites are widely used in powder metallurgy for the production of sintered magnets and magnetoplasts [1; 2]. Compared to barium hexaferrite magnets, strontium ferrite magnets provide superior magnetic properties [3–6]. The quality of the magnetic properties of strontium hexaferrite powder is influenced by the granulometric composition and the degree of uniformity in particle size within the dispersed system [7; 8].

With the increase in the production of permanent magnets, there is also a rise in the amount of waste generated during various technological operations, which needs to be recycled. The recycling process of magnet production waste or used sintered magnets involves stages of milling and powder production [9; 10]. The most common methods for producing fine and ultrafine powders of ferromagnetic materials are wet and dry milling [11–14]. There are also methods to enhance the milling process efficiency by transferring the milled material into a fluidized state [15–17].

The primary goal in producing strontium hexaferrite powder is to obtain a dispersed system with a specified set of physical-technological and structural characteristics. The development of high-performance equipment for milling ferromagnetic materials is of great importance, as the duration of the milling process and the specific energy consumption are crucial economic factors. The efficiency of dispersing can be influenced by changing the conditions under which milling is carried out, particularly by applying alternating inhomogeneous and constant magnetic fields to the dispersed ferromagnetic material in a beater mill, with the magnetic field lines being mutually perpendicular and parallel to the plane of the milling bodies' rotation [18]. Under electromagnetic influence, a magnetoliquefied layer is formed from the dispersed material, where particles and aggregates move within an inhomogeneous alternating magnetic field, ensuring the principle of multiple returns of particles and aggregates to the area of the rotating milling bodies and significantly increasing their collision frequency with the milling bodies. Milling of dispersed media in a magnetoliquefied layer requires additional energy consumption for powering the electromagnets. As the induction of the constant field and the gradient of the alternating magnetic field increase, the energy consumption for power supply also rises. However, only when the induction of the constant magnetic field reaches 15.3 mT and the gradient of the alternating magnetic field reaches 90 mT/m is there intense movement of coarse ferromagnetic particles. The process of reducing particle size in the magnetoliquefied layer in the beater mill is observed only with the intense movement of the dispersed system's particles. Due to the significant reduction in dispersion time in the magnetoliquefied layer, energy consumption is reduced [19].

When processing dispersed substances in any milling apparatus, the resulting powder not only has a specific granulometric composition but also various structural defects that increase the particles' reactivity. In producing fine powders of strontium hexaferrite in powder metallurgy, high demands are placed on both the dispersed composition and the structural characteristics of the dispersed system [20]. Therefore, studying the milling process is necessary to determine effective operating conditions for the apparatus in terms of changing the powder's dispersed composition and structural characteristics.

The aim of this work was to study the effect of mechanical processing of a coarse-grained strontium hexaferrite system in a beater mill in a magnetoliquefied layer on the granulometric composition, structural characteristics of the powder, and its magnetic properties before and after annealing.

The tasks were carried out using research methods such as scanning electron microscopy, *X*-ray diffraction, and magnetic measurements of powder samples.

Experimental

To conduct the research, coarse strontium hexaferrite material with an average particle size of 1558.5 μm, a most probable size of 1420 μm, a dispersion of 497 μm, and a median of 1476.9 μm was milled in a beater mill, where the milling bodies rotated at a frequency of 15.0 ± 1.6 thousand rpm in a horizontal plane. During the milling of magnetic materials in a beater mill, two processes occur: particle fragmentation due to their interaction with the milling bodies and particle aggregation. As the particle size of the milled dispersed material decreases, their tendency to aggregate increases, and the milling intensity significantly decreases. When the dispersed system is processed in a beater mill in a magnetoliquefied layer, the intensity of movement of the ferromagnetic elements and the frequency of their collisions with the rotating milling bodies increase. In the magnetoliquefied layer of ferromagnetic dispersed systems, under certain electromagnetic conditions, the destruction of aggregates occurs [21; 22]. To form a magnetoliquefied layer from the dispersed system in the mill, which ensures the deflocculation of ferromagnetic elements and the return of the powder to the area of the rotating milling bodies, the material was subjected to magnetic fields: an alternating field with a frequency of 50 Hz and an induction gradient of 90 mT/m, as well as a constant field with an induction of 15.3 mT.

The study of the patterns of change in the dispersed composition and structural characteristics during the milling of the initial dispersed strontium hexaferrite system was carried out by analyzing samples taken after 10, 30 and 120 min of milling.

The granulometric composition of the powder samples was analyzed using a Supra 25 scanning electron microscope (Carl Zeiss, Germany). The structural characteristics of the milled dispersed material were investigated using *X*-ray diffraction analysis on a XRD-7000 diffractometer (Shimadzu, Japan) with CuK_α radiation (wavelength $\lambda = 1.5406$ Å) and Bragg-Brentano focusing (θ–2θ). Given the complex appearance of the $SrFe_{12}O_{19}$ phase diffraction pattern, the PowderCell software version 2.3, based on the Rietveld full-profile refinement method, was used to process the diffraction spectra of the powder samples [23; 24]. The ICSD database was used for analyzing and refining the structural characteristics. *X*-ray measurements were conducted at room temperature in step-scan mode (step size 0.03°) over the angular range of $2\theta = 5 \div 90°$. The exposure time at each step was 8 s. The profile R-factor was selected as the criterion for good agreement between the structural model and the actual experiment.

The magnetic properties of the strontium hexaferrite powder samples were investigated using a LakeShore vibrating sample magnetometer (USA) at room temperature and normal atmospheric pressure. The magnetic field measurements were conducted with a precision of 0.1 Oe. The hysteresis loops were recorded in the "Continuous" mode to ensure consistent and detailed measurement of the magnetic behavior.

Results and discussion

The average particle size after 10, 30 and 120 min of processing the dispersed system in the beater mill was 12.48 μm, 1.09 μm and 0.57 μm, respectively.

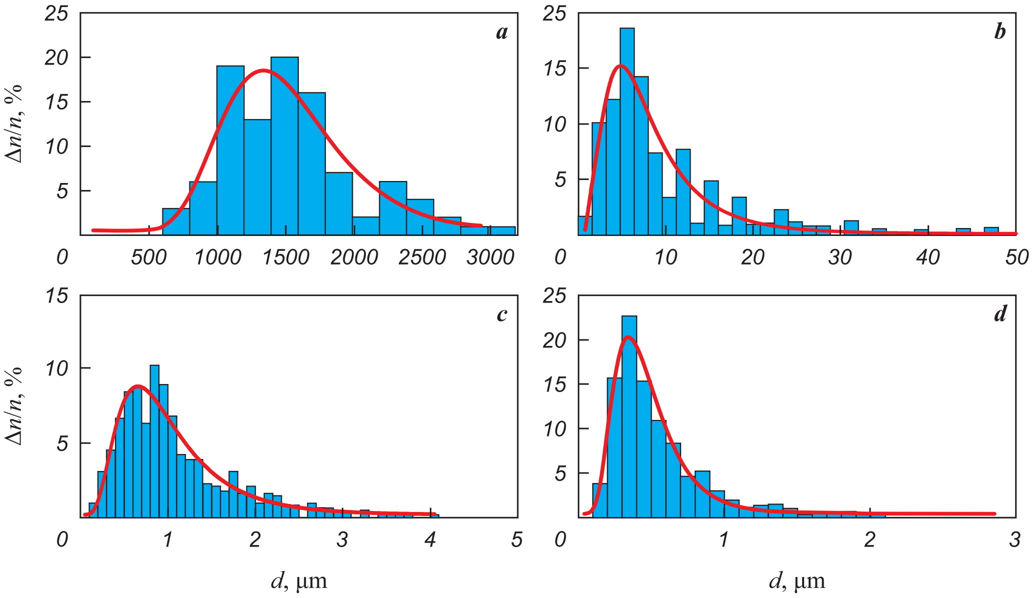

Fig. 1. Histograms and logarithmic-normal distribution functions of strontium hexaferrite powder particle sizes
a – initial powder, ***b–d*** – after milling for 10 min (***b***), 30 min (***c***), 120 min (***d***)

Рис. 1. Гистограммы и функции логарифмически нормального распределения порошка гексаферрита стронция по размерам
a – исходное состояние; ***b–d*** – после измельчения в течение 10 мин (***b***), 30 мин (***c***), 120 мин (***d***)

The experimental results indicate that after 10 min of milling, the degree of milling (the ratio of the average particle size of the initial dispersed system to the average particle size of the milled product) was 124.9. In the subsequent 20 min, the degree of milling decreased to 11.5 and after 90 min, it significantly reduced to 1.9. The rate of particle size reduction during the first 10 min of milling was 154.6 µm/min, during the following 20 min, it was 0.57 µm/min, and during the further 90 min, it was only 0.006 µm/min.

Thus, the most intense milling of the strontium hexaferrite dispersed material occurs in the first 10 min of milling. This result is consistent with studies showing that the strength of the particles and the work required for their fragmentation increase as the particle size decreases [25–27].

From the histograms and functions of the logarithmic-normal distribution of strontium hexaferrite powder particle sizes shown in Fig. 1, it is evident that for the initial dispersed material (Fig. 1, *a*), the most probable size is 1337.23 µm, and the width of the function maximum at half-height is 968.16 µm. After 10, 30 and 120 min of milling in the beater mill in a magnetoliquefied layer, the most probable particle sizes were 4.93 µm, 0.67 µm and 0.34 µm, respectively, and the width of the maximum at half-height of the particle size distribution function decreased to 7.68 µm, 0.91 µm and 0.40 µm, respectively (Fig. 1, *b*–*d*). The morphological features of the strontium hexaferrite powder particles after 120 min of milling in the magnetoliquefied layer are shown in Fig. 2. Thus, after 30 min of milling, the homogeneity of the dispersed composition increases significantly.

The experimental results show that the process of milling the initial strontium hexaferrite dispersed system in a beater mill in a magnetoliquefied layer can be divided into three stages. During the first stage, lasting 10 min, the most intense milling occurs. In the second stage, which lasts 20 min, milling is less intense, but the homogeneity of the dispersed system distribution increases. In the third stage, lasting 90 min, the milling

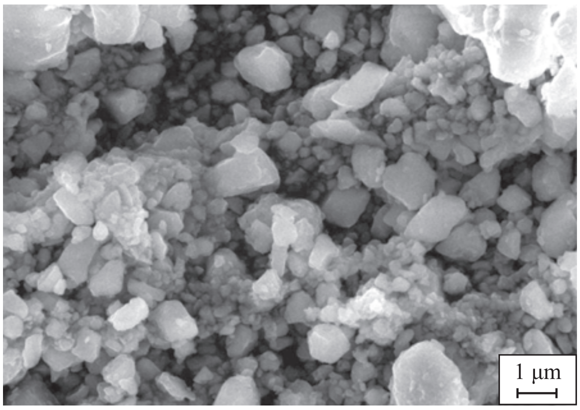

Fig. 2. Morphological features
of strontium hexaferrite powder particles after 120 min
of milling in a magnetoliquefied layer

Рис. 2. Морфологические особенности частиц порошка
гексаферрита стронция после 120 мин измельчения
в магнитоожиженном слое

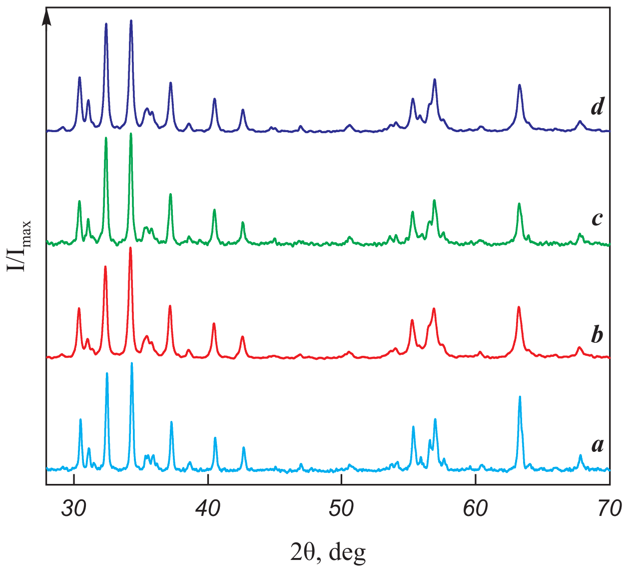

Fig. 3. *X*-ray diffraction patterns of the relative intensity of strontium hexaferrite dispersed material samples

a – initial powder, ***b***–***d*** – after milling for 10 min (***b***), 30 min (***c***), 120 min (***d***)

Рис. 3. Рентгенограммы относительной интенсивности образцов дисперсного материала гексаферрита стронция

a – исходное состояние; ***b***–***d*** – после измельчения в течение 10 мин (***b***), 30 мин (***c***), 120 мин (***d***)

intensity decreases significantly, but the homogeneity of the dispersed system increases substantially.

However, milling leads to the accumulation of crystal structure defects, which reduces the magnetic properties of the powder. It is evident that the most complete information about changes in the structural characteristics of the milled material can be obtained by studying the diffraction profiles of the *X*-ray patterns of powder samples of the initial dispersed material and after milling for $\tau = 10$, 30 and 120 min (Fig. 3). The duration of processing the dispersed material in the mill in a magnetoliquefied layer affects the sizes of coherent scattering regions (CSR), the magnitude of additional relative microstrains $\Delta d/d_{hkl}$ (Δd being the average change in interplanar spacing d_{hkl} due to the presence of defects), and the dislocation density ρ.

According to *X*-ray diffraction analysis data (Fig. 3), milling the coarse strontium hexaferrite material in a beater mill for $\tau = 120$ min in a magnetoliquefied layer does not lead to a change in the phase composition.

Fig. 4 presents histograms showing changes in the sizes of the coherent scattering regions (*D*), lattice microstrains ($\Delta d/d$), and dislocation density (ρ) for samples of the initial strontium hexaferrite dispersed material and after processing in the mill for $\tau = 10$, 30 and 120 min. For the initial dispersed material, the CSR size was $D = 309.4$ Å, the dislocation density was $\rho = 3.13 \cdot 10^{11}$ cm^{-2}, and the relative deformation was $\Delta d/d = 3.49 \cdot 10^{-4}$. As the milling time increases, the size of the crystallites, determined from the analysis of the broadening of diffraction lines, decreases, while the lattice microstrain of the $SrFe_{12}O_{19}$ phase and the dislocation density increase. However, during the processing of the dispersed system in the magnetoliquefied layer, the intensity of changes in the structural characteristics of the powder varies. In the first stage of milling ($\tau = 10$ min), there is an intense reduction in particle size, but the contribution of defect formation processes is small. As seen in Fig. 4, during this stage of processing the initial strontium hexaferrite dispersed system, the change in lattice microstrain $\Delta d/d$ increased by $1.06 \cdot 10^{-4}$, the dislocation density ρ increased by $0.21 \cdot 10^{11}$ cm^{-2}, and the CSR size *D* decreased by 9.9 Å. In the second stage of processing the dispersed system for 20 min in the mill, the milling intensity decreases, and the defect formation process intensifies. During this stage, the change in lattice microstrain increased by $\Delta d/d = 7.50 \cdot 10^{-4}$, the dislocation density increased by $\rho = 1.15 \cdot 10^{11}$ cm^{-2}, and

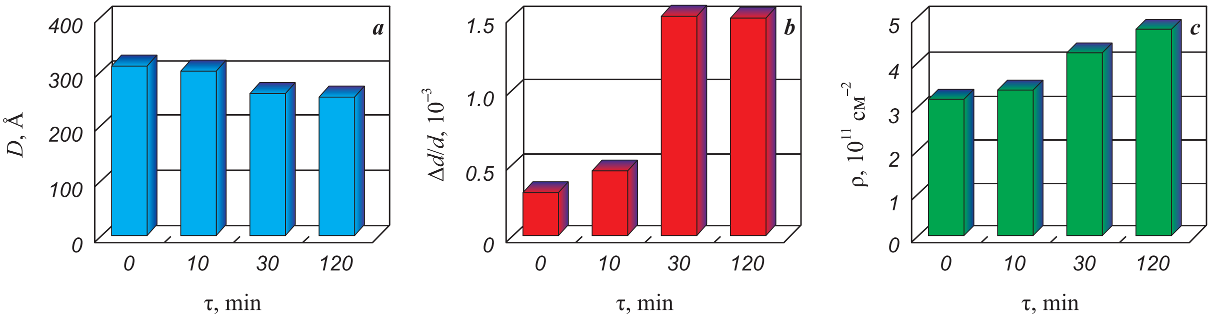

Fig. 4. Changes in the size of coherent scattering regions *D* (***a***), lattice microstrains $\Delta d/d$ (***b***) and dislocation density ρ (***c***) for samples of the initial dispersed strontium hexaferrite material and after milling with different durations (τ)

Рис. 4. Изменение размера областей когерентного рассеяния *D* (***a***), микроискажений кристаллической решетки $\Delta d/d$ (***b***), плотности дислокаций ρ (***c***) для образцов исходного дисперсного материала гексаферрита стронция и после обработки в мельнице с различной длительностью (τ)

the CSR size decreased by 41.0 Å. In the third stage of milling, lasting 90 min, the $\Delta d/d$ value increased by $1.27 \cdot 10^{-4}$, the ρ value increased by $0.21 \cdot 10^{11}$ cm^{-2}, and the CSR size D decreased by 5.96 Å.

The experimental results indicate that the most intense particle size reduction process during the treatment of the dispersed system in a magnetoliquefied layer occurs within the first 10 min, with the degree of milling reaching 271.2 at this stage. The most significant increase in lattice microstrain and dislocation density is observed between 10 and 30 min, during which the average size of the dispersed system changed from 12.48 μm to 1.09 μm. Between 30 and 120 min of milling, the intensity of the milling and defect formation processes decreases, but the homogeneity of the dispersed system increases significantly.

After 120 min of milling the initial strontium hexaferrite dispersed system, the average particle size was 0.57 μm, with a median of 0.46 μm, and the values of D, $\Delta d/d$ and ρ were 252.54 Å, $13.32 \cdot 10^{-4}$ and $4.70 \cdot 10^{11}$ cm^{-2}, respectively.

The magnetic properties of bulk samples made from strontium hexaferrite powder, processed in a beater mill in a magnetoliquefied layer for 120 min, before and after annealing can be evaluated from the magnetic hysteresis loops shown in Fig. 5. To restore the crystalline structure of the sample, annealing was performed for 3 h at a temperature of 950 °C.

The results of the magnetic studies on the sample made from powder processed in a beater mill in a magnetoliquefied layer for 120 min showed that the saturation magnetization M_s was 60.032 G·cm^3/g, he remanent magnetization M_r was 29.991 G·cm^3/g, and the coercive force H_c was 1656.6 Oe. As a result of annealing, the magnetic properties of the strontium hexaferrite powder improved, with the saturation magnetization, remanent magnetization, and coercive force of the sample increasing by 8.7, 43.7 and 64.3 %, respectively.

Conclusion

The experimental studies conducted allow us to observe the changes in the granulometric composition, crystallite size of the phases, lattice microstrains, and dislocation density during the production of $SrFe_{12}O_{19}$ powder through milling in a magnetoliquefied layer. It was established that processing the dispersed system of coarse strontium hexaferrite material for 120 min in a beater mill within an alternating inhomogeneous magnetic field with a frequency of 50 Hz and an induction gradient of 90 mT/m, along with a constant field with an induction of 15.3 mT, does not alter the phase composition of the powder. However, it leads to a significant reduction in particle size, a decrease in the size of coherent scattering regions, and an increase in the lattice microstrain of the $SrFe_{12}O_{19}$ phase and the dislocation density.

It has been shown that during milling, the intensification of changes in the granulometric composition and structural characteristics of the dispersed system of the material being processed significantly decreases once the average particle size reaches 1 μm. Further milling results in a substantial reduction in the intensity of changes in the granulometric composition of the material processed in the mill, while the homogeneity of the dispersed system increases significantly.

According to studies conducted using a vibrating sample magnetometer, the magnetic characteristics of the sample made from the powder obtained after milling – namely, remanent magnetization, saturation magnetization, and coercive force – were determined. The magnetic properties of the sample increased as a result of annealing.

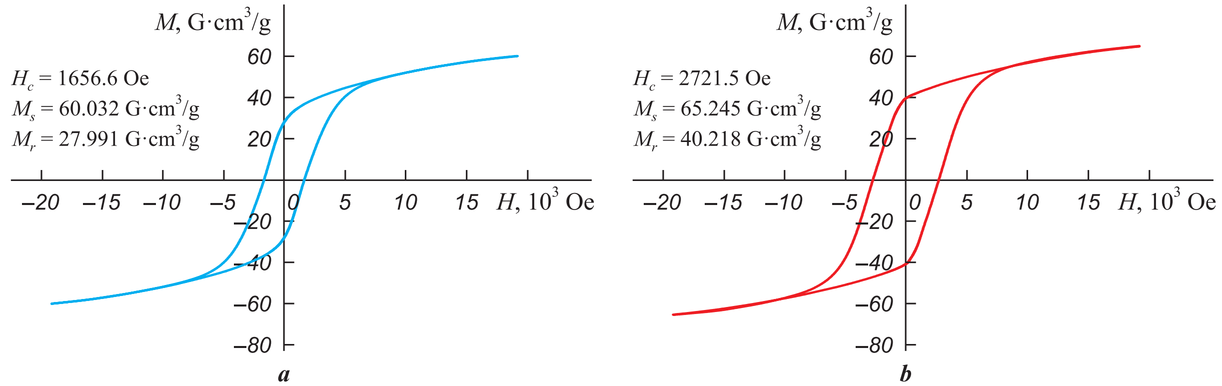

Fig. 5. Hysteresis loops of bulk samples of strontium hexaferrite powder after milling in a magnetoliquefied layer for 120 min (***a***) before annealing and (***b***) after annealing

Рис. 5. Магнитные петли гистерезиса объемных образцов порошка гексаферрита стронция после измельчения в магнитоожиженном слое в течение 120 мин до отжига (***a***) и после отжига (***b***)

References / Список литературы

1. Antsiferov V.N. Problems of powder materials. Part IV. Materials science polycrystalline ferrites. Ekaterinburg: UrO RAN, 2004. 395 p. (In Russ.).

   Анциферов В.Н. Проблемы порошкового материаловедения. Ч. IV. Материаловедение поликристаллических ферритов. Екатеринбург: УрО РАН, 2004. 395 с.
2. Pullar R. Hexagonal ferrites: A review of the synthesis, properties and applications of hexaferrite ceramics. *Progress in Materials Science*. 2012;57(7):1191–1334. https://doi.org/10.1016/j.pmatsci.2012.04.001
3. Kaneva I.I., Kostishin V.G., Andreev V.G., Chitanov D.N., Nikolaev A.N., Kislyakova E.I. Obtaining barium hexaferrite brand 7BI215 with isotropic properties. *Materials of Electronics Engineering*. 2014;(3):183–188. (In Russ.). https://doi.org/10.17073/1609-3577-2014-3-183-188

   Канева И.И., Костишин В.Г., Андреев В.Г., Читанов Д.Н., Николаев А.Н., Кислякова Е.И. Получение гексаферрита бария с повышенными изотропными свойствами. *Известия высших учебных заведений. Материалы электронной техники*. 2014;(3):183–188. https://doi.org/10.17073/1609-3577-2014-3-183-188
4. Ze Wu, Bashkirov L.A., Slonskaya S.V., Shauchenka S.V., Shambalyov V.N. Magnetic properties of permanent magnets based on M-type strontium ferrite with Sr^{2+} substituted by Sm^{3+} and Gd^{3+} and Fe^{3+} substituted by Zn^{2+} and Co^{2+}. *Proceedings of the National Academy of Sciences of Belarus. Chemical Series*. 2015;(3):11–16 (In Russ.).

   Цзэ У, Башкиров Л.А., Слонская С.В., Шевченко С.В., Шамбалев В.Н. Магнитные свойства постоянных магнитов на основе феррита стронция М-типа с замещением ионов Sr^{2+} ионами Sm^{3+}, Gd^{3+} и ионов Fe^{3+} ионами Zn^{2+}, Co^{2+} *Известия Национальной академии наук Беларуси. Серия химических наук*. 2015;(3):11–16.
5. Kikuchi T., Nakamura T., Yamasaki T., Nakanishi M., Fujii T., Takada J., Ikeda Y. Magnetic properties of La–Co substituted M-type strontium hexaferrites prepared by polymerizable complex method. *Journal of Magnetism and Magnetic Materials*. 2010;322(16):2381. https://doi.org/10.1016/j.jmmm.2010.02.041
6. Huang X., Zhang J., Wang L., Zhang Q. Simple and reproducible preparation of barium hexagonal ferrite by adsorbent combustion method. *Journal of Alloys and Compounds*. 2012;540(5):137–140. https://doi.org/10.1016/j.jallcom.2012.05.015
7. Ketov S.V., Yagodkin Yu.D., Lebed A.L., Chernopyatova Yu.V., Khlopkov K. Structure and magnetic properties of nanocrystalline $SrFe_{12}O_{19}$ alloy produced by high-energy ball milling and annealing. *Journal of Magnetism and Magnetic Materials*. 2006;300(1):e479–e481. https://doi.org/10.1016/j.jmmm.2005.10.199
8. Ketov S.V., Yagodkin Yu.D., Menushenkov V.P. Structure and magnetic properties of strontium ferrite anisotropic powder with nanocrystalline structure. *Journal of Alloys and Compounds*. 2011;509(3):1065–1068. https://doi.org/10.1016/j.jallcom.2010.09.184
9. Bollero A., Rial J., Villanueva M., Golasinski K.M., Seoane A., Almunia J., Altimira R. Recycling of strontium ferrite waste in a permanent magnet manufacturing plant. *ACS Sustainable Chemistry & Engineering*. 2017;5(4):3243–3249. https://doi.org/10.1021/acssuschemeng.6b03053
10. Liu B., Zhang S., Steenari B.M., Ekberg K. Synthesis and properties of $SrFe_{12}O_{19}$ obtained by solid waste recycling of oily cold rolling mill sludge. *International Journal of Minerals, Metallurgy, and Materials*. 2019;26:642–648. https://doi.org/10.1007/s12613-019-1772-2
11. Letyuk L.M. Technology of the ferrite materials and magnetoelectronics. Moscow: MISIS, 2005. 352 p. (In Russ.).

    Летюк Л.М. Технология ферритовых материалов магнитоэлектроники. М.: МИСИС, 2005. 352 с.
12. Goldman A. Modern ferrite technology. 2nd ed. Pittsburgh: Springer, 2006. 438 p.
13. Ketov S.V., Lopatina E.A., Bulatov T.A., Yagodkin Yu.D., Menushenkov V.P. Effect of milling in various media and annealing on the structure and magnetic properties of strontium hexaferrite powder. *Solid State Phenomena*. 2012;190:183–187. https://doi.org/10.4028/www.scientific.net/SSP.190.183
14. Stingaciu M., Topole M., McGuiness P., Christensen M. Magnetic properties of ball-milled $SrFe_{12}O_{19}$ particles consolidated by Spark-Plasma Sintering. *Scientific Reports*. 2015;5:14112. https://doi.org/10.1038/srep14112
15. Valverde J.M. Fluidization of fine powders: Cohesive versus Dynamical Aggregation. Netherlands: Springer, 2013. 136 p.
16. Espin M.J., Valverde J.M., Quintanilla M.A.S., Castellanos A. Stabilization of gas-fluidized beds of magnetic powders by a cross-flow magnetic field. *Journal of Fluid Mechanics*. 2011;680:80–113. https://doi.org/10.1017/jfm.2011.151
17. Vandewalle N., Lumay G. Flow properties and heap shape of magnetic powders. A*IP Conference Proceedings*. 2009; 1145:135–138. https://doi.org/10.1063/1.3179847
18. Egorov I.N., Egorova S.I., Vernigorov Yu.M. A method of milling magnetic materials and a device for its implementation: Patent 2306180 (RF). 2007. (In Russ.).

    Егоров И.Н., Егорова С.И., Вернигоров Ю.М. Способ измельчения магнитных материалов и устройство для его осуществления: Патент 2306180 (РФ). 2007.
19. Egorov I.N., Egorov N.Ya. Energy consumption of milling in beater mill in magnetoliquefied layer. *International Research Journal*. 2016;8(50):44–47. (In Russ.). https://doi.org/10.18454/IRJ.2016.50.182

    Егоров И.Н., Егоров Н.Я. Энергозатраты при измельчении в бильной мельнице в магнитоожиженном слое. *Международный научно-исследовательский журнал*. 2016;8(50):44–47. https://doi.org/10.18454/IRJ.2016.50.182
20. Andreev V.G., Kaneva I.I., Podgornaya S.V., Tikhonov A.N. Investigation of the effect duration of grinding powder of strontium hexaferrite microstructure and properties of the magnets on the basis of their. *Materials of Electronics Engineering*. 2010;(2):43–47. (In Russ.).

    Андреев В.Г., Канева И.И., Подгорная С.В., Тихонов А.Н. Исследование влияния длительности измельчения порошков гексаферрита стронция на микроструктуру и свойства магнитов на их основе. *Известия высших учебных заведений. Материалы электронной техники*. 2010;(2):43–47.

21. Egorov I.N. Investigation of electromagnetic effect on structuring processes in magnetoliquefied layer of ferrite disperse systems. *Advanced Engineering Research (Rostov-on-Don)*. 2012;3(64):44–50. (In Russ.).

Егоров И.Н. Исследование электромагнитного воздействия на процессы структурообразования в магнитоожиженном слое ферритовых дисперсных систем. *Вестник ДГТУ. Технические науки*. 2012;3(64):44–50.

22. Egorov I.N., Egorova S.I., Kryzhanovsky V.P. Particle size distribution and structural state analysis of mechanically milled strontium hexaferrite. *Materials Science Forum*. 2019;946:293–297.
https://doi.org/10.4028/www.scientific.net/MSF.946.293

23. PowderCell 2.3 – powder pattern calculation from single crystal data and refinement of experimental curves. URL: http://mill2.chem.ucl.ac.uk/ccp/web-mirrors/powdcell/a_v/v_1/powder/e_cell.html (accessed: 17.09.2023).

24. Rietveld H.M. A profile refinement method for nuclear and magnetic structures. *Journal of Applied Crystallography*. 1969;2:65–71.
https://doi.org/10.1107/S0021889869006558

25. Middlemiss S. Surface damage effects in single particle comminution. *International Journal of Mineral Processing*. 2007;84(1):207–220.
https://doi.org/10.1016/j.minpro.2007.03.001

26. Blanc N., Mayer-Laigle C., Frank X., Radjai F., Delenne J. Evolution of grinding energy and particle size during dry ball-milling of silica sand. *Powder Technology*. 2020;376:661–667.
https://doi.org/10.1016/j.powtec.2020.08.048

27. Sharapov R. Determination of the ball mills performance, taking into account the particle size of the finished product. *E3S Web of Conferences*. 2021;281:01004.
https://doi.org/10.1051/e3sconf/202128101004

Information about the Authors

Ivan N. Egorov – Cand. Sci. (Eng.), Assistant Professor, Lead Programmer at the Regional State Library named after Yu.A. Zhdanov, Southern Federal University (SFU)
ORCID: 0000-0001-8352-2311
E-mail: egorovivan1@gmail.com

Nikolay Ya. Egorov – Cand. Sci. (Eng.), Assistant Professor, Department of Technology And Professional Pedagogical Education, SFU
ORCID: 0000-0001-6921-1701
E-mail: nyegorov@sfedu.ru

Yury V. Rusalev – Postgraduate Student, Junior Scientist at the Smart Materials Research Institute, SFU
ORCID: 0000-0002-6507-6298
E-mail: rusalev@sfedu.ru

Svetlana I. Egorova – Dr. Sci. (Eng.), Assistant Professor, Department of Physics, Don State Technical University
ORCID: 0009-0003-6580-638X
E-mail: siyegorova@gmail.com

Сведения об авторах

Иван Николаевич Егоров – к.т.н., доцент, вед. программист Зональной научной библиотеки им. Ю.А. Жданова Южного федерального университета (ЮФУ)
ORCID: 0000-0001-8352-2311
E-mail: egorovivan1@gmail.com

Николай Яковлевич Егоров – к.т.н., доцент кафедры технологии и профессионально-педагогического образования ЮФУ
ORCID: 0000-0001-6921-1701
E-mail: nyegorov@sfedu.ru

Юрий Владимирович Русалев – аспирант, мл. науч. сотрудник Международного исследовательского института интеллектуальных материалов ЮФУ
ORCID: 0000-0002-6507-6298
E-mail: rusalev@sfedu.ru

Светлана Ивановна Егорова – д.т.н., доцент, профессор кафедры физики Донского государственного технического университета
ORCID: 0009-0003-6580-638X
E-mail: siyegorova@gmail.com

Contribution of the Authors

I. N. Egorov – defined the purpose of the work, conducted X-ray diffraction analysis, wrote the manuscript.
N. Ya. Egorov – conducted experiments on powder milling, participated in the discussion of the results.
Yu. V. Rusalev – investigated the magnetic properties of the powders.
S. I. Egorova – participated in the discussion of the results, wrote the manuscript.

Вклад авторов

И. Н. Егоров – определение цели работы, проведение рентгеноструктурного анализа, подготовка текста статьи.
Н. Я. Егоров – проведение экспериментов по измельчению порошков, участие в обсуждении результатов.
Ю. В. Русалев – исследование магнитных свойств порошков.
С. И. Егорова – участие в обсуждении результатов, написание текста статьи.

Received 26.11.2023
Revised 24.01.2024
Accepted 29.01.2024

Статья поступила 26.11.2023 г.
Доработана 24.01.2024 г.
Принята к публикации 29.01.2024 г.

Production Processes and Properties of Powders
Процессы получения и свойства порошков

UDC 621.762.2

https://doi.org/10.17073/1997-308X-2024-5-13-18

Research article
Научная статья

Synthesis of fine tungsten powders with low impurity content

A. B. Ankudinov, E. V. Evstratov ✉, M. I. Alymov

A.A. Baikov Institute of Metallurgy and Materials Science Russian Academy of Sciences
49 Leninskiy Prosp., Moscow 119334, Russia

✉ evev@imet.ac.ru

Abstract. A chemical-metallurgical method was used to synthesize fine tungsten powders with low oxygen content. The tungsten powders were obtained by hydrogen reduction of tungsten trioxide (WO_3) powders. Hydrogen was passed through a column with potassium hydroxide for drying. In the first series of experiments, three fractions of WO_3 powder of grade "P" 64–100 µm, 40–50 µm, and less than 25 µm were reduced at temperatures of 650, 800, and 950 °C. In the second series of experiments, tungsten powders were obtained by hydrogen reduction of three different WO_3 powders of grades "P", "CP", and "Tumelom". The resulting tungsten powders had varying oxygen contents (0.043–2.18 wt. %) and average particle sizes ranging from 35 to 345 nm. *X*-ray diffraction analysis confirmed the presence of pure tungsten. The minimum oxygen content (0.043 wt. %) in the tungsten powder was achieved by reducing tungsten oxide of grade "CP" at 950 °C for 3 h.

Keywords: synthesis, tungsten, powder, reduction, temperature

Acknowledgements: The work was carried out within the framework of state assignment 075-00320-24-00.

For citation: Ankudinov A.B., Evstratov E.V., Alymov M.I. Synthesis of fine tungsten powders with low impurity content. *Powder Metallurgy and Functional Coatings*. 2024;18(5):13–18. https://doi.org/10.17073/1997-308X-2024-5-13-18

Синтез дисперсных порошков вольфрама с низким содержанием примесей

А. Б. Анкудинов, Е. В. Евстратов ✉, М. И. Алымов

Институт металлургии и материаловедения им. А.А. Байкова РАН
Россия, 119334, г. Москва, Ленинский пр-т, 49

✉ evev@imet.ac.ru

Аннотация. Для синтеза дисперсных вольфрамовых порошков с низким содержанием кислорода использован химико-металлургический метод. Порошок вольфрама получали водородным восстановлением порошков вольфрамового ангидрида WO_3. Водород пропускали через колонну с гидроксидом калия для осушения. В первой серии экспериментов при температурах 650, 800 и 950 °С восстанавливали три фракции порошка вольфрамового ангидрида WO_3 марки Ч: 64–100, 40–50 и менее 25 мкм. Во второй серии экспериментов порошок вольфрама получали водородным восстановлением трех разных порошков вольфрамового ангидрида WO_3 марок Ч, ХЧ, «Тумелом». Получили порошки вольфрама с различным содержанием кислорода (0,043–2,18 мас. %) и средним размером частиц 35–345 нм. Рентгенофазовый анализ показал чистый вольфрам. Минимальное содержание кислорода (0,043 мас. %) в порошке вольфрама получено при восстановлении оксида вольфрама марки ХЧ при температуре 950 °С в течение 3 ч.

Ключевые слова: синтез, вольфрам, порошок, восстановление, температура

Благодарности: Работа выполнена в рамках государственного задания 075-00320-24-00.

Для цитирования: Анкудинов А.Б., Евстратов Е.В., Алымов М.И. Синтез дисперсных порошков вольфрама с низким содержанием примесей. *Известия вузов. Порошковая металлургия и функциональные покрытия*. 2024;18(5):13–18. https://doi.org/10.17073/1997-308X-2024-5-13-18

Introduction

Tungsten powders are widely used in various industries and scientific fields (e.g., radiation shielding for certain medical treatments, nuclear energy, mechanical engineering, etc.) [1–4].

Tungsten is characterized by a high melting point, high thermal conductivity, and low sputtering under plasma exposure, which makes it suitable for the fabrication of internal walls in thermonuclear reactors [5]. However, it is well known that oxygen impurities weaken grain boundaries, thus increasing the risk of cold cracking and leading to a higher ductile-to-brittle transition temperature [6; 7].

Fine tungsten powders are synthesized by various methods. The plasma chemical method is used to produce nanopowders of refractory metals such as W, Mo, Nb, and Ta with average particle sizes ranging from 10 to 100 nm or more [8; 9]. The particles of these powders have a regular shape [10; 11].

Experimental studies on the synthesis of fine tungsten powder from scheelite ($CaWO_4$) by the self-propagating high-temperature synthesis (SHS) method were presented in [12; 13]. After leaching the SHS products with a 20 % aqueous hydrochloric acid solution, tungsten powder with a purity of over 99.9 wt. % and particle size less than 0.5 μm was obtained.

In [14], experimental studies on the hydrogen reduction of tungsten acid vapors $WO_2(OH)_2$ at around 1000 °C were conducted, resulting in powders containing about 70 wt. % tungsten with a particle size of less than 5 nm.

The work [15] presented experimental studies on the hydrothermal synthesis of porous spherical tungsten oxide particles followed by hydrogen reduction at 600–650 °C. The spherical tungsten particles, measuring tens of microns, consisted of crystallites with sizes ranging from 28 to 37 nm.

In industrial practice, tungsten is typically produced using a chemical-metallurgical method [16; 17], which involves the hydrogen reduction of WO_3. This technology does not require expensive specialized equipment. Tungsten ores are enriched to obtain standard concentrates containing 55–65 wt. % tungsten trioxide (WO_3). Various technological schemes are used in industrial practice to process concentrates to produce tungsten trioxide, which serves as a precursor for the production of tungsten, tungsten carbide, and other products. The final compounds in the concentrate processing are usually tungsten acid (H_2WO_4) or ammonium paratungstate (APT) $5(NH_4)_2O\cdot 12WO_3\cdot 5H_2O$, which, upon calcination, yield WO_3. Tungsten acid completely loses water at $t = 500$ °C, while APT decomposes above 250 °C. The calcination temperature of APT depends on the intended use of WO_3.

The reduction process is conducted in tubular furnaces [18] with an excess of dry hydrogen passed over the powder bed (2–4 cm thick) at a rate ensuring the removal of water vapor at temperatures above 630 °C. The primary impurity in tungsten powders is oxygen, the content of which (depending on the reduction mode) ranges from 0.05 to 0.30 wt. % [19; 20].

Advancements in technology demand higher performance characteristics of tungsten powders, including finer particle size and lower oxygen content [21]. Therefore, the practical task of developing a technology for synthesizing fine tungsten powders with low oxygen content is highly relevant. This study aimed to investigate the influence of precursor particle size and reduction temperature on the particle size and oxygen content in tungsten powders.

Materials and methods

Tungsten powder was obtained by hydrogen reduction of three grades of tungsten trioxide (WO_3) powder: “P” (Pure), “CP” (Chemically Pure) and from LLC “Tumelom”. The hydrogen used conformed to the standard OST 11050.003-83. Hydrogen was passed through a column with potassium hydroxide for drying, ensuring a dew point of approximately –60 °C. The hydrogen flow rate was 1 L/min.

The oxygen content in all powders was analyzed using the infrared absorption method on a “Leco TC-600” (USA) apparatus. The method involves placing a powder sample in a graphite crucible within the analyzer’s furnace, where it melts to form a carbon-saturated melt in a helium atmosphere. The carbon in the molten bath reacts with the sample’s oxygen to form carbon monoxide, which is then flushed out of the furnace by the helium stream. The oxygen content is determined by molecular absorption spectroscopy in the infrared region.

X-ray diffraction analysis was conducted using a “DRON-3M” diffractometer (Burevestnik, Russia) in CuK_α radiation ($\lambda = 1.54158$ Å). Diffraction patterns were recorded in continuous scanning mode over the 2θ angle range of 20 to 80° with a step size of 0.02°. Phase identification was performed using the “Crystallographica Search Match” software based on the Powder Diffraction File (PDF-2) database.

Specific surface area determination by the BET method was performed according to GOST 2405 on a “TriStar 3000” surface area analyzer (Micromeritics, USA). Scanning electron microscopy (SEM) was carried out on an ultra-high resolution field emission scanning electron microscope "Zeiss Ultra plus" based on "Ultra 55" (Carl Zeiss LLC, Germany).

Results and discussions

First series of experiments. WO_3 powder of grade "P" was sieved into three fractions, µm: 64–100, 40–50, and less than 25. These three powders were reduced in a tubular furnace IMETRON for 2 h in a hydrogen stream at temperatures of 650, 800 and 950 °C. A nickel boat containing 5 g of each powder, with a layer thickness of about 3 mm, was placed in a vacuum-tight quartz retort with a diameter of 6 cm and a length of 80 cm. The temperature gradient along the boat was not more than 5 °C. The retort scheme, placed in the furnace, is shown in Fig. 1. Nine reduced tungsten powders were obtained. Table 1 presents the reduction modes for WO_3 powder grade "P" and the characteristics of the obtained tungsten powders.

Experimental data (Table 1) show that, regardless of the particle size of WO_3, increasing the reduction temperature decreases the oxygen content and increases the average particle size of the tungsten powder.

Second series of experiments. This series was performed on unsieved powders. The reduction of three grades of WO_3 powder was conducted for 3 h in a hydrogen stream at 950 °C. Three reduced tungsten powders were obtained (Table 2).

When reduced from WO_3 grade "CP" at 950 °C for 3 h, the tungsten powder with the lowest oxygen content – 0.043 wt. % – was obtained.

The average particle size (d) of the powders was calculated using the formula $d = 6/(\rho S)$, where ρ is the density of tungsten (19.3 g/cm^3), and S is the specific surface area of the powder, m^2/g.

The *X*-ray diffraction (XRD) results for all powders indicate pure tungsten (Fig. 2). Fig. 3 shows an SEM image of tungsten powder reduced from grade "CP" tungsten oxide at 950 °C for 3 h. The particle shapes of all the powders are similar, regardless of the reduction conditions, with the main difference being particle size.

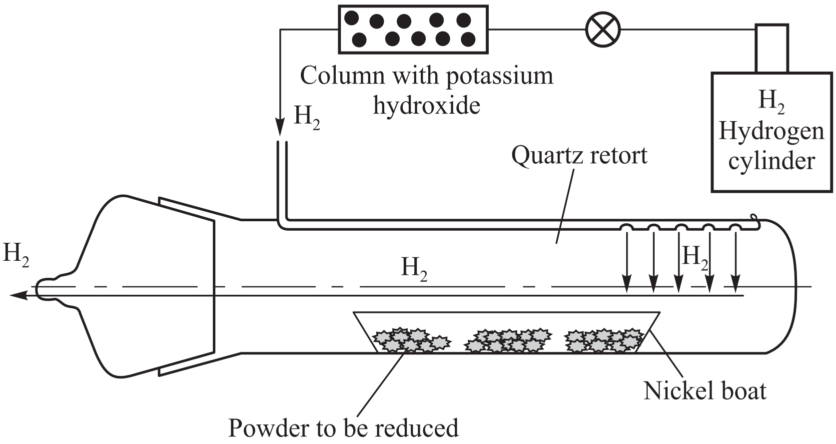

Fig. 1. Scheme of a retort for the reduction of powders

Рис. 1. Схема реторты для восстановления порошков

Table 1. **Reduction modes for WO_3 powder grade "P" and characteristics of tungsten powders**

Таблица 1. **Режимы восстановления порошка WO_3 марки Ч и характеристики порошков вольфрама**

Precursor particle size, µm	Reduction temperature, °C	Oxygen content, wt. %	Specific surface area, m^2/g	Average particle size, nm
<25	650	2.180	8.9	35
	800	0.390	4.5	69
	950	0.150	1.5	207
40–50	650	1.930	7.8	40
	800	0.270	3.6	86
	950	0.100	1.3	239
64–100	650	2.010	7.0	44
	800	0.230	3.3	94
	950	0.073	1.7	183

Table 2. **Characteristics of tungsten powders obtained at a reduction temperature of 950 °C, 3 h**

Таблица 2. **Характеристики порошков вольфрама, полученных при температуре восстановления 950 °C в течение 3 ч**

Tungsten oxide	Oxygen content, wt. %	Specific surface area, m^2/g	Average particle size, nm
P	0.091	1.5	207
CP	0.043	0.9	345
Tumelom	0.122	1.1	283

The results of all experiments are shown in Fig. 4. It can be seen that with an increase in the reduction temperature, there is a significant growth in the average particle size of the reduced tungsten powder, regardless of the precursor's dispersity. Simultaneously, the oxygen content decreases.

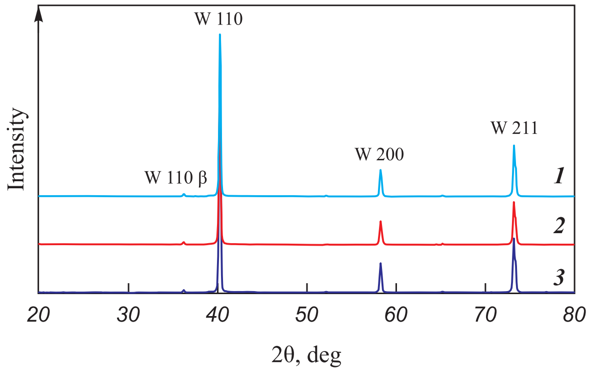

Fig. 2. *X*-ray patterns of tungsten powders
1 – Tumelom; ***2*** – P; ***3*** – CP

Рис. 2. Рентгенограммы порошков вольфрама
1 – Тумелом; ***2*** – Ч; ***3*** – ХЧ

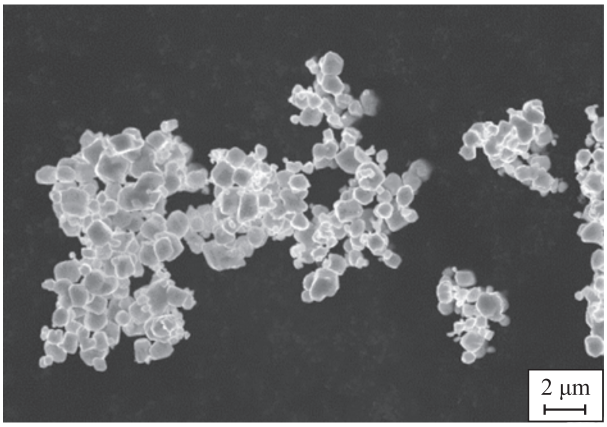

Fig. 3. SEM image of tungsten powder reduced from tungsten oxide of chemical grade "CP" at 950 °C for 3 h

Рис. 3. СЭМ-изображение порошка вольфрама, восстановленного из оксида вольфрама марки ХЧ при температуре 950 °C в течение 3 ч

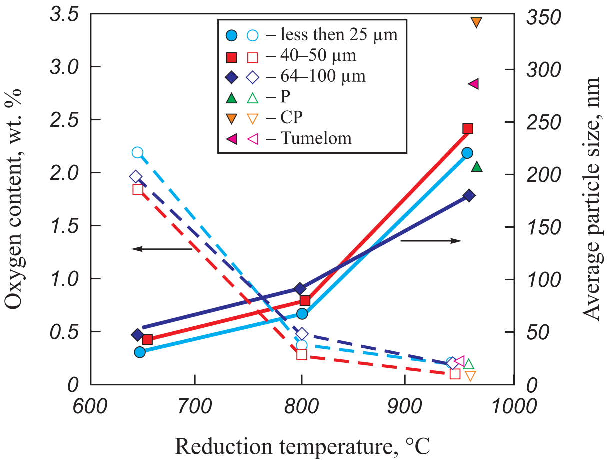

Fig. 4. Dependence of oxygen content and average particle size of tungsten powder on reduction temperature for different tungsten oxide powders

Рис. 4. Зависимость содержания кислорода и среднего размера частиц порошка вольфрама от температуры восстановления для разных порошков оксида вольфрама

Conclusion

Fine tungsten powders with low oxygen content were synthesized from tungsten trioxide using a chemical-metallurgical method. The minimum oxygen content in the powder was obtained by reducing tungsten oxide of grade "CP" at 950 °C for 3 h. The resulting tungsten powder had the lowest oxygen content of 0.043 wt.% and an average particle size of 345 nm.

References / Список литературы

1. Lassner E., Schubert W.-D. Tungsten: Properties, chemistry, technology of the element, alloys, and chemical compounds. N.Y.: Springer, 1999, 422 p.
https://doi.org/10.1007/978-1-4615-4907-9
2. Povarova K.B. Powder metallurgy of tungsten alloys (Alloying, pretreatment, sintering, TMT, structure, properties). In: *Proceedings of 3rd EURO PM 2004 – Powder metallurgy world congress and exhibition* (Viena, Austria. 17–21 October 2004). Vol. 5. P. 106–112.
3. Sahin Y. Recent progress in processing of tungsten heavy alloys. *Journal of Powder Technology*. 2014:764306.
https://doi.org/10.1155/2014/764306
4. Chernyak G.B., Povarova K.B. Tungsten in ammunition. Moscow: GNTs RF FGUP "TsNIIKhM", 2014. 355 p. (In Russ.).

   Черняк Г.Б., Поварова К.Б. Вольфрам в боеприпасах. М.: ГНЦ РФ ФГУП «ЦНИИХМ», 2014. 355 р.
5. Haag J.V., Wang J., Kruska K., Olszta M.J., Henager Jr.C.H., Edwards D.J., Setyawan W., Murayama M. Investigation of interfacial strength in nacre-mimicking tungsten heavy alloys for nuclear fusion applications. *Scientific Reports*. 2023;13(1):575.
https://doi.org/10.1038/s41598-022-26574-4

6. Braun J., Kaserer L., Stajkovic J., Leitz K.-H., Tabernig B., Singer P., Leibenguth P., Gspan C., Kestler H., Leichtfried G. Molybdenum and tungsten manufactured by selective laser melting: Analysis of defect structure and solidification mechanisms. *International Journal of Refractory Metals & Hard Materials*. 2019;84:104999.
https://doi.org/10.1016/j.ijrmhm.2019.104999

7. Veverka J., Vilémová M., Chlup Z., Hadraba H., Lukáč F., Csáki S., Matějíček J., Vontorová J., Chráska T. Evolution of carbon and oxygen concentration in tungsten prepared by field assisted sintering and its effect on ductility. *International Journal of Refractory Metals and Hard Materials*. 2021;97:105499.
https://doi.org/10.1016/j.ijrmhm.2021.105499

8. Krasovskii P.V., Samokhin A.V., Fadeev A.A., Sinayskiy M.A., Sigalaev S.K. Alloying effects and composition inhomogeneity of plasma-created multimetallic nanopowders: a case study of the W–Ni–Fe ternary system. *Journal of Alloys and Compounds*. 2018;750:265–275.
https://doi.org/10.1016/j.jallcom.2018.03.367

9. Samokhin A., Alekseev N., Sinayskiy M., Astashov A., Kirpichev D., Fadeev A., Tsvetkov Y., Kolesnikov A. Nanopowders production and micron-sized powders spheroidization in DC plasma reactors. *Powder Technology*. 2018;1:1–18.
http://doi.org/10.5772/intechopen.76262

10. Krasovskii P.V., Samokhin A.V., Malinovskaya O.S. Characterization of surface oxide films and oxygen distribution in α–W nanopowders produced in a DC plasma reactor from an oxide feedstock. *Powder Technology*. 2015;286:144–150.
http://doi.org/10.1016/j.powtec.2015.07.025

11. Samokhin A.V., Fadeev A.A., Alekseev N.V., Dorofeev A.A., Kalashnikov Ju.P., Sinaisky M.A., Zavertyaev I.D. Processing of tungsten nanopowder into micropowder consisting of spherical particles. *Inorganic Materials: Applied Research*. 2024;15(2):553–561.
https://doi.org/10.1134/S2075113324020369

Самохин А.В., Фадеев А.А., Алексеев Н.В., Дорофеев А.А., Калашников Ю.П., Синайский М.А., Завертяев И.Д. Сфероидизация нанопорошковых микрогранул вольфрама в термической плазме электродугового разряда. *Перспективные материалы*. 2023;(12):71–82.
https://doi.org/10.30791/1028-978X-2023-12-71-82

12. Jung J.C., Ko S.G., Won C.W., Cho S.S., Chun B.S. The self-propagation high-temperature synthesis of ultrafine high purity tungsten powder from scheelite. *Journal of Materials Research*. 1996;11(7):1825–1830.
https://doi.org/10.1557/JMR.1996.0230

13. Ẑivanovič P., Zdujič M., Nikolič Z., Tasič M., Kamberovič Ẑ. Unconventional methods for preparation of fine tungsten powder from scheelite. In: *Proceedings of 3rd BMC-2003-Ohnd* (R. Macedonia). 2004;10(4):343–353.

14. Ostermann M., Dalbauer V., Schubert W.-D., Haubner R. Preparation of nano-crystalline tungsten powders from gaseous $WO_2(OH)_2$. *Tungsten*. 2022;4:60–66.
https://doi.org/10.1007/s42864-021-00118-1

15. Guo J., Wen X., Wu Y., Xu J., Zhou J. Preparation of spherical tungsten particles assisted by hydrothermal method. *Journal of Wuhan University of Technology–Materials Science Edition*. 2023;38(6):1457–1462.
https://doi.org/10.1007/s11595-023-2842-x

16. Alymov M.I., Ankudinov A.B., Tregubova I.V., Zablotsky A.A. Synthesis of nanopowders on the base of tungsten. *Physics and Chemistry of Materials Treatment*. 2005;(6):81–82. (In Russ.).

Алымов М.И., Анкудинов А.Б., Трегубова И.В., Заблоцкий А.А. Синтез нанопорошков на основе вольфрама. *Физика и химия обработки материалов*. 2005;(6):81–82.

17. Alymov M.I. Powder metallurgy of nanocrystalline materials. Moscow: Nauka, 2007. 169 p. (In Russ.).

Алымов М.И. Порошковая металлургия нанокристаллических материалов. М.: Наука, 2007. 169 с.

18. Alymov M.I., Tregubova I.V., Povarova K.B., Ankudinov A.B., Evstratov E.V. Development of physicochemical foundations for the synthesis of tungsten-based nanopowders with controlled properties. *Russian Metallurgy*. 2006;(3):217–220.
https://doi.org/10.1134/S0036029506030062

Алымов М.И., Трегубова И.В., Поварова К.Б., Анкудинов А.Б., Евстратов Е.В. Разработка физико-химических основ синтеза нанопорошков на основе вольфрама с регулируемыми свойствами. *Металлы*. 2006;(3):37–40.

19. Zelikman A.N., Nikitina L.S. Tungsten. Moscow: Metallurgiya, 1978. 272 p. (In Russ.).

Зеликман А.Н., Никитина Л.С. Вольфрам. М.: Металлургия, 1978. 272 с.

20. Alymov M.I., Levinskiy Yu.V., Vershinina E.V., Naboichenko S.S., Kasimtsev A.V., Panov V.S. Metal powders. Products made from metal powders: Directory. Moscow: Infra-Inzheneriya, 2021. 560 p. (In Russ.).

Алымов М.И., Левинский Ю.В., Вершинина Е.В., Набойченко С.С., Касимцев А.В., Панов В.С. Металлические порошки. Изделия из металлических порошков: Справочник. Под ред. М.И. Алымова, Ю.В. Левинского. М.: Инфра-Инженерия, 2021. 560 с.

21. Wang R., Zhan X., Chen Y., Zhang C., Che Y., He J. Regulation of particle size and morphology of tungsten powders in bottom-blowing hydrogen reduction process. *International Journal of Refractory Metals and Hard Materials*. 2024;118:106495.
https://doi.org/10.1016/j.ijrmhm.2023.106495

Information about the Authors

Aleksey B. Ankudinov – Senior Research Scientist at the Laboratory of Physical Chemistry of Surfaces and Ultrafine Powder Materials, A.A. Baykov Institute of Metallurgy and Materials Science of the Russian Academy of Sciences (IMET RAS)
ORCID: 0009-0002-1150-8515
E-mail: a-58@bk.ru

Evgeniy V. Evstratov – Cand. Sci. (Eng.), Senior Research Scientist at the Laboratory of Physical Chemistry of Surfaces and Ultrafine Powder Materials of the IMET RAS
ORCID: 0009-0004-5507-7467
E-mail: evev@imet.ac.ru

Mikhail I. Alymov – Dr. Sci. (Eng.), Professor, Corresponding Member of the Russian Academy of Sciences, Head at the Laboratory of Physical Chemistry of Surfaces and Ultrafine Powder Materials of the IMET RAS
ORCID: 0000-0001-6147-5753
E-mail: malymov@imet.ac.ru

Сведения об авторах

Алексей Борисович Анкудинов – ст. науч. сотрудник лаборатории «Физикохимия поверхности и ультрадисперсных порошковых материалов» Института металлургии и материаловедения им. А.А. Байкова (ИМЕТ) РАН
ORCID: 0009-0002-1150-8515
E-mail: a-58@bk.ru

Евгений Викторович Евстратов – к.т.н., ст. науч. сотрудник лаборатории «Физикохимия поверхности и ультрадисперсных порошковых материалов» ИМЕТ РАН
ORCID: 0009-0004-5507-7467
E-mail: evev@imet.ac.ru

Михаил Иванович Алымов – д.т.н, профессор, член-корр. РАН, заведующий лабораторией «Физикохимия поверхности и ультрадисперсных порошковых материалов» ИМЕТ РАН
ORCID: 0000-0001-6147-5753
E-mail: malymov@imet.ac.ru

Contribution of the Authors

A. B. Ankudinov – prepared mixtures and initial samples, conducted experiments, and participated in the discussion of results.

E. V. Evstratov – prepared initial samples, participated in the discussion of results, and wrote the article.
M. I. Alymov – defined the objectives of the work, participated in the discussion of results, and co-authored the article.

Вклад авторов

А. Б. Анкудинов – приготовление смесей и исходных образцов, проведение экспериментов, участие в обсуждении результатов.
Е. В. Евстратов – исходные образцы, участие в обсуждении результатов, написание статьи.
М. И. Алымов – определение цели работы, участие в обсуждении результатов, написание статьи.

Received 29.03.2024
Revised 07.06.2024
Accepted 11.06.2024

Статья поступила 29.03.2024 г.
Доработана 07.06.2024 г.
Принята к публикации 11.06.2024 г.

Refractory, Ceramic, and Composite Materials
Тугоплавкие, керамические и композиционные материалы

UDC 620.193.2, 621.793

https://doi.org/10.17073/1997-308X-2024-5-19-29

Research article
Научная статья

High-entropy coatings in the FeCrNiCo–Mo_x system with enhanced corrosion and tribocorrosion resistance in seawater

K. A. Kuptsov, M. N. Fatykhova, A. N. Sheveyko, R. T. Islamov, A. A. Zaitsev, D. V. Shtansky

National University of Science and Technology "MISIS"
1 Bld, 4 Leninskiy Prosp., Moscow 119049, Russia

kuptsov.k@gmail.com

Abstract. To tackle the pressing challenge of protecting steel products in marine and coastal infrastructure from corrosion and tribocorrosion, high-entropy coatings in the FeCrNiCo–Mo_x system were developed using automated vacuum electrospark deposition with specialized equipment. Discs with a diameter of 30 mm made from 30Kh13 steel were used as substrates. The coatings were applied using FeCrNiCo–Mo_x electrodes, where $x = 0$, 5, 10, and 15 at. %, produced by powder metallurgy. The structure, elemental, and phase compositions of the coatings were evaluated using XRD, SEM, and EDS methods. FeCrNiCo–Mo_x coatings were obtained through the remelting of the substrate and electrode material. Coatings with a moderate molybdenum content (2–5 at. %) formed a single-phase solid solution with an FCC lattice. At a Mo content of around 7 at. %, the formation of a second phase based on molybdenum with a BCC lattice was observed. The thickness of the FeCrNiCo coatings was 45 µm, while the addition of molybdenum to the coatings reduced this thickness to 32–34 µm. The corrosion and tribocorrosion resistance of the coatings was assessed in artificial seawater using electrochemical and tribological methods. Under stationary corrosion conditions, the coating with 2 at. % Mo exhibited the highest corrosion resistance, with a corrosion potential of 50 mV and a corrosion current density of 2 µA/cm^2. Under tribocorrosion conditions, the coating with 5 at. % molybdenum demonstrated the highest wear resistance, with a value of $2 \cdot 10^{-5}$ mm^3/(N·m).

Keywords: electrospark deposition, vacuum, coatings, seawater, electrochemistry, wear resistance, corrosion resistance, tribocorrosion

Acknowledgments: The research was supported by the Russian Science Foundation, grant No. 20-79-10104-П.

For citation: Kuptsov K.A., Fatykhova M.N., Sheveyko A.N., Islamov R.T., Zaitsev A.A., Shtansky D.V. High-entropy coatings in the FeCrNiCo–Mo_x system with enhanced corrosion and tribocorrosion resistance in seawater. *Powder Metallurgy and Functional Coatings*. 2024;18(5):19–29. https://doi.org/10.17073/1997-308X-2024-5-19-29

Высокоэнтропийные покрытия в системе FeCrNiCo–Mo_x с повышенной коррозионной и трибокоррозионной стойкостью в морской воде

К. А. Купцов, М. Н. Фатыхова, А. Н. Шевейко, Р. Т. Исламов, А. А.Зайцев, Д. В. Штанский

Национальный исследовательский технологический университет «МИСИС»
Россия, 119049, г. Москва, Ленинский пр-т, 4, стр. 1

kuptsov.k@gmail.com

Аннотация. Для решения актуальной проблемы защиты стальных изделий морской и прибрежной инфраструктуры от коррозии и трибокоррозии были разработаны высокоэнтропийные покрытия в системе FeCrNiCo–Mo_x, получаемые методом автоматизированного электроискрового легирования в вакууме с использованием специальной установки. В качестве подложек применялись диски диаметром 30 мм из стали 30Х13. Для нанесения покрытий использовались электроды CrNiCo–xMo, где $x = 0$, 5, 10 и 15 ат. %, полученные методом порошковой металлургии. Структуру, элементный и фазовый составы покрытий оценивали методами РФА, СЭМ и ЭДС. За счет переплава материала подложки и электрода были получены покрытия FeCrNiCo–Mo_x. Покрытия с умеренной долей молибдена (2–5 ат. %) представляют собой однофазный твердый раствор с ГЦК-решеткой. При содержании Mo около 7 ат. % наблюдается формирование второй фазы на основе молибдена с ОЦК-решеткой. Толщина покрытий FeCrNiCo составляла 45 мкм, введение молибдена в состав покрытий приводило к ее снижению до 32–34 мкм. Оценка коррозионной и трибокоррозионной стойкости покрытий осуществлялась в искусственной морской воде электрохимическими и трибологическими методами. В стационарных коррозионных условиях покрытие с 2 ат. % Mo характеризовалось наибольшей коррозионной стойкостью: коррозионный потенциал составлял 50 мВ, плотность тока коррозии – 2 мкА/см^2. В трибокоррозионных условиях наибольшей износостойкостью на уровне $2\cdot10^{-5}$ мм^3/(Н·м) обладало покрытие с 5 ат. % молибдена.

Ключевые слова: электроискровое легирование, вакуум, покрытия, морская вода, электрохимия, износостойкость, коррозионная стойкость, трибокоррозия

Благодарности: Исследование выполнено за счет гранта Российского научного фонда № 20-79-10104-П.

Для цитирования: Купцов К.А., Фатыхова М.Н., Шевейко А.Н., Исламов Р.Т., Зайцев А.А., Штанский Д.В. Высокоэнтропийные покрытия в системе FeCrNiCo–Mo_x с повышенной коррозионной и трибокоррозионной стойкостью в морской воде. *Известия вузов. Порошковая металлургия и функциональные покрытия*. 2024;18(5):19–29. https://doi.org/10.17073/1997-308X-2024-5-19-29

Introduction

Currently, over 50 % of the world's population lives within 60 km of the coastline [1]. More than 80% of global trade is conducted by sea [2; 3]. Human economic activity in the marine and coastal zones is closely linked to the production and operation of marine transport vessels and coastal infrastructure. Steel, due to its high specific strength, wide availability, and favorable economic characteristics, is one of the primary structural materials used for these purposes [4; 5]. However, the challenges of using structural steels in seawater arise not only from corrosion but also from tribocorrosion – a phenomenon that combines mechanical wear and corrosion degradation [6; 7]. Tribocorrosion causes the most damage to friction pairs, such as bearings, shafts, rods, swivels, etc. [8], leading to a significant reduction in the service life of structures and resulting in substantial economic losses. In industrialized countries, the economic impact of tribocorrosion can account for up to 3–4 % of GDP [9; 10].

The primary method of corrosion control in marine environments is alloying steel with chromium and molybdenum due to their ability to form a dense passive film on the surface [11–13]. This film acts as a barrier, preventing contact between the metal and the aggressive environment, thereby protecting against further degradation. However, a recently discovered class of high-entropy alloys (HEAs) has outperformed traditional chromium- and molybdenum-enriched stainless steels in terms of tribocorrosion resistance [14–16]. Fe-based HEAs (Fe–Cr–Ni–Co–X) are promising materials for use in the marine industry due to their excellent mechanical and corrosion properties. Chromium promotes the formation of a stable and dense passive film, with high chromium content enhancing resistance to pitting corrosion. Nickel contributes to resistance against both general and localized corrosion and serves as an austenite stabilizer. Cobalt also plays a role in stabilizing the oxide film. However, the key element ensuring the formation of a dense and high-quality passive film, especially in the presence of chromium, is molybdenum.

The cost of high-entropy alloys is relatively high due to the substantial content of expensive alloying elements and the complex manufacturing process. Additionally, some HEAs have shown a tendency toward brittle behavior under certain conditions [17].

The most promising application of high-entropy alloys for corrosion protection is not in the fabrication of entire structural components from HEAs but in their use as surface coatings. Currently, HEA-based coatings are primarily produced by methods such as laser cladding, electro-spark deposition, magnetron sputtering, and others [18; 19].

Electro-spark deposition (ESD) in a vacuum using CNC-controlled equipment is one of the most promising methods for producing wear-resistant and corrosion-resistant coatings on various steels due to its improved uniformity and purity [20]. This method can produce relatively thick coatings, up to 200 µm [18; 21], with excellent adhesion strength due to micrometallurgical reactions between the electrode and the substrate. Additionally, this coating technology is characterized by its relative simplicity, cost-effectiveness, high productivity, ease of process automation, and the capability for localized coating deposition. During vacuum electro-spark deposition, material transfer from the electrode to the substrate and pulsed cathode-arc evaporation of the electrode, initiated by spark discharge, occur simultaneously. This enhances process efficiency and improves surface wettability, resulting in lower coating roughness [10].

The aim of this study was to investigate the influence of molybdenum on the structure, corrosion, and tribocorrosion properties of coatings based on the FeCrNiCo–Mo$_x$ high-entropy alloy.

Materials and methods

The FeCrNiCo–Mo$_x$ were deposited using a specialized vacuum system for electrospark deposition, equipped with a three-axis table and a rotating electrode holder [22]. the electrodes used for the coatings were produced by powder metallurgy from a base equiatomic mixture of CrNiCo with addition of 5, 10, and 15 at. % Mo. Iron was introduced into the coatings through the mixing of the substrate and electrode material during the electrospark deposition process.

Fig. 1 shows SEM images of high-purity (>99 %) metal powders of Cr (PKh-1S, <63 µm), Ni (PNK-0T2, <20 µm), Co (PK-1u, <1.2 µm), and Mo (PM99.95, <5 µm), which were used to prepare the initial mixture for electrode production. the powders were mixed in a ball mill for 4 h. Blanks were produced from the mixture by cold pressing, followed by sintering in a vacuum furnace at 1300 °C for 60 min (with a residual pressure in the vacuum chamber not exceeding $1\cdot10^{-2}$ Pa). After sintering, the electrode blanks were ground to produce rods 60 mm in length and 6 mm in diameter.

Before deposition, the vacuum chamber was evacuated to a pressure of $5\cdot10^{-3}$ Pa, after which Ar (99.993 %) was introduced to maintain a working pressure of 20 Pa. the coatings were deposited under the following parameters: electrode rotation speed – 1000 rpm, scanning speed and step – 500 mm/min and 0.5 mm, respectively. After each processing cycle, the scanning direction was changed to perpendicular to ensure better coverage and uniformity of the coatings.

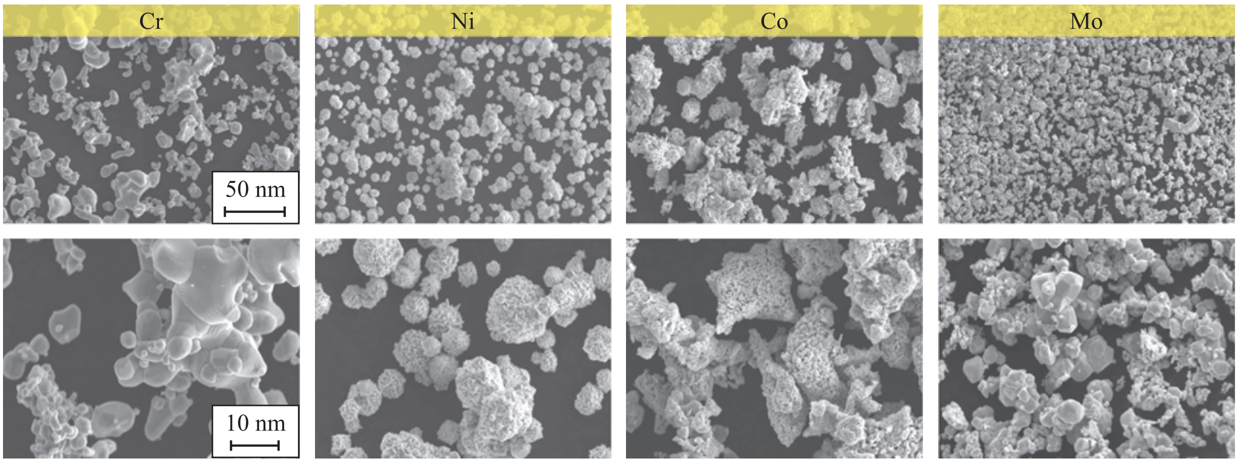

Fig. 1. SEM images of powders used for electrodes production

Рис. 1. СЭМ-изображения порошков, используемых для изготовления электродов

The FeCrNiCo–Mo_x coatings were deposited onto 30 mm diameter, 3 mm thick discs made of 30Kh13 steel under the following technological parameters: pulse frequency – 500 Hz, voltage – 50 V, pulse duration – 50 μs, electrode polarity – anodic.

Phase composition of the coatings was studied using X-ray phase analysis (XRD) on a D8 Advance diffractometer (Bruker, Germany) with monochromatic CuK_α radiation in the 2θ angle range from 10 to 100°.

Morphology and microstructure of the coatings were examined using a scanning electron microscope (SEM) S-3400N (Hitachi, Japan) equipped with an energy-dispersive spectrometer (EDS) NORAN (Thermo Scientific, USA).

Electrochemical properties of the coatings were studied in a three-electrode cell using an IPC Pro MF potentiostat (Russia). A platinum electrode was used as the auxiliary electrode, and an Ag/AgCl electrode served as the reference. the corrosion current density and potential were determined by extrapolating the polarization curves using the Tafel method.

Tribocorrosion resistance of the coatings was evaluated using a Tribometer (CSM Instruments, Switzerland) equipped with a special rotating cell that allows the registration of the electrochemical corrosion potential during tribological tests in a ball-on-disk configuration. the tests were conducted in artificial seawater at a load of 5 N, a distance of 500 m, and a sliding speed of 10 cm/s. the artificial seawater was prepared according to ASTM D1141-98 from the following salts (g/L): NaCl (24.53), $MgCl_2$ (5.20), Na_2SO_4 (4.09), $CaCl_2$ (1.16), KCl (0.695), $NaHCO_3$ (0.201), KBr (0.1), H_3BO_3 (0.027), $SrCl_2$ (0.003), NaF (0.003).

An alumina (Al_2O_3) ball with a diameter of 6 mm and a roughness of R_a = 0.8 μm was used as the counterbody. the wear tracks on the coatings were examined using optical profilometry with a WYKO NT1100 profilometer (Veeco, USA).

Results and discussion

Fig. 2 presents SEM cross-sectional images of the electrodes after sintering and the corresponding molybdenum distribution maps. All electrodes were characterized by high density and low residual porosity. Molybdenum in the CoCrNi–5Mo electrode was evenly distributed throughout the volume, while in electrodes with higher Mo content (10 and 15 at. %), clusters rich in molybdenum were observed.

The coatings obtained using the CoCrNi, CoCrNi–5Mo, CoCrNi–10Mo, and CoCrNi–15Mo electrodes are referred to as 0Mo, 5Mo, 10Mo, and 15Mo, respectively. Fig. 3 shows SEM images of the coating surfaces and the corresponding element distribution maps; the composition of the coatings is provided in Table 1.

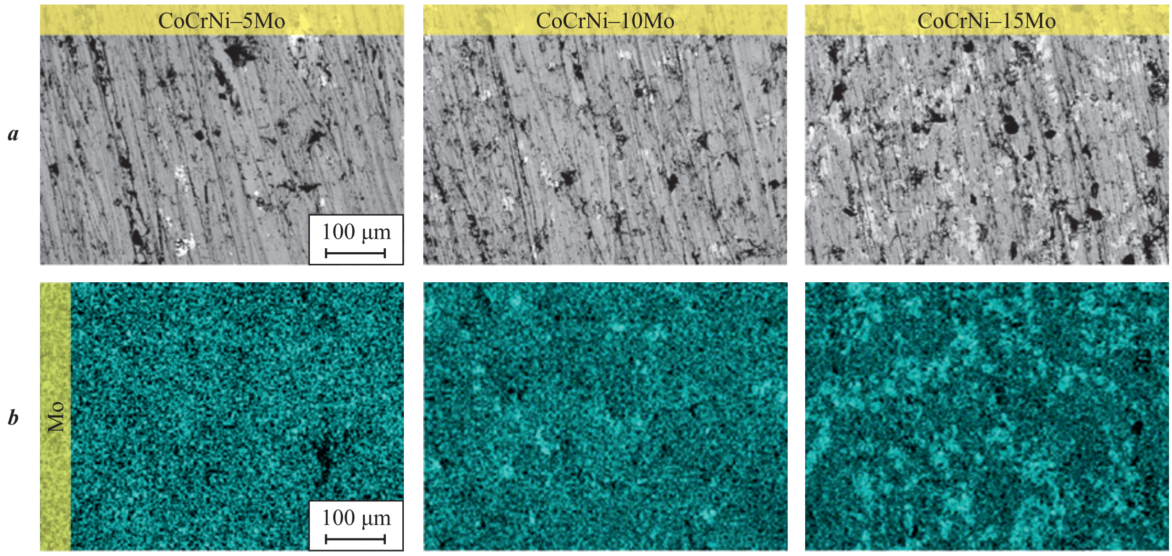

c

Electrodes	Contents, at. %			
	Cr	Co	Ni	Mo
CrNiCo–5Mo	32	31	33	5
CrNiCo–10Mo	29	30	31	10
CrNiCo–15Mo	28	29	28	15

Fig. 2. SEM images of electrode cross-sections (***a***), Mo distribution maps (***b***) and elemental composition (***c***)

Рис. 2. СЭМ-изображения шлифов электродов (***a***), карты распределения Mo (***b***) и элементный состав (***c***) the surface of the coatings exhibits a characteristic morphology in the form of overlapping areas of solidified melt formed by individual electrospark deposition pulses. No cracks or other surface defects were detected on the coatings. the 0Mo coating was characterized by a uniform distribution of elements across the surface. the introduction of Mo into the coatings resulted in the formation of a less homogeneous structure. It is evident that the 10Mo and 15Mo coatings consist of two distinct areas: 1) iron-based and 2) regions with higher concentrations of Mo, Ni, and Co. Additionally,

Table 1. **Elemental composition (at. %) of the surface of FeCrNiCo–Mo$_x$ coatings**

Таблица 1. **Элементный состав (ат. %) поверхности покрытий FeCrNiCo–Mo$_x$**

Coating	O	Cr	Fe	Co	Ni	Mo
0Mo	4	20	41	16	19	–
5Mo	4	21	41	17	15	2
10Mo	3	24	31	17	20	5
15Mo	5	20	43	12	13	7

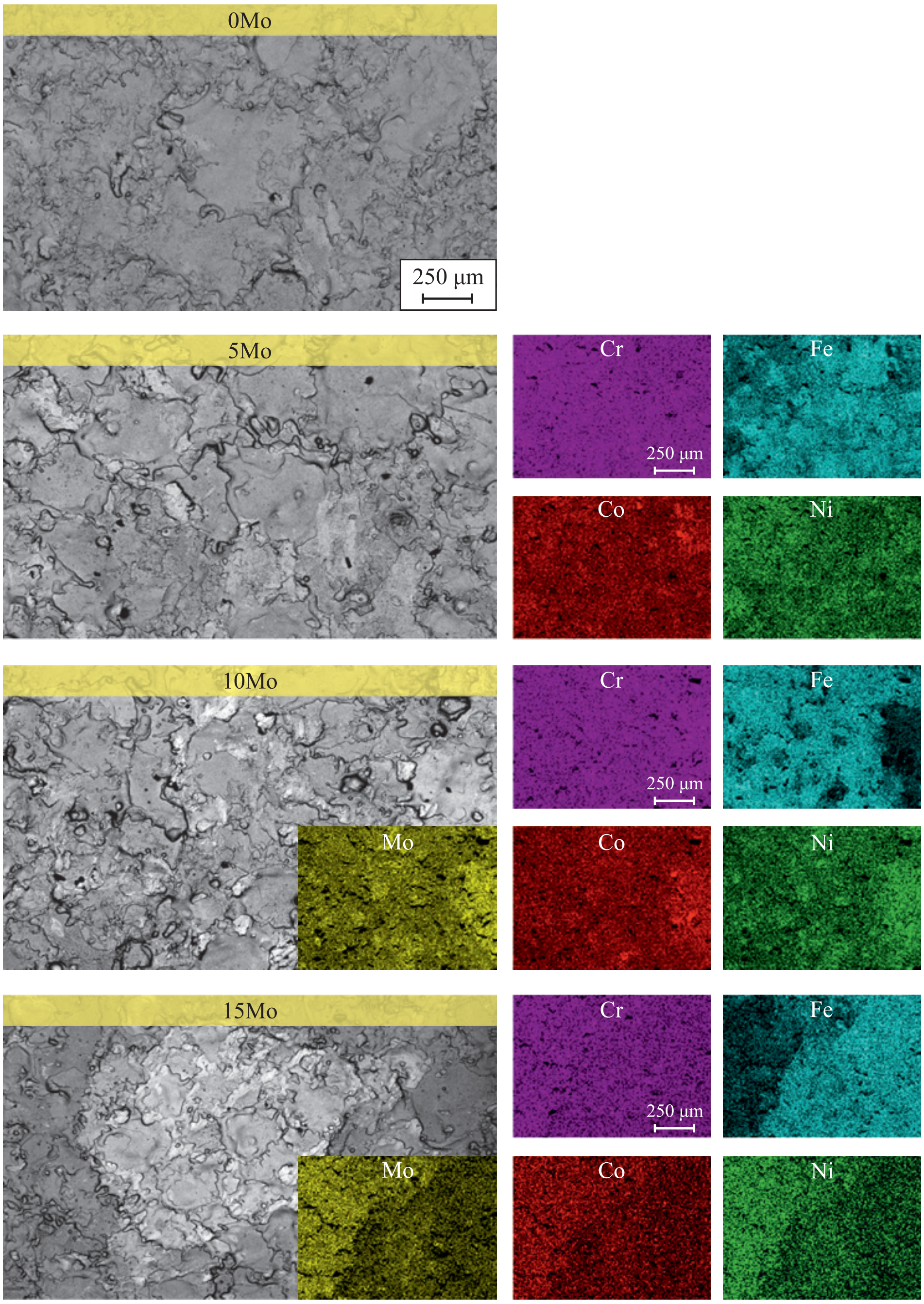

Fig. 3. SEM images of coating surface and corresponding element distribution maps

Рис. 3. СЭМ-изображения поверхности покрытий и соответствующие карты распределения элементов the coating with the highest molybdenum content exhibited increased surface roughness, with so-called "burns" containing large amounts of molybdenum.

Iron was the primary element in the coatings. the introduction of iron into the coatings occurred directly during electrospark deposition due to the mixing of the melts from both the electrode material and the substrate material in localized melting areas. the 10Mo coating had the lowest iron content, at 31 at. %, while in the other coatings it ranged between 41–43 at. %. This effect is likely due to more intensive transfer of the CoCrNi–10Mo electrode material. the molybdenum content in the coatings increased with its proportion in the electrodes, reaching 2 (5Mo), 5 (10Mo), and 7 (15Mo) at. %, respectively. the 10Mo coating had the highest chromium content of 24 at. %, while the other coatings showed chromium levels in the range of 20–21 at. %. the Ni and Co content in the 0Mo–10Mo coatings was 15–20 at. %, while in the coating with the highest molybdenum content, it was around 12–13 at. %. Additionally, all coatings showed a small oxygen content of about 3–5 at. %.

Fig. 4 shows SEM cross-sectional images of the coatings at various magnifications. the coatings exhibited high density, with no voids or cracks detected. the base FeCrNiCo coating without molybdenum had the highest thickness – up to 45 μm – while processing with molybdenum-containing electrodes reduced the thickness to 32–34 μm (5Mo–15Mo coatings). the reduction in coating thickness is associated with the altered material transfer during processing due to the introduction of refractory molybdenum, which led to a decrease in the size of the melt zone. Additionally, the molybdenum-containing coatings showed more pronounced transition areas between the substrate and the coating. the main layer of the 0Mo and 5Mo coatings was characterized by high uniformity, while the introduction of a higher amount of molybdenum into the coatings resulted in the formation of more distinct areas, rich in molybdenum and depleted in iron (Fig. 4, *c*). In the 10Mo coatings, these areas appeared as isolated clusters smaller than 5 μm, while in the 15Mo coating, these areas formed a discontinuous top layer.

Fig. 5 presents XRD patterns of FeCrNiCo–Mo$_x$ coatings and the steel substrate. All coatings were characterized by a single-phase structure based on a solid solution with an FCC lattice and a strong (200) texture, formed due to the directional solidification of the melt zones. Increasing the molybdenum content in the coatings leads to a shift of the FCC peaks towards lower angles, indicating an increase in the lattice parameter due to the large atomic radius of molybdenum. It is worth noting that the 10Mo and 15Mo coatings have the same lattice parameter, which may be due to the small difference in molybdenum content (5 and 7 at. %) and the fact that when the molybdenum con-

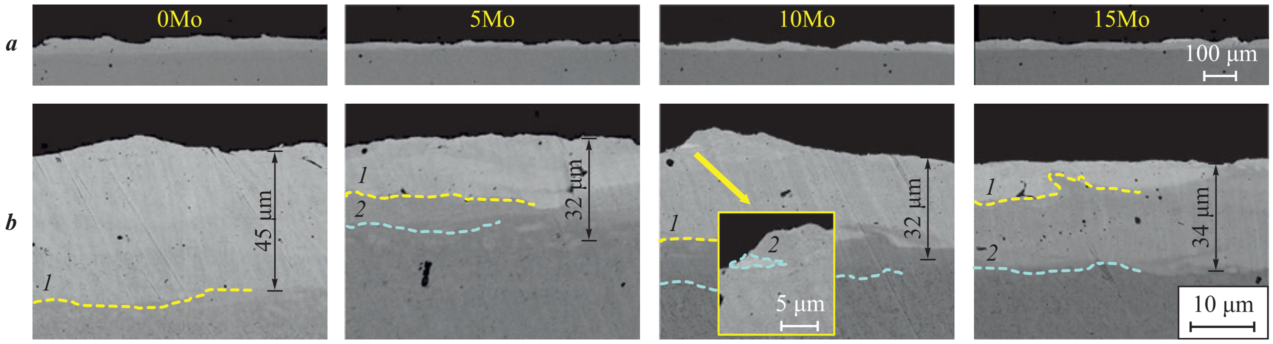

c

Coating	Area	Contents, at. %					
		O	Cr	Fe	Co	Ni	Mo
0Mo	*1*	5	22	27	23	23	–
5Mo	***1***	**12**	**18**	**50**	**7**	**10**	**3**
	2	–	**15**	**84**	–	**1**	–
10Mo	*1*	12	17	53	6	8	4
	2	13	25	10	21	23	8
15Mo	***1***	**11**	**22**	**21**	**17**	**19**	**10**
	2	**12**	**17**	**53**	**6**	**8**	**4**

Fig. 4. SEM images of cross-sections of FeCrNiCo–Mo$_x$ coatings at different magnifications (***a***, ***b***) and elemental composition of selected areas (***c***)

Рис. 4. СЭМ-изображения шлифов покрытий FeCrNiCo–Mo$_x$ при различных увеличениях (***a***, ***b***) и элементный состав выделенных областей (***c***)

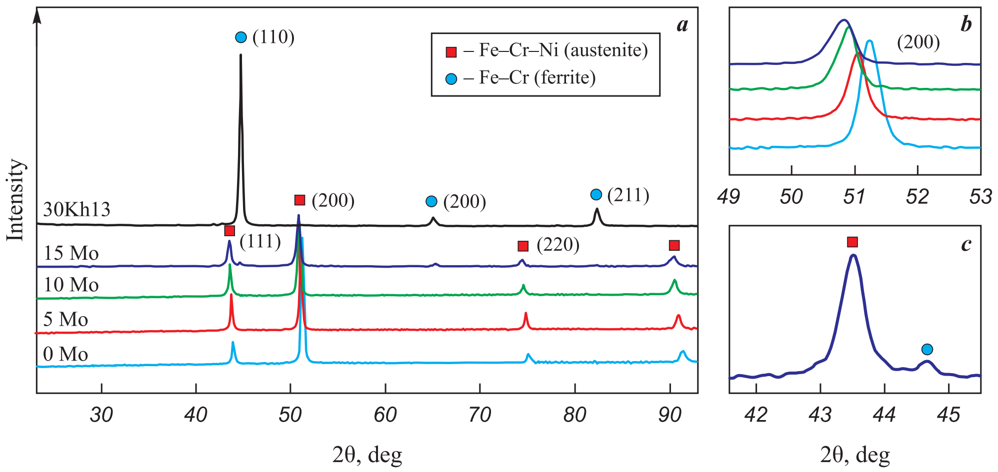

Fig. 5. XRD patterns of FeCrNiCo–Mo$_x$ coatings and 30Kh13 substrate (***a***),
as well as detailed image of FCC (200) peaks (***b***) and 15Mo coating (111) FCC and (110) BCC phases peaks (***c***)

Рис. 5. Дифрактограммы покрытий FeCrNiCo–Mo$_x$ и подложки 30Х13 (***а***),
а также увеличенное изображение пика (200) ГЦК-фазы (***b***) и пиков (111) ГЦК- и (110) ОЦК-фаз для покрытия 15Mo (***c***)

tent exceeds a certain threshold (5 at. % in our case), additional molybdenum can no longer be incorporated into the FCC lattice and will form its own phase.

In the case of the 15Mo coating, a second set of low-intensity peaks corresponding to an α-Fe (ferrite) phase can be distinguished. On one hand, these peaks could be attributed to the substrate, which has this structure. On the other hand, given the thickness of the coatings, this assumption seems unlikely. Another possible explanation is the formation of an additional BCC phase rich in molybdenum. the presence of such regions was shown in the cross-sections of the 15Mo coating. Additionally, molybdenum has very limited solubility in the FCC phase, as it is a ferrite stabilizer. Thus, processing with the CoCrNi–15Mo electrode is undesirable, as it leads to the formation of a two-phase coating.

Fig. 6 presents the results of tribocorrosion tests of FeCrNiCo–Mo$_x$ coatings. These tests included three stages: exposure to a corrosive environment (artificial seawater); tribological testing in a corrosive environment; and re-exposure under stationary conditions after the friction process was completed.

A key characteristic of tribocorrosion is the continuous wear of the passive film, which causes a sharp drop in corrosion potential due to the exposure of an active surface in the corrosive environment. the base 0Mo coating exhibited the highest corrosion potential during friction at –180 mV. Introducing a moderate amount of molybdenum (5Mo and 10Mo coatings) led to a more significant decrease in corrosion potential, down to –200 mV. the coating with the highest Mo content showed the highest drop in corrosion potential to –250 mV, likely due to the formation of galvanic couples between iron- and molybdenum-rich regions. the coefficient of friction for all coatings ranged from 0.2 to 0.3, with the lowest levels (0.2–0.25) observed in the 0Mo and 10Mo coatings.

The highest wear resistance was observed in the 10Mo and 15Mo coatings with higher molybdenum content – the wear rate was $(2.0\div2.7)\cdot10^{-5}$ mm^3/(N·m), whereas in the 0Mo and 5Mo coatings, it was $(4.1\div4.8)\cdot10^{-5}$ mm^3/(N·m). This effect is likely due to the strengthening of the high-entropy matrix in the 10Mo and 15Mo coatings through the formation of molybdenum-rich regions.

Wear tracks and the composition of wear products are shown in Fig. 7 and Table 2. the morphology of the wear tracks represents partially worn roughness, and the wear products are mainly represented by iron and chromium oxides.

The polarization curves of the coatings with varying Mo content are shown in Fig. 8. the corrosion potential and current density of the base FeCrNiCo coatings were 70 mV and 3.5 μA/cm^2, respectively. the introduction of 2 at. % Mo (5Mo coating) led to a slight shift of the potential in the negative direction to 50 mV, but at the same time, the corrosion current density decreased by almost a half (2 μA/cm^2). Further increasing the molybdenum content to 5–7 at. % (10Mo, 15Mo) caused an increase in the electrochemical potential to 110–120 mV; however, the corrosion current density increased to 4.0–4.5 μA/cm^2. Thus, the introduction of a small amount of molybdenum into FeCrNiCo leads to a reduction in corrosion current density, while further increases in molybdenum content primarily result in a significant shift in corrosion potential towards positive values.

This electrochemical behavior can be explained as follows. the introduction of a small amount of molyb-

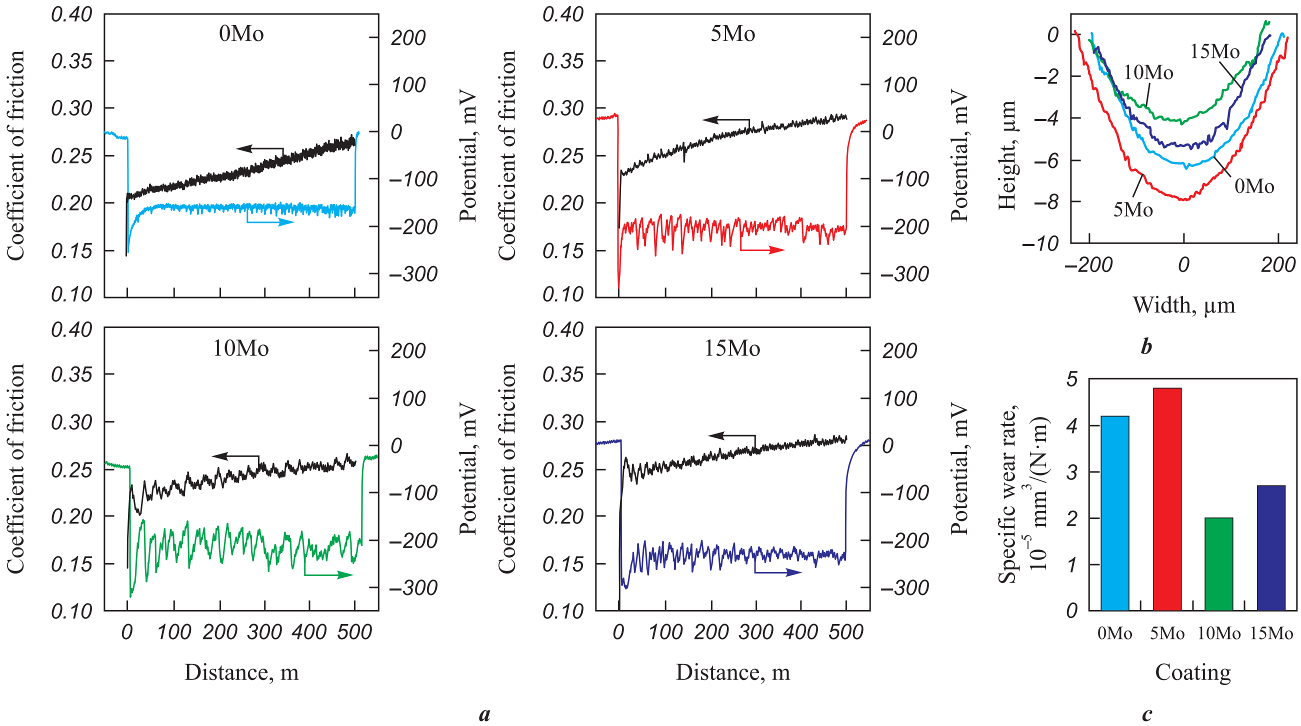

Fig. 6. Results of tribocorrosion tests (corrosion potential and coefficient of friction) of FeCrNiCo–Mo$_x$ coatings in artificial seawater (***a***), typical 2D wear track profiles (***b***) and wear rates (***c***)

Рис. 6. Результаты трибокоррозионных исследований (потенциал коррозии и коэффициент трения) покрытий FeCrNiCo–Mo$_x$ в искусственной морской воде (***a***), типичные 2D-профили дорожек износа (***b***) и значения приведенного износа (***c***)

denum (2 at. %) does not lead to the formation of molybdenum-rich regions, so the surface potential remains almost unchanged. Nevertheless, molybdenum in such quantities, especially when paired with chromium, contributes to the formation of a denser passive film, which improves the corrosion resistance of the 5Mo coatings. A higher molybdenum content in the coating leads to the formation of regions (possibly phases) rich in molybdenum, which shifts the surface potential in a more positive direction. However, the presence of surface heterogeneities intensifies corrosion processes.

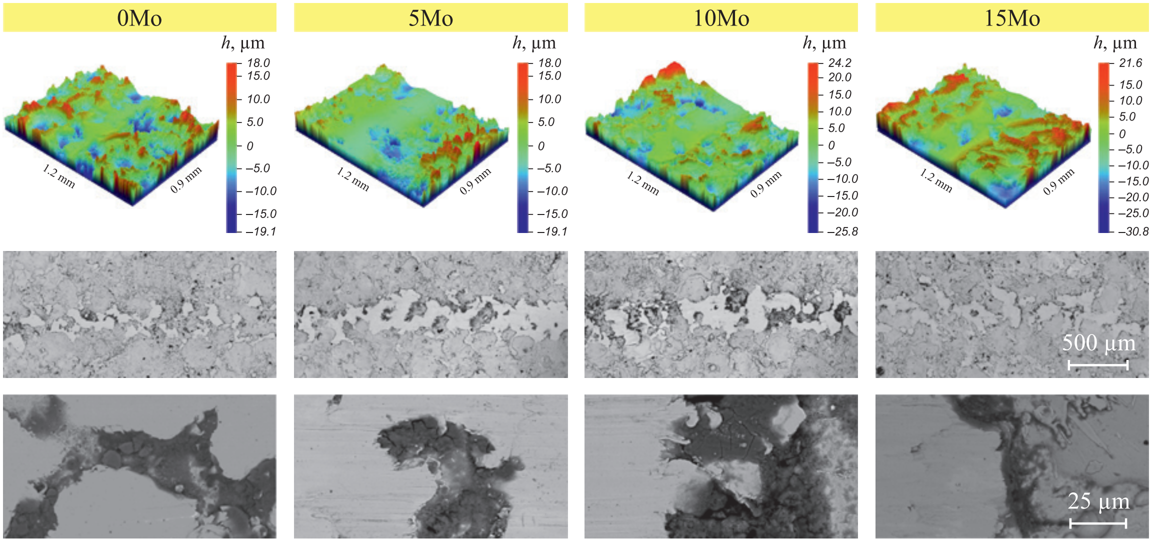

Fig. 7. 3D profiles and SEM images of wear tracks of FeCrNiCo–Mo$_x$ coatings after tribocorrosion tests

Рис. 7. 3D-профили и СЭМ-изображения дорожек износа покрытий FeCrNiCo–Mo$_x$ после трибокоррозионных испытаний

Table 2. **Elemental composition of wear products (at. %)**

Таблица 2. **Элементный состав продуктов износа (ат. %)**

Coating	C	O	Na	Mg	Si	Cl	Ca	Cr	Fe	Co	Ni	Mo
0Mo	38	37	1	1	1	1	1	4	10	3	3	–
5Mo	16	58	–	1	1	1	1	4	15	2	1	–
10Mo	18	54	1	1	1	1	1	4	15	2	2	–
15Mo	48	31	1	1	1	1	1	3	10	1	1	1

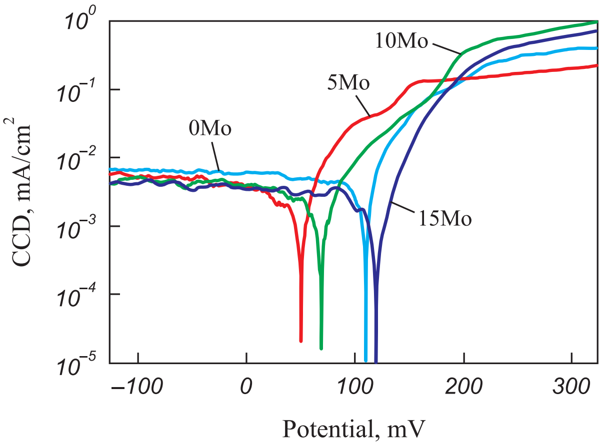

Fig. 8. Corrosion current density versus applied potential curves for coatings with varying molybdenum content

Рис. 8. Зависимости плотности тока коррозии от приложенного потенциала для покрытий с различным содержанием молибдена

Conclusions

1. High-entropy coatings with thicknesses up to 45 μm in the FeCrNiCo–Mo_x system with varying molybdenum content were successfully obtained using electrospark deposition in a vacuum. the introduction of a moderate amount of molybdenum in the range of 2–5 at. % into FeCrNiCo-based coatings has shown promise for enhancing their corrosion and tribocorrosion resistance in seawater.

2. All coatings with molybdenum content up to 5 at. % were single-phase solid solutions with an FCC lattice. the addition of higher amounts of molybdenum (7 at. %) led to the formation of a second phase based on molybdenum with a BCC lattice.

3. Under stationary corrosion conditions, the coating with 2 at. % Mo exhibited the highest corrosion resistance, with a corrosion current density and potential of 2 μA/cm^2 and 50 mV, respectively. the introduction of higher amounts of molybdenum (5–7 at. %) led to a shift in potential towards positive values, up to 120 mV, due to the formation of molybdenum-rich regions. However, the intensified local corrosion caused the corrosion current density to reach 4.5 μA/cm^2.

4. Under tribocorrosion conditions, coatings with moderate molybdenum content (up to 5 at. %) demonstrated a corrosion potential drop to –180 to –200 mV and a coefficient of friction around 0.25. the addition of higher amounts of molybdenum led to a more significant potential drop (down to –250 mV) and a higher coefficient of friction (up to 0.3). the coating with 5 at. % molybdenum exhibited the highest wear resistance, with a specific wear rate of $2 \cdot 10^{-5}$ mm^3/(N·m).

References / Список литературы

1. Andres M., Barragan J.M. Development of coastal cities and agglomerations: pressure and impacts on coastal and marine ecosystems. *WIT Transactions on the Built Environment*. 2015;148:63–71. https://doi.org/10.2495/CC150061
2. Usta O., Korkut E. Prediction of cavitation development and cavitation erosion on hydrofoils and propellers by detached eddy simulation. *Ocean Engineering*. 2019;191: 106512. https://doi.org/10.1016/j.oceaneng.2019.106512
3. Kruk C.B., Donner M. Freight transport for development toolkit. *Freight Transport for Development Toolkit*. 2009. https://doi.org/10.1596/27813
4. Abbas M., Rizvi S.H.M., Sarfraz S., Raza A., Khan A., Loya A., Najib A. Evaluation of the influence of dissolved nitrates on corrosion behaviour of ship structural steel exposed to seawater environment. *Ocean Engineering*. 2024;298:117268. https://doi.org/10.1016/J.OCEANENG.2024.117268
5. Tiamiyu A.A., Eduok U., Odeshi A.G., Szpunar J.A. Effect of prior plastic deformation and deformation rate on the corrosion resistance of AISI 321 austenitic stainless steel. *Materials Science and Engineering*. 2019;745:1–9. https://doi.org/10.1016/J.MSEA.2018.12.093
6. Liu Z.X., Li Y., Xie X.H., Qin J., Wang Y. the tribo-corrosion behavior of monolayer vn and multilayer VN/C hard coatings under simulated seawater. *Ceramics International*. 2021;47:25655–25663. https://doi.org/10.1016/J.CERAMINT.2021.05.291
7. Sofiani F.M., Tacq J., Elahi S.A., Chaudhuri S., De Waele W. A hybrid probabilistic-deterministic framework for prediction of characteristic size of corrosion pits in low-carbon steel following long-term seawater exposure. *Corrosion Science*. 2024;232:112039. https://doi.org/10.1016/J.CORSCI.2024.112039
8. Liu C., Jiang Z., Zhao J., Cheng X., Liu Z., Zhang D. Influence of rare earth metals on mechanisms of localised

corrosion induced by inclusions in Zr–Ti deoxidised low alloy steel. *Corrosion Science*. 2020;166:108463. https://doi.org/10.1016/j.corsci.2020.108463

9. Okoani A.O., Nand A., Ramezani M. Corrosion and wear interplay: Tribo-electrochemical evaluation of NiTiNOL60 alloy in sulfuric acid. *Results in Materials*. 2024;21: 100523. https://doi.org/10.1016/J.RINMA.2023.100523

10. Sun Y. Surface engineering & coating technologies for corrosion and tribocorrosion resistance. *Materials*. 2023; 16(13):4863. https://doi.org/10.3390/MA16134863

11. Santos R.F., Rocha A.M.F., Bastos A.C., Cardoso J.P., Rodrigues F., Fernandes C.M., Sacramento J., Ferreira M.G.S., Senos A.M.R., Fonseca C. Microstructural characterization and corrosion resistance of WC–Ni–Cr–Mo composite – the effect of Mo. *International Journal of Refractory Metals and Hard Materials*. 2020;86:105090. https://doi.org/10.1016/J.IJRMHM.2019.105090

12. Fu Y., Zhou F., Zhang M., Wang Q., Zhou Z. Structural, mechanical and tribocorrosion performances of CrMoSiN coatings with various Mo contents in artificial seawater. *Applied Surface Science*. 2020;525:146629. https://doi.org/10.1016/J.APSUSC.2020.146629

13. Ren X., Sun W., Tian S., Zhu C., Qin M., Yang Y., Wu W. Tribological and electrochemical behaviors of $FeCoNiCrMo_x$ HEA coatings prepared by internal laser cladding on 316L steel tube. *Materials Characterization*. 2024;211:113906. https://doi.org/10.1016/J.MATCHAR.2024.113906

14. Niu D., Zhang X., Sui X., Shi Z., Lu X., Wang C., Wang Y., Hao J. Tailoring the tribo-corrosion response of $(CrNbTiAlV)C_xN_y$ coatings by controlling carbon content. *Tribology International*. 2023;179:108179. https://doi.org/10.1016/J.TRIBOINT.2022.108179

15. Kafali M., Doleker K.M., Erdogan A., Sunbul S.E., Icin K., Yildiz A., Gok M.S. Wear, corrosion and oxidation characteristics of consolidated and laser remelted high entropy alloys manufactured via powder metallurgy. *Surface and Coatings Technology*. 2023;467:129704. https://doi.org/10.1016/J.SURFCOAT.2023.129704

16. Zeng C., Neils A., Lesko J., Post N. Machine learning accelerated discovery of corrosion-resistant high-entropy alloys. *Computational Materials Science*. 2024;237:112925. https://doi.org/10.1016/J.COMMATSCI.2024.112925

17. Li Q.H., Yue T.M., Guo Z.N., Lin X. Microstructure and corrosion properties of alcocrfeni high entropy alloy coatings deposited on AISI 1045 steel by the electrospark process. *Metallurgical and Materials Transactions A: Physical Metallurgy and Materials Science*. 2013;44:1767–1778. https://doi.org/10.1007/S11661-012-1535-4/FIGURES/15

18. Kuptsov K.A., Antonyuk M.N., Sheveyko A.N., Bondarev A.V., Ignatov S.G., Slukin P.V., Dwived P., Fraile A., Polcar T., Shtansky D.V. High-entropy Fe–Cr–Ni–Co–(Cu) coatings produced by vacuum electro-spark deposition for marine and coastal applications. *Surface and Coatings Technology*. 2023;453:129136. https://doi.org/10.1016/J.SURFCOAT.2022.129136

19. Zhang C., Lu X., Zhou H., Wang Y., Sui X., Shi Z.Q., Hao J. Construction of a compact nanocrystal structure for $(CrNbTiAlV)N_x$ high-entropy nitride films to improve the tribo-corrosion performance. *Surface and Coatings Technology*. 2022;429:127921. https://doi.org/10.1016/J.SURFCOAT.2021.127921

20. Kuptsov K.A., Antonyuk M.N., Bondarev A.V., Sheveyko A.N., Shtansky D.V. Electrospark deposition of wear and corrosion resistant Ta(Zr)C–(Fe,Mo,Ni) coatings to protect stainless steel from tribocorrosion in seawater. *Wear*. 2021;486–487:204094. https://doi.org/10.1016/J.WEAR.2021.204094

21. Sheveyko A.N., Kuptsov K.A., Antonyuk M.N., Bazlov A.I., Shtansky D.V. Electro-spark deposition of amorphous Fe-based coatings in vacuum and in argon controlled by surface wettability. *Materials Letters*. 2022;318: 132195. https://doi.org/10.1016/J.MATLET.2022.132195

22. Sytchenko A.D., Fatykhova M.N., Kuznetsov V.P., Kuptsov K.A., Petrzhik M.I., Kudryashov A.E., Kiryukhantsev-Korneev Ph.V. TaC-based wear-resistant coatings obtained by magnetron sputtering and electro-spark deposition for wedge gate valve protection. *Powder Metallurgy and Functional Coatings*. 2023;17(3):67–78. https://doi.org/10.17073/1997-308X-2023-3-67-78

Сытченко А.Д., Фатыхова М.Н., Кузнецов В.П., Купцов К.А., Петржик М.И., Кудряшов А.Е., Кирюханцев-Корнеев Ф.В. Покрытия на основе карбида тантала, полученные методами магнетронного распыления и электроискрового легирования, для повышения износостойкости деталей запорной арматуры. *Известия вузов. Порошковая металлургия и функциональные покрытия*. 2023;17(3):67–78. https://doi.org/10.17073/1997-308X-2023-3-67-78

Information about the Authors

Konstantin A. Kuptsov – Cand. Sci. (Eng.), Senior Researcher of the Scientific-Educational Center of SHS of MISIS–ISMAN
ORCID: 0000-0003-2585-0733
E-mail: kuptsov.k@gmail.com

Mariya N. Fatykhova – Cand. Sci. (Eng.), Junior Researcher of the Scientific-Educational Center of SHS of MISIS–ISMAN
ORCID: 0000-0001-6817-5999
E-mail: mariya.antonyuck@ya.ru

Aleksandr N. Sheveyko – Researcher of the Scientific-Educational Center of SHS of MISIS–ISMAN
ORCID: 0000-0003-3704-515X
E-mail: sheveyko@mail.ru

Сведения об авторах

Константин Александрович Купцов – к.т.н., ст. науч. сотрудник Научно-учебного центра (НУЦ) СВС МИСИС–ИСМАН
ORCID: 0000-0003-2585-0733
E-mail: kuptsov.k@gmail.com

Мария Николаевна Фатыхова – к.т.н., мл. науч. сотрудник НУЦ СВС МИСИС–ИСМАН
ORCID: 0000-0001-6817-5999
E-mail: mariya.antonyuck@ya.ru

Александр Николаевич Шевейко – науч. сотрудник НУЦ СВС МИСИС–ИСМАН
ORCID: 0000-0003-3704-515X
E-mail: sheveyko@mail.ru

Rafael T. Islamov – Research Assistant of the Department of Powder Metallurgy and Functional Coating of National University of Science and Technology "MISIS" (NUST MISIS)
✉ ***E-mail:*** livinoe@bk.ru

Aleksandr A. Zaitsev – Cand. Sci. (Eng.), Senior Researcher of the Laboratory "*In situ* diagnostics of structural transformations" of the Scientific-Educational Center of SHS of MISIS–ISMAN
ORCID: 0000-0001-6934-9137
✉ ***E-mail:*** aazaitsev@bk.ru

Dmitriy V. Shtansky – Dr. Sci. (Phys.-Math.), Head of the Research Center "Inorganic Nanomaterials" of NUST MISIS, Chief Researcher of the Scientific-Educational Center of SHS of MISIS–ISMAN
ORCID: 0000-0001-7304-2461
✉ ***E-mail:*** shtansky@shs.misis.ru

Рафаэль Тагирович Исламов – лаборант-исследователь кафедры порошковой металлургии и функциональных покрытий Национального исследовательского технологического университета «МИСИС» (НИТУ МИСИС)
✉ ***E-mail:*** livinoe@bk.ru

Александр Анатольевич Зайцев – к.т.н., ст. науч. сотрудник лаборатории «*In situ* диагностика структурных превращений» НУЦ СВС МИСИС–ИСМАН
ORCID: 0000-0001-6934-9137
✉ ***E-mail:*** aazaitsev@bk.ru

Дмитрий Владимирович Штанский – д.ф.-м.н., заведующий научно-исследовательским центром «Неорганические наноматериалы» НИТУ МИСИС, гл. науч. сотрудник НУЦ СВС МИСИС–ИСМАН
ORCID: 0000-0001-7304-2461
✉ ***E-mail:*** shtansky@shs.misis.ru

Contribution of the Authors

K. A. Kuptsov – defined the research objectives and conceptual framework, applied the coatings, described the results, prepared the manuscript, and formulated the conclusions.
M. N. Fatykhova – defined the research objectives and conceptual framework, conducted microstructural studies, electrochemical and tribocorrosion tests, and prepared the graphical materials.

A. N. Sheveyko – described the electrochemical results.
R. T. Islamov – prepared the literature review.
A. A. Zaitsev – performed the XRD analysis.

D. V. Shtansky – defined the research objectives and conceptual framework.

Вклад авторов

К. А. Купцов – определение цели работы и концепции исследований, нанесение покрытий, описание результатов, подготовка текста статьи, формулировка выводов.
М. Н. Фатыхова – определение цели работы и концепции исследований, проведение микроструктурных исследований, электрохимических и трибокоррозионных испытаний, подготовка графического материала.
А. Н. Шевейко – описание электрохимических результатов.
Р. Т. Исламов – подготовка литературного обзора.
А. А. Зайцев – проведение рентгенофазового структурного анализа.
Д. В. Штанский – определение цели работы и концепции исследований.

Received 16.04.2024
Revised 06.05.2024
Accepted 13.05.2024

Статья поступила 16.04.2024 г.
Доработана 06.05.2024 г.
Принята к публикации 13.05.2024 г.

UDC 677.523

https://doi.org/10.17073/1997-308X-2024-5-30-36

Research article
Научная статья

The effect of an oiling agent on the technological properties of coreless silicon carbide fiber

D. V. Tsytsarkina✉**, P. A. Timofeev**

JSC "Kompozit"
4 Pionerskaya Str., Korolev, Moscow region 141070, Russia

✉ tsytsarkinadv@inbox.ru

Abstract. A study was conducted to investigate the influence of oiling agents with various formulations on the properties of coreless silicon carbide fiber from the perspective of its technological qualities. The oiling agents investigated included formulations of PMS-5, PMS-10, PMS-20 in isopropyl alcohol and acetone, aqueous emulsions of PMS-200 with the addition of dispersant IVP-317 and polyvinyl alcohol, an aqueous solution of PEG-400 (30 %), and an aqueous solution of starch (10 %). The evaluation of the oiling agent's impact on the technological properties of the fiber was carried out through tensile strength testing, determination of the minimum bending radius, examination of the surface morphology of the oiled fibers, and the ability of the tested composition to bundle filaments together and reduce fuzzing. It was found that oiling agents using acetone and isopropyl alcohol as solvents led to the deterioration of the technological qualities of the treated fibers, significantly increasing their brittleness. The aqueous solution of polyethylene glycol (PEG-400) (30 %) poorly distributed on the fiber surface and reduced the strength characteristics of the samples after treatment. The strength of the samples treated with an aqueous starch solution (10 %) was found to be close to that of untreated fibers in tensile testing. This composition improved the homogeneity of the bundle and exhibited the best bonding properties on the filaments within it, but the increased brittleness of the fibers after drying significantly reduced their technological efficiency. The use of PMS-200 aqueous emulsion with IVP-317 contributed to increased homogeneity and flexibility of the bundle but led to a deterioration in the strength characteristics of the samples compared to pure fiber. The best result was shown by the PMS-200 emulsion with the addition of polyvinyl alcohol and dispersant IVP-317. This composition increased flexibility, reduced fuzzing, and improved the technological properties of the treated fibers, with only a slight reduction in the strength of the samples. The results obtained suggest that the aqueous emulsion based on polymethylsiloxane (PMS-200) and polyvinyl alcohol is the most effective oiling agent for coreless silicon carbide fiber.

Keywords: coreless silicon carbide fiber, SiC fiber, textile oiling agents, emulsification, fiber technological properties

For citation: Tsytsarkina D.V., Timofeev P.A. The effect of an oiling agent on the technological properties of coreless silicon carbide fiber. *Powder Metallurgy and Functional Coatings*. 2024;18(5):30–36. https://doi.org/10.17073/1997-308X-2024-5-30-36

Влияние замасливающего агента на технологические свойства бескернового карбидокремниевого волокна

Д. В. Цыцаркина, **П. А. Тимофеев**

АО «Композит»
Россия, 141070, Московская обл., г. Королев, ул. Пионерская, 4

tsytsarkinadv@inbox.ru

Аннотация. Проведено исследование влияния замасливателей различных рецептур на свойства бескернового карбидокремниевого волокна с точки зрения его технологических качеств. Исследованы замасливающие агенты составов ПМС-5, ПМС-10, ПМС-20 в изопропиловом спирте и ацетоне, водные эмульсии ПМС-200 с добавлением диспергатора IVP-317 и поливинилового спирта, водный раствор ПЭГ-400 (30 %), водный раствор крахмала (10 %). Оценка влияния замасливателя на технологические качества волокна осуществлялась путем проведения испытания образцов на прочность при растяжении, определения минимального радиуса гиба, исследования морфологии поверхности замасленных волокон, способности исследуемого состава объединять филаменты в составе пучка и снижать пушение. Установлено, что замасливающие агенты, в качестве растворителя в которых используются ацетон и изопропиловый спирт, приводят к ухудшению технологических качеств обработанных волокон, значительному повышению их ломкости. Водный раствор полиэтиленгликоля (ПЭГ-400) (30 %) плохо распределялся по поверхности волокна и снизил прочностные характеристики образцов после обработки. Прочность образцов, обработанных водным раствором крахмала (10 %), по результатам испытания на растяжение оказалась близкой к прочности необработанных волокон. Данный состав повысил однородность пучка и показал наилучшие скрепляющие свойства на филаменты в его составе, однако повышенная ломкость волокон при изгибе после высыхания в значительной степени снизила их технологичность. Применение водной эмульсии ПМС-200 с IVP-317 способствовало повышению однородности и гибкости пучка, однако привело к ухудшению прочностных характеристик образцов по сравнению с чистым волокном. Наилучший результат показала эмульсия ПМС-200 с добавлением поливинилового спирта и диспергатора IVP-317. Данный состав повысил гибкость, уменьшил пушение, улучшил технологические качества обработанных волокон, незначительно при этом снизив прочность образцов. Полученные результаты позволяют считать водную эмульсию на основе полиметилсилоксана (ПМС-200) и поливинилового спирта наиболее эффективной в качестве замасливающего агента для бескернового карбидокремниевого волокна.

Ключевые слова: бескерновое карбидокремниевое волокно, SiC-волокно, текстильные замасливатели, эмульсирование, технологические свойства волокна

Для цитирования: Цыцаркина Д.В., Тимофеев П.А. Влияние замасливающего агента на технологические свойства бескернового карбидокремниевого волокна. *Известия вузов. Порошковая металлургия и функциональные покрытия*. 2024;18(5): 30–36. https://doi.org/10.17073/1997-308X-2024-5-30-36

Introduction

The implementation of advanced composite materials is the foundation for the prospective development of aviation and rocket-space technology. Composites based on modern materials are widely used in the production of elements and assemblies for the aerospace industry [1–3].

The designs of modern aircraft require minimal weight, high reliability, rigidity, strength of components, and maximum operational lifespan of structures capable of functioning effectively under high temperatures and in aggressive oxidative environments.

The use of advanced composites with improved manufacturing technology and the introduction of new materials in their production plays a key role in solving these challenges [4; 5]. Composite materials reinforced with continuous coreless silicon carbide fibers with metallic and ceramic matrices are applicable to various components of aircraft that operate at high temperatures: thrust vectoring nozzles of propulsion systems, exhaust gas valves, nozzle guide vanes, etc. [6–14].

Silicon carbide fibers are characterized by high strength properties, reaching up to 3 GPa, a modulus of elasticity of 400 GPa, low oxygen content (less than 1 %), and high oxidative stability at elevated temperatures up to 1500 °C [15; 16].

The data presented allows us to consider SiC fibers as a promising reinforcing component for composites that operate in aggressive oxidative environments at high temperatures [17; 18].

Some applications of final products made from composite materials require reinforcing fillers in the form of fabric. However, creating textile preforms is challenging due to the inherent brittleness of SiC fibers. to enhance the processability of silicon carbide fibers for textile manufacturing, oiling compositions are applied. the emulsification process, which involves applying an oiling agent to the fiber surface, improves the technological properties of the fibers and the threads derived from them. This process helps prevent breakages and abrasion during thread formation, reduces friction when high-modulus ceramic fibers interact with manufacturing equipment, binds individual monofilaments together, lowers the dynamic friction coefficient, and prevents static electricity buildup [19–22].

The most commonly used textile oiling agents for chemical fibers include oils (both mineral and natural), surfactants, starch-based compositions, and organic polymers [23–25].

The aim of this study is to investigate the impact of different oiling agent formulations on the technological properties of coreless silicon carbide fibers.

Materials and methods

The study was carried out on specially prepared samples in the form of bundles of continuous coreless silicon carbide fibers. the diameter of the fibers ranged from 14 to 20 µm, and the bundle contained 150 fibers.

The oiling compositions used in this work were based on organosilicon compounds (polymethylsiloxanes (PMS)), polyethylene glycol (PEG-400), polyvinyl alcohol (PVA), and starch. Acetone, isopropyl alcohol, and water were used as solvents.

The application of the oiling agent to the surface of the silicon carbide fiber was carried out by immersing the fiber bundle in the solution, followed by gentle squeezing according to the following scheme (Fig. 1): the fiber from the guiding roller *1* was dipped into the oiling bath *2*, advanced by roller *3*, and then passed through squeeze rollers *4* to remove excess agent.

The tensile strength of the oiled fibers was evaluated using an "Instron 5942" testing machine (Instron, USA) according to GOST 32667 for samples with a working length of 25 mm and an average diameter of 17 µm. the tensile speed of the machine grips was 1.0 mm/s.

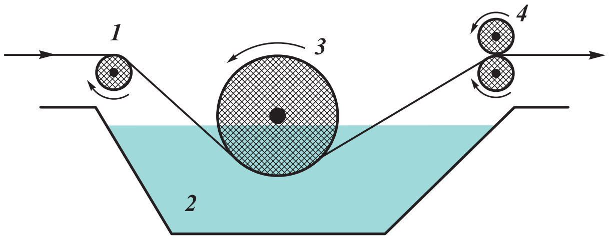

Fig. 1. Installation diagram for oiling continuous fibers

Рис. 1. Схема установки для замасливания непрерывных волокон

Fig. 2. Cylindrical mandrel with variable diameter

Рис. 2. Цилиндрическая оправка с переменным диаметром

The surface morphology of the oiled fibers was studied using a scanning electron microscope.

The flexural properties of the silicon carbide fibers with the applied oiling agent was evaluated by determining the minimum bending radius of the sample around a cylindrical mandrel with a variable diameter from 10 to 70 mm (Fig. 2). the sample was attached at one end to the surface of the measuring disc, wrapped around it in a pressed state, and held for 5 min. the minimum bending radius was considered to be the radius of the measuring disc preceding the one on which fiber breakage occurred.

Results and discussion

The use of acetone and isopropyl alcohol as solvents necessitated the use of low-molecular-weight polymethylsiloxane fluids: PMS-5, PMS-10, and PMS-20. During testing of these oiling agents, the treated fiber samples exhibited excessive brittleness, which was attributed to the removal of adsorbed moisture that contributed to the fiber surface's flexibility. This led to a significant increase in fuzzing and fiber breakage (Fig. 3).

The flexural test using a mandrel revealed that more than 80 % of the filaments were destroyed at the first stage, corresponding to a mandrel diameter of 70 mm.

Oiling compositions using acetone and isopropyl alcohol as solvents were found to be ineffective.

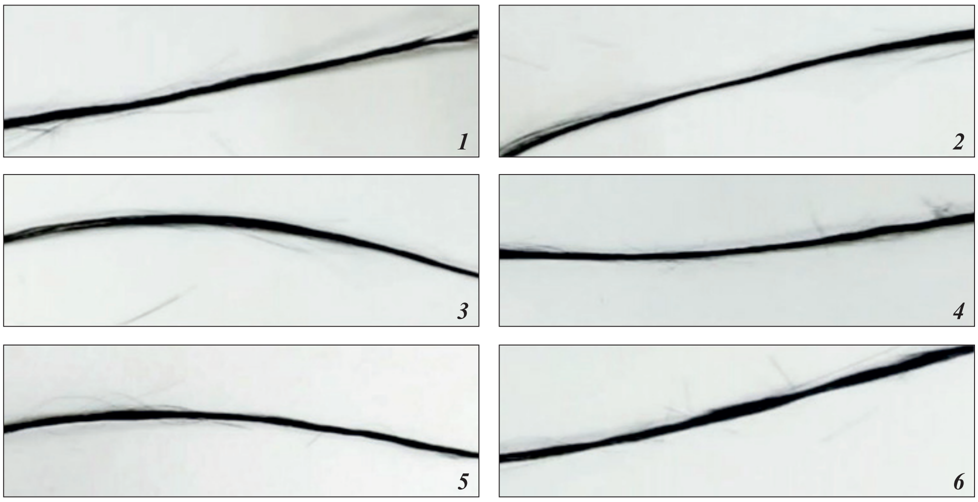

Fig. 3. Silicon carbide fibers with applied oiling agent

1, ***4*** – PMS-5; ***2***, ***5*** – PMS-10; ***3***, ***6*** – PMS-20
1–3 – solvent acetone; ***4–6*** – solvent isopropyl alcohol

Рис. 3. Карбидокремниевые волокна с нанесенным замасливателем

1, ***4*** – ПМС-5; ***2***, ***5*** – ПМС-10; ***3***, ***6*** – ПМС-20
1–3 – растворитель ацетон; ***4–6*** – растворитель изопропиловый спирт

In contrast, the use of oiling agents in the form of aqueous emulsions allowed for the application of higher molecular weight, more viscous fluids such as PMS-200. Silicone aqueous emulsions of PMS-200, and PMS-200 with the addition of polyvinyl alcohol (PVA), required the inclusion of dispersant IVP-317, which enhanced fiber wetting and contributed to the stabilization of the emulsion.

Oiling agents formulated with these components demonstrated high efficiency: uniform distribution (Fig. 4, *a*, *b*), effective wetting of the fiber surface,

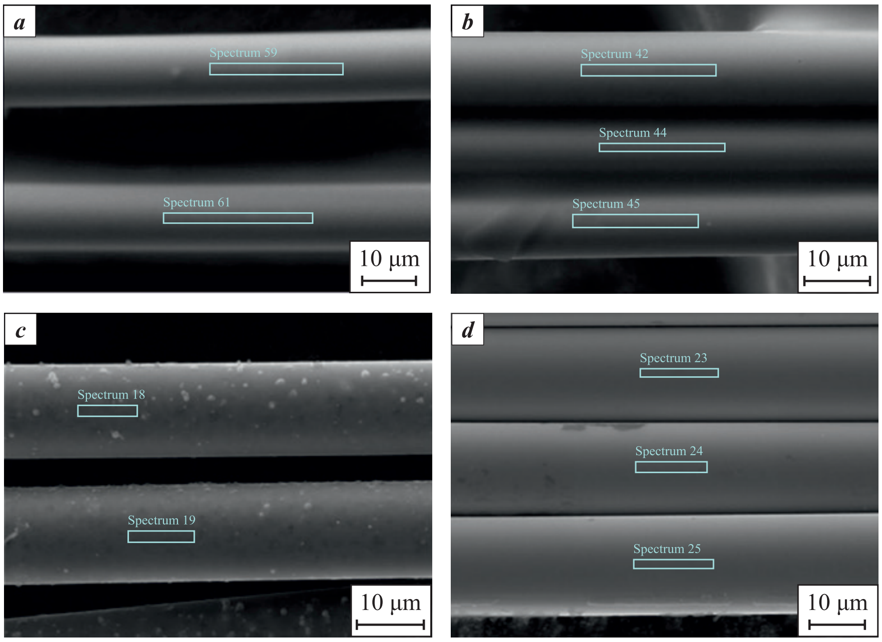

Fig. 4. Morphology of silicon carbide fiber surfaces with applied oiling agents (solvent – water)

a – PMS-200 emulsion; ***b*** – PMS-200 emulsion with PVA; ***c*** – PEG-400 solution (30 %); ***d*** – starch solution (10 %)

Рис. 4. Морфология поверхности карбидокремниевых волокон с нанесенными замасливателями (растворитель – вода)

a – эмульсия ПМС-200; ***b*** – эмульсия ПМС-200 с ПВС; ***c*** – раствор ПЭГ-400 (30 %); ***d*** – раствор крахмала (10 %)

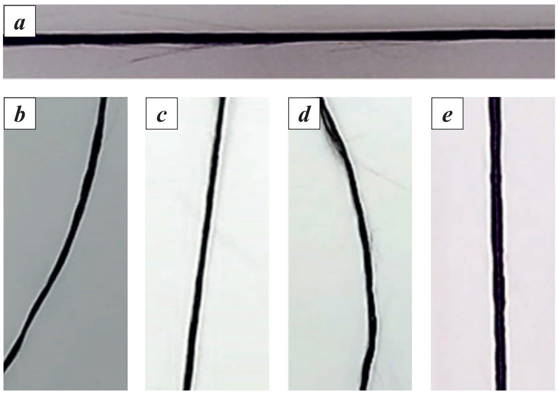

Fig. 5. Silicon carbide fibers

a – pure fibers in a bundle;
b–e after treatment with an aqueous emulsion PMS-200 (***b***), an aqueous emulsion of PMS-200 with the addition of polyvinyl alcohol (***c***), an aqueous solution of PEG-400 (30 %) (***d***), an aqueous solution of starch (10 %) (***e***)

Рис. 5. Карбидокремниевые волокна

a – чистые волокна в пучке;
b–e – после обработки водной эмульсией ПМС-200 (***b***), водной эмульсией ПМС-200 с добавлением поливинилового спирта (***c***), водным раствором ПЭГ-400 (30 %) (***d***), водным раствором крахмала (10 %) (***e***)

significant reduction in fuzzing, and improved bundle homogeneity (Fig. 5, *b*, *c*).

The addition of polyvinyl alcohol to the PMS-200 aqueous emulsion further enhanced the strength characteristics of the silicon carbide fibers and their overall technological properties (see Table).

Silicon carbide fibers treated with aqueous emulsions based on polymethylsiloxane (PMS-200 and PMS-200 with polyvinyl alcohol) showed a filament failure rate of no more than 1 % within the bundle when tested on a 10 mm mandrel, indicating improved suitability for textile processing (see Table).

In addition to silicone fluids, the study also examined an oiling composition containing an aqueous solution of polyethylene glycol PEG-400 (30 %). Fibers treated with this composition exhibited poor wetting, reduced oiling effectiveness compared to silicone fluids, and increased filament brittleness (Fig. 5, *d*). This may be attributed to the low affinity of the composition for silicon carbide fibers. During flexural testing on a cylindrical mandrel, more than 40 % of the filaments failed at the 40 mm diameter stage.

The aqueous starch solution (10 %) applied to the surface of the silicon carbide fibers demonstrated good distribution (Fig. 4, *d*), strong filament bonding within the bundle, reduced fuzzing (Fig. 5, *e*), and increased tensile strength (see Table). However, after drying, this composition caused excessive brittleness in the fibers, significantly reducing their technological suitability for further textile processing. Flexural testing using a mandrel showed that about 20 % of the filaments failed at the 60 mm diameter stage.

The Table below presents the test results for determining the minimum bending radius of oiled SiC fibers, their tensile strength relative to untreated fibers, and a description of the surface morphology.

Conclusions

The experimental study found that oiling agents using acetone and isopropyl alcohol as solvents led to a deterioration in the technological properties of the treated fibers, significantly increasing their brittleness and complicating their suitability for textile processing. the aqueous solution of polyethylene glycol (PEG-400) (30 %) was found to be ineffective due to poor distribution on the fiber surface and a reduction in the tensile strength of the treated samples (a 16 % decrease compared to untreated fibers). the best filament bundling and increased homogeneity were observed in samples treated with a 10 % aqueous starch solution. the tensile strength of these samples was

The effect of aqueous oiling compounds on the morphology and properties of SiC-fibers

Влияние водных замасливающих составов на морфологию и свойства SiC-волокон

Oiling liquid	Distribution on fiber surface (morphology)	Test results	
		Tensile strength of oiled fibers relative to pure fiber (100 % – baseline), %	Minimum bending radius when wound on a cylinder, mm
PMS-200 aqueous emulsion, IVP-317	uniform	62	15
PMS-200 aqueous emulsion, PVA, IVP-317	uniform	98	15
PEG-400 aqueous solution (30 %)	poor	84	50
Starch aqueous solution (10 %)	uniform	99	65

close to that of untreated fibers, with only a 1 % reduction. However, the increased brittleness of the fibers after drying significantly reduced their technological suitability, potentially causing difficulties in textile processing.

The study concluded that using oiling agents in the form of aqueous emulsions is the most effective method for treating coreless silicon carbide fibers. the best results were obtained with a PMS-200 emulsion containing polyvinyl alcohol and dispersant IVP-317, which improved flexural properties, reduced fuzzing, and enhanced the technological properties of the treated fibers, with only a slight decrease in tensile strength (2 % compared to untreated fibers). the use of the PMS-200 emulsion with IVP-317 also contributed to increased bundle homogeneity and flexural properties, although it did lead to a decrease in the tensile strength of the samples compared to untreated fibers.

The results suggest that aqueous emulsions based on polymethylsiloxane liquids and polyvinyl alcohol are the most effective for preparing coreless silicon carbide fibers for textile processing.

References / Список литературы

1. Bratukhin A.G., Sirotkin O.S., Sabodazh P.F., Egorov V.N. Materials of the future and their amazing properties. Moscow: Mashinostroenie, 1995. 127 p. (In Russ.).

   Братухин А.Г., Сироткин О.С., Сабодаж П.Ф., Егоров В.Н. Материалы будущего и их удивительные свойства. М.: Машиностроение, 1995. 127 с.
2. Bratukhin A.G., Ivanov Yu.L., Maryin B.N., Merkulov V.I., Dolotov B.I., Makarov K.A., Muravyev V.I. Modern technologies of aircraft construction. Moscow: Mashinostroenie, 1999. 832 p. (In Russ.).

   Братухин А.Г., Иванов Ю.Л., Марьин Б.Н., Меркулов В.И., Долотов Б.И., Макаров К.А., Муравьев В.И. Современные технологии авиастроения. М.: Машиностроение, 1999. 832 с.
3. Tyalina L.N., Minaev A.M., Pruchkin V.A. New composite materials. Tomsk: TGTU, 2011. 82 p. (In Russ.).

   Тялина Л.Н., Минаев А.М., Пручкин В.А. Новые композиционные материалы. Томск: ТГТУ, 2011. 82 с.
4. Bulanov I.M., Vorobey V.V. Technology of rocket and aerospace structures made of composite materials. Moscow: Bauman Moscow State Technical University, 1998. 516 p. (In Russ.).

   Буланов И.М., Воробей В.В. Технология ракетных и аэрокосмических конструкций из композиционных материалов. М.: МГТУ им. Н.Э. Баумана, 1998. 516 с.
5. Golubev I.S., Samarin A.V. Designing aircraft structures. Moscow: Mashinostroenie, 1991. 512 p. (In Russ.).

   Голубев И.С., Самарин А.В. Проектирование конструкций летательных аппаратов. М.: Машиностроение, 1991. 512 с.
6. Naslain Roger R. SiC-matrix composites: Nonbrittle ceramics for thermo-structural application. *International Journal of Applied Ceramic Technology*. 2005;2(2):75–84. https://doi.org/10.1111/j.1744-7402.2005.02009.x
7. Lewis D.A., Hogan M.T., McMahon J., Kinney S. Application of uncooled ceramic matrix composite power turbine blades for performance improvement of advanced turboshaft engines. In: *Proceedings of the 64th American Helicopter Society International Annual Forum* (Montreal, QC, Canada, April 29 – May 1, 2008). Vol. 2. P. 961–966.
8. DiCarlo J.A., Yun H.M., Morscher G.N., Bhatt R.T. SiC/SiC composites for 1200 °C and above. In: *Handbook of ceramic composites*. Boston: Kluwer Academic Publishers, 2005. P. 77–98. https://doi.org/10.1007/0-387-23986-3_4
9. DiCarlo J.A., Yun H.M., Morscher G.N., Bhatt R.T. Advanced SiC/SiC ceramic composites for air-breathing and rocket propulsion engine components. In: *Proceedings of JANNAF Conference* (Charleston, SC, June 15, 2005). P. 5–22.
10. DiCarlo J.A., Yun H.M., Bhatt R.T., Easler T. Advanced SiC/SiC ceramic composites for hot-section aerospace components. In: *Proceedings of National Space & Missile Materials Symposium* (Summerlin, NV, June 27 – July 1, 2005). P. 77–82.
11. Brentnall W.D., Van Roode M., Norton P.F., Gates S., Rice J.L., Jimenez O., Miriyala O. Ceramic gas turbine development at solar turbines incorporated. In: *Ceramic gas turbine design and test experience.* Vol. 1. Eds. M. Van Roode, M.K. Ferber, D.W. Richerson. N.Y.: ASME Press, 2002. P. 155–192.
12. Lamouroux F., Bouillon E., Cavalier J.C., Spriet P., Habarou G. An improved long life duration CMC for jet aircraft engine applications. In: *High temperature ceramic matrix composites.* Eds. W. Krenkel, R. Naslain, H. Schneider. Weinheim: Wiley-VCH, 2001. P. 783–788. https://doi.org/10.1002/3527605622.ch119
13. Dongming Zhu. Aerospace ceramic materials: Thermal, environmental barrier coatings and SiC/SiC ceramic matrix composites for turbine engine applications. *Materials Science*. 2018;219884.
14. Narottam P. Bansal, Jacques Lamon. Ceramic matrix composites: Materials, modeling and technology. New Jersey: the American Ceramic Society, 2015. 695 p.
15. Afanasov I.M., Lazoryak B.I. High-temperature ceramic fibers. Moscow: Lomonosov Moscow State University, 2010. 51 p. (In Russ.).

    Афанасов И.М., Лазоряк Б.И. Высокотемпературные керамические волокна. М.: МГУ им. М.В. Ломоносова, 2010. 51 с.
16. Berger M.H. Fine ceramic fibers: from microstructure to high temperature mechanical behavior. *Ceramic Transactions*. 2003;153:3–26. https://doi.org/10.1002/9781118406892.ch1
17. Schönfeld K. Interaction of fiber matrix bonding in SiC/SiC ceramic matrix composites. *Journal of the European Ceramic Society*. 2019;39(13):3557–3565. https://doi.org/10.1016/j.jeurceramsoc.2019.05.025
18. Christin F. Design, fabrication and application of C/C, C/SiC and SiC/SiC composites. In: *High temperature ceramic matrix composites*. Eds. W. Krenkel, R. Naslain,

H. Schneider. Weinheim: Wiley-VCH, 2001. P. 729–743. https://doi.org/10.1002/3527605622.ch112

19. Pakshver A.B., Mel'nikov B.N., Usenko V.A., Solov'ev A.N., Kukin G.N. Properties and features of chemical fiber processing. Ed. A.B. Pakshver. Moscow: Khimiya, 1975. 495 p. (In Russ.).

Пакшвер А.Б., Мельников Б.Н., Усенко В.А., Соловьев А.Н., Кукин Г.Н. Свойства и особенности переработки химических волокон. Под ред. А.Б. Пакшвера. М.: Химия, 1975. 495 с.

20. Frotsher G. Chemistry and physical chemistry of textile auxiliary materials. Vol. 2. Moscow: Gizlegprom, 1958. 200 p. (In Russ.).

Фротшер Г. Химия и физическая химия текстильных вспомогательных материалов. Т. 2. М.: Гизлегпром, 1958. 200 с.

21. Stepanova T.Yu. Emulsification as a method of modifying the properties of the surface of textile fibers. Ivanovo: IGKhTU, 2011. 118 p. (In Russ.).

Степанова Т.Ю. Эмульсирование как способ модификации свойств поверхности текстильных волокон. Иваново: ИГХТУ, 2011. 118 с.

22. Arabov J., G'ofurov Q., Rajapov O. the effect of emulsification of chemical fiber on the properties of yarn. *Textile Journal of Uzbekistan*. 2020;9(1):9.

23. Voronkov M.G., Makarskaya V.M. Appretirovanie textilnykh materialov. Novosibirsk: Nauka, 1978. 78 p. (In Russ.).

Воронков М.Г., Макарская В.М. Аппретирование текстильных материалов. Новосибирск: Наука, 1978. 78 с.

24. Filinkovskaya E.F., Serebryakova Z.G. Textile-auxiliary substances in the production of chemical fibers. Moscow: Khimiya, 1970. 265 p. (In Russ.).

Филинковская Е.Ф., Серебрякова З.Г. Текстильно-вспомогательные вещества в производстве химических волокон. М.: Химия, 1970. 265 с.

25. Nazarova M.V. Theoretical foundations of the processes of preparatory operations of weaving production. Volgograd: VolgGTU, 2015. 188 p. (In Russ.).

Назарова М.В. Теоретические основы процессов подготовительных операций ткацкого производства. Волгоград: ВолгГТУ, 2015. 188 с.

Information about the Authors

Darya V. Tsytsarkina – Process Engineer, JSC "Kompozit"
ORCID: 0009-0001-5867-4513
E-mail: tsytsarkinadv@inbox.ru

Pavel A. Timofeev – Cand. Sci. (Eng.), Head of the Department of Ceramic-matrix composite materials, JSC "Kompozit"
ORCID: 0000-0001-7448-8086
E-mail: 02421@kompozit-mv.ru

Сведения об авторах

Дарья Васильевна Цыцаркина – инженер-технолог, АО «Композит»
ORCID: 0009-0001-5867-4513
E-mail: tsytsarkinadv@inbox.ru

Павел Анатольевич Тимофеев – к.т.н., начальник отдела керамоматричных композиционных материалов, АО «Композит»
ORCID: 0000-0001-7448-8086
E-mail: 02421@kompozit-mv.ru

Contribution of the Authors

D. V. Tsytsarkina – defined the research objectives, prepared samples, conducted experiments, and authored the article.
P. A. Timofeev – provided scientific guidance and participated in the discussion of the results.

Вклад авторов

Д. В. Цыцаркина – определение цели работы, приготовление образцов, проведение экспериментов, написание статьи.
П. А. Тимофеев – научное руководство, участие в обсуждении результатов.

Received 24.11.2023
Revised 03.06.2024
Accepted 05.06.2024

Статья поступила 24.11.2023 г.
Доработана 03.06.2024 г.
Принята к публикации 05.06.2024 г.

Nanostructured Materials and Functional Coatings
Наноструктурированные материалы и функциональные покрытия

UDC 621.793

https://doi.org/10.17073/1997-308X-2024-5-37-43

Research article
Научная статья

Erosion resistance of ZrBN protective coatings deposited by reactive pulsed magnetron sputtering

A. D. Chertova[1], A. V. Levanov[2], B. B. Meshkov[3], E. A. Levashov[1], Ph. V. Kiryukhantsev-Korneev[1]

[1] **National University of Science and Technology "MISIS"**
1 Bld, 4 Leninskiy Prosp., Moscow 119049, Russia
[2] **M.V. Lomonosov Moscow State University**
4 Bld, 27 Lomonosovskiy Prosp., Moscow 119991, Russia
[3] **JSC "Research Institute of Technical Glass n.a. V.F. Solinov"**
5 Bld, 29 Krzhizhanovckiy Str., Moscow 117218, Russia

kiruhancev-korneev@yandex.ru

Abstract. ZrBN coatings were deposited by reactive pulsed magnetron sputtering using a ZrB_2 target while varying the pulse duration. The composition and structure of the coatings were studied using scanning and transmission electron microscopy, energy dispersive, optical emission and glow discharge Raman spectroscopy, as well as *X*-ray diffraction. Optical properties were studied by spectrophotometry. Erosion resistance was determined under laser exposure. All coatings were amorphous, had a dense, defect-free structure and a uniform distribution of elements throughout the thickness. According to Raman spectroscopy, the coatings contain B–N and Zr–N bonds. The coatings were characterized by high optical transmittance of 70–90 % in the wavelength range 450–1300 nm. The reflectivity of coatings was 9–26 %. The refractive index value increases from 1.7 to 3.0 as the wavelength increases from 200 to 1200 nm. The glass substrate is fragilely destroyed during erosion at a power of 20–60 W. All coatings successfully protect the glass substrate from erosive wear: the application of ZrBN coatings leads to a reduction in the width and depth of the erosion zone of the glass substrate by 1.3 and 4.5 times, respectively. The coating obtained at the optimal pulse duration has better erosion resistance, which may be due to its higher adhesive strength.

Keywords: pulsed magnetron sputtering, ZrBN, amorphous films, optical properties, erosion resistance

Acknowledgements: This work was carried out with the financial support of the Russian Science Foundation (project No. 24-13-00085).

For citation: Chertova A.D., Levanov A.V., Meshkov B.B., Levashov E.A., Kiryukhantsev-Korneev Ph.V. Erosion resistance of ZrBN protective coatings deposited by reactive pulsed magnetron sputtering. *Powder Metallurgy and Functional Coatings*. 2024;18(5):37–43. https://doi.org/10.17073/1997-308X-2024-5-37-43

Исследование эрозионной стойкости защитных покрытий ZrBN, осажденных методом реакционного импульсного магнетронного распыления

А. Д. Чертова[1], **А. В. Леванов**[2], **Б. Б. Мешков**[3],
Е. А. Левашов[1], **Ф. В. Кирюханцев-Корнеев**[1]

[1] **Национальный исследовательский технологический университет «МИСИС»**
Россия, 119049, г. Москва, Ленинский пр-т, 4, стр. 1
[2] **Московский государственный университет им. М. В. Ломоносова**
Россия, 119991, г. Москва, Ломоносовский пр-т, 27, к. 4
[3] **АО «Научно-исследовательский институт технического стекла им. В. Ф. Солинова»**
Россия, 117218, г. Москва, ул. Кржижановского, 29, к. 5

kiruhancev-korneev@yandex.ru

Аннотация. Покрытия ZrBN были получены методом реакционного импульсного магнетронного распыления с использованием мишени ZrB$_2$ при варьировании длительности импульса. Состав и структуру покрытий исследовали методами сканирующей и просвечивающей электронной микроскопии, энергодисперсионной спектроскопии, оптической эмиссионной спектроскопии тлеющего разряда и спектроскопии комбинационного рассеяния света, а также рентгенофазового анализа. Оптические свойства изучали методом спектрофотометрии. Эрозионную стойкость определяли при лазерном воздействии. Покрытия ZrBN были аморфными и характеризовались плотной бездефектной структурой и равномерным распределением элементов по толщине. По данным спектроскопии комбинационного рассеяния света, покрытия содержали связи B–N и Zr–N. Покрытия характеризовались высоким оптическим коэффициентом пропускания 70–90 % в диапазоне длин волн 450–1300 нм. Коэффициент отражения покрытий составлял 9–26 %. Значение показателя преломления повышалось от 1,7 до 3,0 при увеличении длины волны от 200 до 1200 нм. Эрозионные испытания показали, что подложка из стекла хрупко разрушается при воздействии лазера мощностью 20–60 Вт. Все покрытия успешно защищают стеклянную подложку от эрозионного износа: ширина и глубина зоны эрозии стеклянной подложки уменьшаются в 1,3 и 4,5 раза соответственно. Покрытие, полученное при оптимальной длительности импульса, обладает лучшей эрозионной стойкостью, что может быть обусловлено его более высокой адгезионной прочностью.

Ключевые слова: импульсное магнетронное распыление, аморфные покрытия, ZrBN, оптические свойства, эрозионная стойкость

Благодарности: Работа выполнена при финансовой поддержке Российского научного фонда (проект № 24-13-00085).

Для цитирования: Чертова А.Д., Леванов А.В., Мешков Б.Б., Левашов Е.А., Кирюханцев-Корнеев Ф.В. Исследование эрозионной стойкости защитных покрытий ZrBN, осажденных методом реакционного импульсного магнетронного распыления. *Известия вузов. Порошковая металлургия и функциональные покрытия*. 2024;18(5):37–43. https://doi.org/10.17073/1997-308X-2024-5-37-43

Introduction

One of the current challenges in the operation of optical equipment components (such as lenses, prisms, mirrors, interferometers, etc.) is wear due to erosion, which significantly affects their service life. Therefore, the development of optical coatings is an important direction in the creation of new precision optical devices [1]. These coatings must not only exhibit high transmittance and good reflectivity but also enhanced erosion resistance [2].

To protect optical device components exposed to wear, oxide coatings such as ZrO$_2$, Ta$_2$O$_5$, and others are commonly used. These coatings possess a wide transparent spectral range and high refractive indices [3; 4]. However, oxide coatings are characterized by relatively low hardness: 7 GPa for Nb$_2$O$_5$ [5], 8 GPa for TiO$_2$ [6], 10 GPa for SiO$_2$ [7], and 13 GPa for In$_2$O$_3$ [8]. They also show poor scratch resistance and have a high defect density in their structure, negatively impacting their wear resistance [9]. Recently, there has been growing interest in the study of transition metal nitrides, such as Ti, Zr, Cr, Nb, Mo, and Ta, which offer satisfactory optical properties combined with good wear resistance [10]. Comparative studies of TiN and TiAlN hard coatings have demonstrated that aluminum alloying enhances wear resistance under thermal stress conditions [11]. Among TiN, HfN, and ZrN coatings, zirconium nitride coatings exhibit superior optical properties [12]. Introducing boron into ZrN coatings can improve hardness, wear resistance, and optical characteristics.

Previously, we developed wear-resistant ZrBN coatings with high thermal stability and an optical transmittance of up to 90 % [13], which was associated with a high volume fraction of the BN phase. We established the influence of pulse frequency and duration during the deposition of ZrBN coatings using pulsed magnetron sputtering (PMS) on their structure, optical properties, hardness, elastic-plastic characteristics, and wear resistance under friction, sliding, and abrasive conditions [14; 15]. However, the protective properties of ZrBN coatings under erosion conditions require further investigation. It is important to note that ZrBN coatings serve as an excellent model composition, which can serve as the basis for developing more complex multicomponent structures based on advanced heterophase ceramics in the future [16].

The aim of this study is to investigate the structure, optical properties, and erosion resistance of ZrBN coatings deposited by PMS.

Materials and methods

Zr–B–N coatings were deposited using reactive pulsed magnetron sputtering (PMS) with a ZrB_2 target. The deposition was performed using a setup based on the UVN-2M vacuum system, the schematic of which is described in [17]. Nitrogen (99.999 % purity) was used as the working gas, with a pressure of 0.1–0.2 Pa.

The magnetron was powered by a Pinnacle Plus 5×5 unit (Advanced Energy, USA), with a power output of 1 kW, a current of 2 A, and a voltage in the range of 400–500 V. The frequency was set at 350 kHz, and the pulse durations were 0.4 μs (coating *1*), 0.7 μs (coating *2*), and 1.1 μs (coating *3*). The sputtering process lasted for 40 min.

Colorless optical glass plates (K8) were used as substrates. Before coating deposition, the substrates were cleaned in an ultrasonic bath for 5 min in isopropyl alcohol. Ion cleaning of the substrates was performed using an Ar^+ on beam from a slit-type ion source at an accelerating voltage of 2.5 kV for 20 min. The coating deposition time was 40 min.

The structural analysis of the coatings was conducted using scanning electron microscopy (SEM) and energy-dispersive spectroscopy (EDS) on a Hitachi S-3400N microscope equipped with a NORAN 7 Thermo system. Transmission electron microscopy (TEM) was performed on a JEM-2100 microscope (Jeol). Glow discharge optical emission spectrometry (GD-OES) was carried out using the PROFILER-2 system (Horiba Jobin Yvon) [18]. TEM samples were prepared by ion milling using a PIPS II dual-beam precision ion polishing system (Gatan Inc., USA). Raman spectra were obtained with a LabRam HR800 system (Horiba JY) equipped with a 514 nm green laser source. *X*-ray phase analysis (XRD) was conducted using CuK_α radiation ($\lambda = 0.154$ nm) on a Phaser D2 diffractometer (Bruker). Optical properties were measured over a wavelength range of 380–1300 nm using a Photon-RT spectrophotometer.

The erosion resistance of the coatings was tested on a LaserPRO Spirit laboratory setup. The CO_2 laser power was set at 20, 40, and 60 W. The length of the laser track and exposure time were 10 mm and 2 s, respectively. The tracks were examined using an Axiovert 25 optical microscope (Carl Zeiss) and a WYKO-NT1100 optical profilometer (Veeco).

Results and discussion

All elements in the coatings were uniformly distributed throughout their depth, with impurity levels (C and O) ranging from 0.7 to 1.8 at. %. The coatings, regardless of pulse duration, had a similar elemental composition, at. %: 14 ± 2 Zr, 46 ± 2 B, and 40 ± 2 N. The thickness and growth rate of the coatings were 1.3–1.5 μm and 32–39 nm/min, respectively. The Zr–B–N coatings exhibited a dense, homogeneous structure without the characteristic columnar elements typical of nitrogen-containing ion-plasma coatings [19].

Fig. 1 shows a typical electron diffraction pattern, a bright-field image of the structure, an *X*-ray diffraction pattern, and a Raman scattering spectrum for coating *2*.

The electron diffraction pattern (Fig. 1, *a*) shows a broad ring, indicating the presence of an amorphous phase. The *X*-ray diffraction pattern (Fig. 1, *b*) displays a halo in the $2\theta = 20{\div}40°$ range, further confirming the amorphous nature of the coatings. Raman spectroscopy (Fig. 1, *c*) was used to clarify the phase composition of the coatings. The spectrum shows pronounced peaks at 1360 and 1490 cm^{-1}, which can be attributed to the BN phase [20]. In the 600–1200 cm^{-1} wavelength range, peaks corresponding to the ZrN phase are observed [21].

Fig. 2, *a* and *b* present the spectral-angular dependencies of the transmittance (*T*) and reflectance (*R*) coefficients as a function of wavelength (λ) for coating *2*. The *T* and *R* spectra exhibit an oscillatory character, which is associated with interference effects. The ZrBN coatings showed a transmittance of 70÷87 % in the 450–1300 nm wavelength range (Fig. 2, *a*). At the same time, the *R* values ranged from 9 to 26 %, depending on the wavelength. It is worth noting that the transmittance of ZrBN coatings is comparable to that of traditional oxide coatings such as Zr–O, Zr–Al–O, and ZrSiN nitride-based coatings ($T = 70{\div}90$ %) [22; 23].

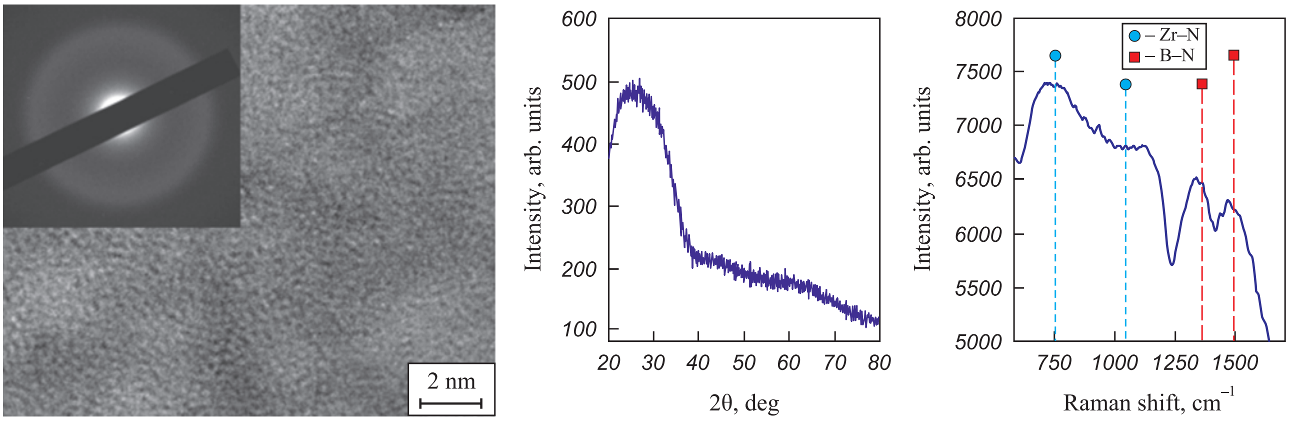

a *b* *c*

Fig. 1. BF TEM image, SAED (***a***), XRD pattern (***b***), and Raman spectra (***c***) for coating *2*

Рис. 1. Светлопольное изображение структуры и электронограмма (***a***), рентгенограмма (***b***) и спектр комбинационного рассеяния света (***c***) для покрытия *2*

The interference nature of the transmittance and reflectance curves allowed the determination of the dispersion dependence of the refractive index (*n*) (Fig. 2, *c*). As the wavelength increased from 400 to 900 nm, the refractive index gradually decreased from 2.29 to 2.06, indicating strong absorption of visible light due to free electrons and weaker absorption of infrared radiation. It is worth noting that ZrN coatings exhibit weaker visible light absorption, with the refractive index increasing from 1.7 to 3.0 as the wavelength increases from 200 to 1200 nm [19].

SEM images of the surface of the uncoated substrate and coatings *1*–*3* after erosion exposure at 20 W power are shown in Fig. 3, *a*. The track width for the uncoated substrate was 222 μm. The application of coatings *1*, *2*, and *3* reduced the track width by 5, 7, and 21 %, respectively. At increased powers of 40 and 60 W (Figs. 3, *b* and *c*), the uncoated substrate exhibited crack formation and chipping along the track boundaries, whereas no cracks or delamination were observed in the coatings tested under the same conditions. Coating *3* had the smallest track width, measuring 222 and 237 μm at powers of 40 and 60 W, respectively, while the substrate had values of 292 and 296 μm (Fig. 3).

Thus, the application of coating *3* reduced the track width by 1.3 times compared to the uncoated glass substrate.

The tracks after erosion exposure were also analyzed using optical profilometry, with the most prominent results shown in Fig. 4. The two-dimensional profiles reveal that the uncoated glass substrate is unevenly damaged. More intense material degradation occurs at the final moment of scanning (Fig. 4, *a*, marked by an arrow). This effect may be due to the increased brittleness, low thermal stability, and low thermal conductivity of the glass substrate. The maximum depth at the center of the track was ~9 μm (Fig. 4, *a*).

For the ZrBN coatings, as exemplified by sample *3* (Fig. 4, *b*), no brittle fracture was observed, and the track was uniform.

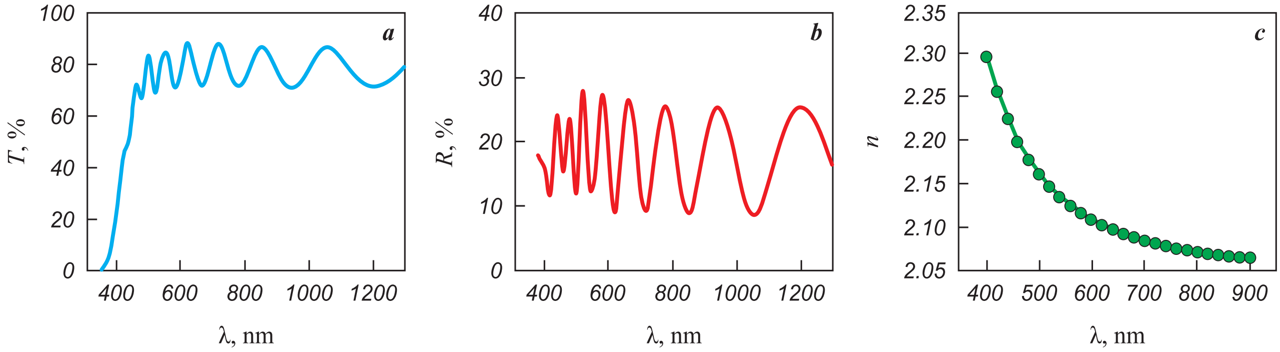

Fig. 2. Transmittance (***a***), reflection (***b***), and the refractive index (***c***) of coating *2*

Рис. 2. Коэффициенты оптического пропускания (***a***) и отражения (***b***), показатель преломления (***c***) для покрытия *2*

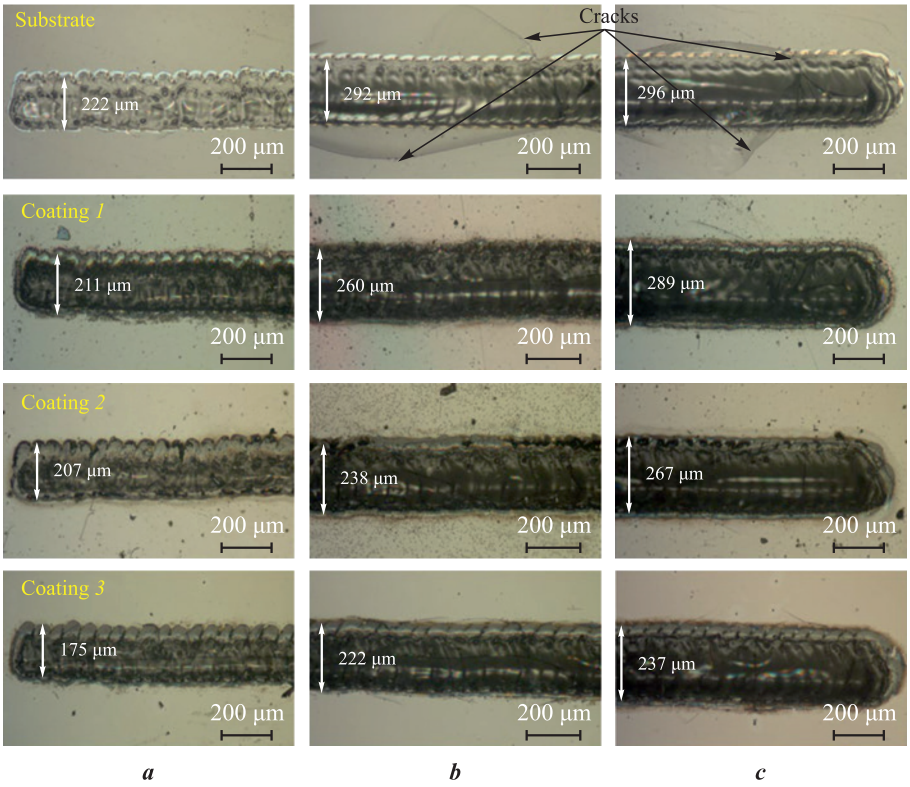

Fig. 3. SEM-images of tracks after erosion test for uncoated substrate and ZrBN coatings *1*, *2*, *3* for 20 (***a***), 40 (***b***) and 60 (***c***) W

Рис. 3. СЭМ-изображения дорожек после эрозионных испытаний для непокрытой подложки и покрытий ZrBN *1*, *2*, *3* при мощности эрозионного воздействия 20 (***a***), 40 (***b***) и 60 (***c***) Вт

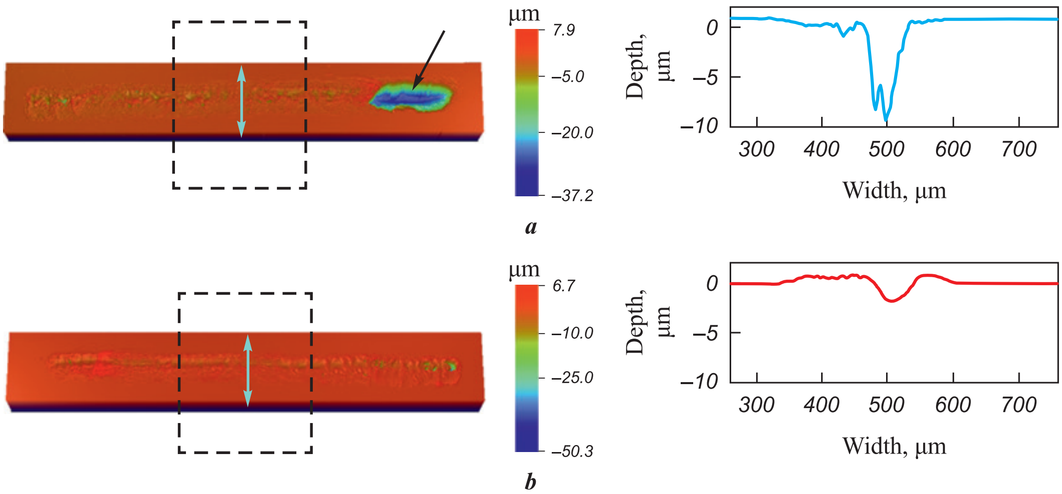

Fig. 4. 3D and 2D track profiles after erosion test for uncoated substrate (***a***) and coating *3* (***b***)

Fig. 4. 3D и 2D-профили дорожек после эрозионных испытаний для непокрытой подложки (***a***) и покрытия *3* (***b***)

The maximum track depth at the center for all coatings was around 2 µm, which is 4.5 times lower than the values obtained for the uncoated glass substrate.

Thus, all coatings successfully protect the glass substrate from erosion. Coating *3* demonstrated the best resistance, likely due to its higher crack resistance and adhesion strength [15].

Conclusion

Amorphous ZrBN coatings with a thickness of 1.3–1.5 µm were deposited using pulsed magnetron sputtering with varying pulse durations. The coatings exhibited a dense, homogeneous structure. The transmittance and reflectance coefficients in the 450–1300 nm wavelength range were 70–87 %

and 9–26 %, respectively. The refractive index ranged from 2.29 to 2.06 in the $\lambda = 400–900$ nm range. Erosion resistance tests revealed that the glass substrate cracked and degraded significantly during the experiments. However, the application of ZrBN coatings prevented substrate cracking and reduced the width and depth of the erosion zone by 1.3 and 4.5 times, respectively.

References / Список литературы

1. Hu C., Guo K., Li Y., Gu Z., Quan J., Zhang S., Zheng W. Optical coatings of durability based on transition metal nitrides. *Thin Solid Films*. 2019;688:137339.
https://doi.org/10.1016/j.tsf.2019.05.058

2. Mishra S.K., Kumar V., Tiwari S.K., Mishra T., Angula G., Adhikari S. Development and degradation behavior of protective multilayer coatings for aluminum reflectors for solar thermal applications. *Thin Solid Films*. 2016;619:202–207.
https://doi.org/10.1016/j.tsf.2016.10.067

3. Zhu Y., Ma M., Zhang P., Cai W., Li D., Xu C. Preparation of sol-gel ZrO_2 films with high laser-induced damage threshold under high temperature. *Optics Express*. 2019;27(26):37568–37578.
https://doi.org/10.1364/OE.27.037568

4. Zhang P., Lin D., Zhu Y., Cai W., Li D., Xu C. *In-situ* high temperature laser-induced damage of sol-gel Ta_2O_5 films with different dual additives. *Thin Solid Films*. 2020;693:137723.
https://doi.org/10.1016/j.tsf.2019.137723

5. Mazur M., Szymańska M., Kaczmarek D., Kalisz M., Wojcieszak D., Domaradzki J., Placido F. Determination of optical and mechanical properties of Nb_2O_5 thin films for solar cells application. *Applied Surface Science*. 2014;301:63–69.
https://doi.org/10.1016/j.apsusc.2014.01.144

6. Krishna D.S.R., Sun Y., Chen Z. Magnetron sputtered TiO_2 films on a stainless steel substrate: selective rutile phase formation and its tribological and anti-corrosion performance. *Thin Solid Films*. 2011;519(15):4860–4864.
https://doi.org/10.1016/j.tsf.2011.01.042

7. Mazur M., Wojcieszak D., Kaczmarek D., Domaradzki J., Song S., Gibson D., Placido F., Mazur P., Kalisz M., Poniedzialek A. Functional photocatalytically active and scratch resistant antireflective coating based on TiO_2 and SiO_2. *Applied Surface Science*. 2016;380:165–171.
https://doi.org/10.1016/j.apsusc.2016.01.226

8. Yang L., Zhu J., Bai J., Zhu Y., Dai B., Yu H., Jia Z., Han J. Plasma exposure inducing crystallization of indium oxide film with improved electrical and mechanical properties at room temperature. *Journal of Materials Science*. 2014;49:5955–5960.
https://doi.org/10.1007/S10853-014-8314-0

9. Fryauf D.M., Phillips A.C., Kobayashi N.P. Corrosion barriers for silver-based telescope mirrors: comparative study of plasma-enhanced atomic layer deposition and reactive evaporation of aluminum oxide. *Journal of Astronomical Telescopes, Instruments, and Systems*. 2015;1(4):044002.
https://doi.org/10.1117/1.JATIS.1.4.044002

10. Gaković B.M., Trtica M., Nenadović T., Gredić T. Transversely excited atmospheric CO_2 laser-induced damage of TiN and (Ti,Al)N coatings. *Applied Surface Science*. 1999;143(1-4):78–84.
https://doi.org/10.1016/S0169-4332(98)00903-9

11. Jafari M., Rogström L., Andersson J.M., Birch J., Gibmeier J., Jöesaar M.J., Kiefer D., Odén M. Thermal degradation of TiN and TiAlN coatings during rapid laser treatment. *Surface and Coatings Technology*. 2021;422:127517.
https://doi.org/10.1016/j.surfcoat.2021.127517

12. Patsalas P. Zirconium nitride: A viable candidate for photonics and plasmonics? *Thin Solid Films*. 2019;688:137438.
https://doi.org/10.1016/j.tsf.2019.137438

13. Kiryukhantsev-Korneev P.V., Sytchenko A.D., Kozlova N.S., Zabelina E.V., Skryleva E.A., Kaplansky Y.Y., Vakhrushev R.A., Levashov E.A. Structure and properties of protective amorphous ZrBN coating. *Surface and Coatings Technology*. 2022;448:128849.
https://doi.org/10.1016/j.surfcoat.2022.128849

14. Kiryukhantsev-Korneev P.V., Levashov E.A. Transparency effect in Zr−B−N coatings obtained by magnetron sputtering of ZrB_2 target. *Technical Physics Letters*. 2020;46(2):179–181.
https://doi.org/10.1134/S1063785020020224

15. Kiryukhantsev-Korneev P.V., Sytchenko A.D., Levashov E.A. The effect of pulse duration on the structure and mechanical, tribotechnical, and optical characteristics of Zr–B–N coatings obtained by the PMS method. *Protection of Metals and Physical Chemistry of Surfaces*. 2021;57(6):1222–1230.
https://doi.org/10.1134/S2070205121060125

16. Houska J., Steidl P., Vlcek J., Martan J. Thermal, mechanical and electrical properties of hard B_4C, BCN, ZrBC and ZrBCN ceramics. *Ceramics International*. 2016; 42(3):4361-4369.
https://doi.org/10.1016/j.ceramint.2015.11.115

17. Kiryukhantsev-Korneev P.V., Sytchenko A.D., Sviridova T.A., Sidorenko D.A., Andreev N.V., Klechkovskaya V.V., Polčak J., Levashov E.A., Effects of doping with Zr and Hf on the structure and properties of Mo–Si–B coatings obtained by magnetron sputtering of composite targets. *Surface and Coatings Technology*. 2022;442: 128141. https://doi.org/10.1016/j.surfcoat.2022.128141

18. Kiryukhantsev-Korneev P.V. Elemental analysis of coatings by high-frequency glow discharge optical emission spectroscopy. *Protection of Metals and Physical Chemistry of Surfaces*. 2012;48(5):585–590.
https://doi.org/10.1134/S207020511205005X

Кирюханцев-Корнеев Ф.В. Анализ элементного состава покрытий с использованием высокочастотной оптической эмиссионной спектроскопии тлеющего разряда. *Физикохимия поверхности и защита материалов*. 2012;48(5):488–494.

19. Pilloud D., Dehlinger A.S., Pierson J.F., Roman A., Pichon L. Reactively sputtered zirconium nitride coatings: structural, mechanical, optical and electrical characteristics. *Surface and Coatings Technology*. 2003; 174–175:338–344.
https://doi.org/10.1016/S0257-8972(03)00613-3

20. Chang J., Zhang H., Cao J. Ultrahigh sensitive and selective triethylamine sensor based on h-BN modified MoO_3 nanowires. *Advanced Powder Technology*. 2022;33(2): 103432. https://doi.org/10.1016/j.apt.2022.103432

21. Rizzo A., Valerini D., Capodieci L., Mirenghi L., Di Benedetto F., Protopapa M.L. Reactive bipolar pulsed dual magnetron sputtering of ZrN films: the effect of duty cycle. *Applied Surface Science*. 2018;427(A):994–1002. https://doi.org/10.1016/j.apsusc.2017.08.032

22. Musil J., Sklenka J., Cerstvy R. Transparent Zr–Al–O oxide coatings with enhanced resistance to cracking. *Surface and Coatings Technology*. 2012;206(8-9):2105–2109. https://doi.org/10.1016/j.surfcoat.2011.09.035

23. Pilloud D. Influence of the silicon concentration on the optical and electrical properties of reactively sputtered Zr–Si–N nanocomposite coatings. *Materials Science and Engineering: B*. 2006;131(1-3):36–39. https://doi.org/10.1016/j.mseb.2006.03.017

Information about the Authors

Alina D. Chertova – Cand. Sci. (Eng.), Junior Research Scientist of the Laboratory "*In situ* Diagnostics of Structural Transformations" of Scientific-Educational Center of Self-Propagating High-Temperature Synthesis (SHS-Center) MISIS–ISMAN, National University of Science and Technology "MISIS" (NUST "MISIS")
ORCID: 0000-0002-8668-5877
E-mail: alina-sytchenko@yandex.ru

Alexander V. Levanov – Cand. Sci. (Chem.), Associate Professor of the Department of Chemistry, M.V. Lomonosov Moscow State University
ORCID: 0000-0003-1529-717X
E-mail: chem.alexander@yandex.ru

Boris B. Meshkov – Cand. Sci. (Eng.), Head of the Optical Coatings Laboratory, JSC "Research Institute of Technical Glass n. a. V. F. Solinov"
E-mail: meshkov-bb@yandex.ru

Evgeniy A. Levashov – Dr. Sci. (Eng.), Prof., Acad. of the Russian Academy of Natural Science, Head of the Department of Powder Metallurgy and Functional Coatings (PM&FC) NUST "MISIS", Director of SHS-Center of MISIS–ISMAN
ORCID: 0000-0002-0623-0013
E-mail: levashov@shs.misis.ru

Philipp V. Kiryukhantsev-Korneev – Dr. Sci. (Eng.), Professor of the Department of PM&FC of NUST "MISIS", Head of the Laboratory «*In situ* Diagnostics of Structural Transformations" of SHS-Center of MISIS–ISMAN
ORCID: 0000-0003-1635-4746
E-mail: kiruhancev-korneev@yandex.ru

Сведения об авторах

Алина Дмитриевна Чертова – к.т.н, мл. науч. сотрудник лаборатории «*In situ* диагностика структурных превращений» Научно-учебного центра (НУЦ) СВС МИСИС–ИСМАН, Национальный исследовательский технологический университет «МИСИС» (НИТУ МИСИС)
ORCID: 0000-0002-8668-5877
E-mail: alina-sytchenko@yandex.ru

Александр Владимирович Леванов – к.х.н, доцент химического факультета МГУ им. М.В. Ломоносова
ORCID: 0000-0003-1529-717X
E-mail: chem.alexander@yandex.ru

Борис Борисович Мешков – к.т.н., начальник лаборатории оптических покрытий АО «Научно-исследовательский институт технического стекла им. В. Ф. Солинова»
E-mail: meshkov-bb@yandex.ru

Евгений Александрович Левашов – д.т.н., проф., акад. РАЕН, зав. кафедрой порошковой металлургии и функциональных покрытий (ПМиФП) НИТУ МИСИС, директор НУЦ СВС МИСИС–ИСМАН
ORCID: 0000-0002-0623-0013
E-mail: levashov@shs.misis.ru

Филипп Владимирович Кирюханцев-Корнеев – д.т.н., профессор кафедры ПМиФП НИТУ МИСИС, зав. лабораторией «*In situ* диагностика структурных превращений» НУЦ СВС МИСИС–ИСМАН
ORCID: 0000-0003-1635-4746
E-mail: kiruhancev-korneev@yandex.ru

Contribution of the Authors

A. D. Chertova – conducting structural studies, analysis of research results, preparation of the text, formulation of conclusions.
A. V. Levanov – Raman study.

B. B. Meshkov – study of optical properties.
E. A. Levashov – tasks establishing, correction of manuscript and conclusions.
Ph. V. Kiryukhantsev-Korneev – coating deposition by magnetron sputtering, correction of manuscript, discussion of the results, general management.

Вклад авторов

А. Д. Чертова – проведение структурных исследований, анализ результатов исследований, подготовка текста статьи.
А. В. Леванов – проведение исследований методом комбинационного рассеяния света.
Б. Б. Мешков – исследование оптических свойств.
Е. А. Левашов – постановка цели, корректировка текста статьи, формулировка выводов.
Ф. В. Кирюханцев-Корнеев – нанесение покрытий методом магнетронного распыления, корректировка текста, обсуждение результатов, общее руководство.

Received 05.09.2024
Revised 24.09.2024
Accepted 26.09.2024

Статья поступила 05.09.2024 г.
Доработана 24.09.2024 г.
Принята к публикации 26.09.2024 г.

Nanostructured Materials and Functional Coatings
Наноструктурированные материалы и функциональные покрытия

UDC 621.791.927.5 + 620.178.165

https://doi.org/10.17073/1997-308X-2024-5-44-54

Research article
Научная статья

Formation of wear-resistant coatings during electric arc surfacing with ultrasonic vibrations

D. V. Priyatkin ✉, A. A. Artem'ev, V. I. Lysak

Volgograd State Technical University
28 Lenin Prosp., Volgograd 400005, Russia

✉ priyatkin.dv@mail.ru

Abstract. The study focuses on investigating the influence of ultrasonic vibrations introduced into the crystallizing metal of the weld pool through filler wire during automated electric arc surfacing with flux-cored wire, on the formation characteristics of a wear-resistant coating made from the 280Cr14Mn6Ni6Mo3Ti2Nb2 alloy. The effect of ultrasonic vibrations on the structural-phase composition, hardness, and wear resistance of the surfaced coating is analyzed, particularly under normal and elevated temperatures up to 600 °C in conditions of exposure to a gas-abrasive flow. The failure pattern of the thin surface layers of the worn coatings is also studied. It was established that the microstructure of the coating consists of a carbide eutectic based on austenite, which possesses increased ductility and sufficiently high strength due to alloying with chromium and molybdenum. This ensures reliable retention of reinforcing phases represented by Mo_2C, $(Ti,Nb,Mo)_xC_y$, and Me_xC_y carbides. It is shown that under the influence of high-frequency acoustic vibrations, large primary Me_xC_y carbides disappear from the alloy structure, the volume fraction of austenite increases by 25 %, and the proportion of Me_xC_y-type carbides decreases. Additionally, a redistribution of alloying elements between the austenite and carbide phases is observed. The formation of a fine lamellar eutectic leads to changes in the wear mechanism of the alloy: hard solution layers dampen shear deformations caused by impacts of abrasive particles, while the plastic flow of the austenitic matrix forms a metallic binder around the broken carbide fragments, reducing the likelihood of their detachment. This results in an 18 % increase in the alloy's resistance to high-temperature gas-abrasive wear, surpassing the performance of an international industrial counterpart.

Keywords: wear-resistant coatings, carbides, austenite, electric arc surfacing, ultrasonic vibrations, filler wire, high-temperature gas-abrasive wear

Acknowledgements: This research was supported by a grant from the Russian Science Foundation No. 23-13-00354, https://rscf.ru/project/23-13-00354.

For citation: Priyatkin D.V., Artem'ev A.A., Lysak V.I. Formation of wear-resistant coatings during electric arc surfacing with ultrasonic vibrations. *Powder Metallurgy and Functional Coatings*. 2024;18(5):44–54. https://doi.org/10.17073/1997-308X-2024-5-44-54

Формирование износостойких покрытий в процессе электродуговой наплавки с ультразвуковыми колебаниями

Д. В. Прияткин ✉, А. А. Артемьев, В. И. Лысак

Волгоградский государственный технический университет
Россия, 400005, г. Волгоград, пр. им. В.И. Ленина, 28

✉ priyatkin.dv@mail.ru

Аннотация. Исследование посвящено изучению влияния ультразвуковых колебаний, вводимых в кристаллизующийся металл сварочной ванны через присадочную проволоку в процессе автоматической электродуговой наплавки порошковой проволокой, на особенности формирования износостойкого покрытия из сплава 280Х14Г6Н6М3Т2Б2. Выявлено влияние ультразвуковых колебаний на структурно-фазовый состав и твердость наплавленного покрытия, а также его износостойкость при нормальной и повышенной до 600 °С температурах в условиях воздействия газоабразивного потока. Изучен характер разрушения тонких поверхностных слоев изношенных покрытий. Установлено, что микроструктура покрытия состоит из карбидной эвтектики на основе аустенита, обладающего повышенной пластичностью и достаточно высокой прочностью за счет легирования хромом и молибденом, что способствует надежному закреплению в нем упрочняющих фаз, представленных карбидами Mo_2C, $(Ti,Nb,Mo)_xC_y$ и Me_xC_y. Показано, что под действием высокочастотных акустических колебаний в структуре сплава исчезают крупные первичные карбиды Me_xC_y, на 25 % увеличивается объемная доля аустенита при снижении доли карбидов типа Me_xC_y, а также наблюдается перераспределение легирующих элементов между аустенитом и карбидной фазой. Установлено, что формирование тонкопластинчатой эвтектики обусловливает изменения в механизме изнашивания сплава: прослойки твердого раствора демпфируют сдвиговые деформации при ударах абразивных частиц, а пластическое течение аустенитной матрицы формирует вокруг образующихся обломков карбидов металлическую связку, снижая вероятность их выкрашивания. Это способствует повышению на 18 % стойкости сплава к высокотемпературному газоабразивному изнашиванию, которая превосходит показатель зарубежного промышленного аналога.

Ключевые слова: износостойкие покрытия, карбиды, аустенит, электродуговая наплавка, ультразвуковые колебания, присадочная проволока, высокотемпературное газоабразивное изнашивание

Благодарности: Исследование выполнено за счет гранта Российского научного фонда № 23-13-00354, https://rscf.ru/project/23-13-00354.

Для цитирования: Прияткин Д.В., Артемьев А.А., Лысак В.И. Формирование износостойких покрытий в процессе электродуговой наплавки с ультразвуковыми колебаниями. *Известия вузов. Порошковая металлургия и функциональные покрытия*. 2024;18(5):44–54. https://doi.org/10.17073/1997-308X-2024-5-44-54

Introduction

Industrial equipment during operation is subjected to abrasive wear, which significantly reduces its service life by altering the size, shape, and condition of the working surfaces of parts [1; 2]. For instance, components of industrial fans, draft machines, solid-fuel boilers, and gas turbine units are exposed to abrasive particles carried by high-speed flows of heated gases. The need to replace wornout parts leads to substantial economic losses due to prolonged equipment downtime during repairs [2–4]. Extending the service life of parts can be achieved efficiently by strengthening their surface with wear-resistant alloys [4; 5].

One of the key kinematic parameters determining the nature and intensity of the wear surface destruction is the angle of its attack by the gas-abrasive flow [6; 7]. At small attack angles (20–30°) and temperatures up to 600 °C, typical for the operation of forced draft fans, the surface destruction mechanism is dominated by plastic displacement of the metal and microcutting, which leads to low wear resistance of ductile materials [8–10]. Under these conditions, alloys based on iron with a composite structure, consisting of both large and fine hard carbides distributed throughout a ductile matrix, are more preferable [11; 12].

The task of obtaining thick wear-resistant coatings on the surface of parts is most universally and effectively solved by electric arc surfacing with flux-cored wire [1; 13]. The use of flux-cored wire allows the production of coatings with virtually any chemical composition, providing them with the necessary operational properties [14; 15]. Dynamic exposure to ultrasonic vibrations (from 18 kHz) on the alloys crystallizing during the surfacing process is one of the known technological methods that allows altering their structural-phase composition, increasing wear resistance, reducing the likelihood of internal defects, and more [16–18].

These changes are caused by the formation of standing waves in the melt, characterized by alternating regions of compression and rarefaction. The generation of high energy densities in these regions manifests in secondary effects (cavitation, acoustic flows, radiation pressure, viscous friction forces), creating specific conditions for the crystallization of the metallic melt [19; 20]. These effects contribute to the intensification of physical and chemical processes: degassing, diffusion, metal structure dispersion, phase coagulation, and others [21; 22].

Among all known methods of transmitting ultrasonic vibrations (USV) to the crystallizing melt in the weld pool, using filler (waveguide) wire for this purpose is of the greatest practical interest [23]. In this case, it becomes possible to affect the melt near the crystallization front, where the acoustic treatment has the most noticeable effect. Using flux-cored wire as a waveguide allows for alloying, reinforcing, and modifying the surfaced metal with refractory particles, while the USV can contribute to their more uniform distribution within the melt [24; 25]. At the same time, it is necessary to note that the relationships between the influence of USV on the structure and properties of the surfaced wear-resistant alloys have not been fully explored in scientific and technical publications.

The objective of this study is to investigate the influence of USV on the structural-phase composition and resistance to gas-abrasive wear at temperatures up to 600 °C of a coating made from the experimental alloy 280Cr14Mn6Ni6Mo3Ti2Nb2, surfaced by the electric arc method.

Materials and methods

During the formation of the wear-resistant coating by electric arc surfacing in a protective gas, an experimental flux-cored wire (FCW) with a diameter of 2.8 mm was used as the electrode. A strip of 08kp steel (low-carbon killed steel, ~0.08 % C) with a thickness of 0.25 mm was used as the sheath for the FCW, and the filler material of the wire consisted of metallic powders of chromium, nickel, molybdenum, niobium, titanium, iron, as well as graphite powder. The composition of the filler was calculated to achieve a eutectic structure in the surfaced alloy, featuring a tough and ductile austenitic matrix stabilized by carbon, nickel, and manganese, capable of securely retaining hard phases in the form of chromium, titanium, niobium, and molybdenum carbides [26].

A wear-resistant coating was formed in a single layer of 6–7 mm thickness on the surface of plates made of St3sp steel, with the following chemical composition (wt. %):

C	2.7–2.9	Mo	3.0–3.14
Cr	13.5–15.0	Nb	2.0–2.1
Ni	5.7–6.0	Ti	2.0–2.15
Mn	6.0–6.2	Fe	balance

To protect the molten metal from atmospheric exposure, gaseous argon was used. For comparison of the wear resistance of the experimental coating with industrial counterparts, samples from the 600Cr23B7Mo7Si2W2F alloy were produced by electric arc surfacing using covered Weartrode 65T electrodes (ESAB).

As the filler (waveguide) wire, a flux-cored wire with a diameter of 2 mm was used, made with a steel strip sheath 0.5 mm thick and filled with iron powder.

The chemical composition of the surfaced coating was determined using an optical emission spectrometer Oxford Instruments PMI-MASTER PRO. Metallographic studies were carried out using optical (Carl Zeiss Axiovert 40 MAT microscope) and electron microscopy (FEI Versa 3D scanning electron-ion microscope). Metallographic sections were prepared using a grinding machine MP-1B Time Group Inc.

X-ray microanalysis of the structural components of the coating and elemental mapping of the alloying elements on the surface of microsections was carried out using an energy-dispersive *X*-ray detector (Apollo X-SDD) mounted on a Versa 3D microscope. The volumetric fractions of the structural components in the coating were determined by analyzing the elemental distribution maps on the microsection surface using the Image J software, by calculating the area occupied by each component.

X-ray phase analysis of the surfaced coatings was performed using a “Bruker D8 Advance Eco” *X*-ray diffractometer with a vertical θ-θ goniometer. The samples were scanned using copper anode radiation ($\lambda = 1.54060$ Å) under the following conditions: *X*-ray tube voltage – 40 kV; filament current – 25 mA; exposure time – 1 s; scanning step – 0.02°. Phase identification in the coatings was carried out using Diffrac.EVA software equipped with the licensed “Powder Diffraction File-2” database (The International Center for Diffraction Data).

Hardness testing of the surfaced coating was conducted by the Rockwell method (scale C) using a “TN-500 Time Group Inc.” hardness tester.

The resistance of the surfaced coating to gas-abrasive wear at normal and elevated temperatures up to 600 °C was evaluated using an express testing method described in [27]. The coating sample, a plate measuring 40×16×3.5 mm, was heated by passing an electric current through it and subjected to a stream of heated compressed air mixed with abrasive particles of quartz sand with an average size of 260 μm. Stability of the testing temperature was ensured by controlling the sample temperature with a WR5/20 thermocouple, connected to an LA-20 USB analog-to-digital converter, which displayed the readings on a computer screen using "PowerGraph" software. The test parameters were as follows: test duration – 120 s, air pressure in the system – 3 atm, attack angle of the gas-abrasive stream on the sample surface – 30°.

The wear resistance criterion was the specific wear rate (ξ, g/kg), calculated using the formula

$$\xi = \Delta m/\Delta m_a,$$

where Δm is the mass loss of the tested sample, g; m_a is the mass of abrasive used during the test, kg. The mass loss of the samples was measured with an accuracy of 0.0001 g using "Shinko Denshi VIBRA HT-124RCE" analytical scales.

The plastic deformation characteristics of the thin surface layers of worn coatings were studied using an electron-ion microscope, by preparing microsections of the surface through ion etching, with a platinum layer applied beforehand.

Technique for forming surfaced coatings

Electric arc surfacing of the coating (Fig. 1) using the experimental flux-cored wire (FCW) was performed with the "A2 Mini Master" (ESAB) welding machine, equipped with a device for introducing ultrasonic vibrations (USV) into the weld pool via a waveguide wire.

In the electro-neutral waveguide wire, which is constantly immersed in the weld pool and fed into it at a constant speed, bending vibrations with a frequency of 20.6 kHz are generated by an ultrasonic piezoelectric transducer performing longitudinal vibrations. The wire melts due to the heat generated in the welding reaction zone and also from the heat generated within the wire itself as it transmits the USV [28]. To achieve the maximum vibration amplitude at the end of the waveguide wire in the weld pool, its extension (a) must be a multiple of half the wavelength of the bending waves (λ_{ben}), and the rollers of the feeding mechanism must contact the wire at a vibration node at a distance (b) from the end of the transducer (Fig. 1). This helps reduce energy losses during the surfacing process, as the system becomes acoustically closed.

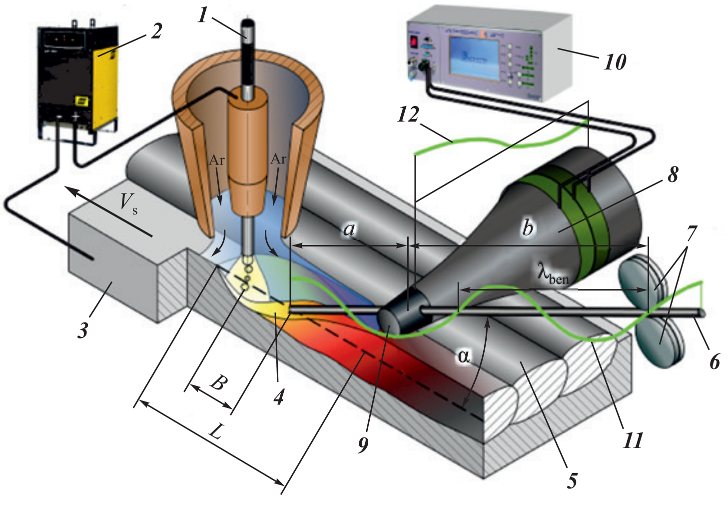

Fig. 1. Schematic diagram of the formation of the surfaced coating with the influence of USV

1 – electrode wire; ***2*** – welding power source; ***3*** – plate to be surfaced; ***4*** – weld pool; ***5*** – surfaced coating; ***6*** – waveguide wire; ***7*** – rollers of the feeding mechanism; ***8*** – ultrasonic transducer; ***9*** – vibration transmission node to the waveguide wire; ***10*** – ultrasonic generator; ***11***, ***12*** – distribution of the amplitude of bending and longitudinal vibrations, respectively; λ_{ben} – bending wavelength; B – distance between the waveguide and electrode wires; a – extension of the waveguide wire; b – distance from the point of USV input to the feeding mechanism rollers; α – inclination angle of the waveguide wire; L – length of the weld pool; V_s – surfacing speed

Рис. 1. Принципиальная схема формирования наплавленного покрытия с воздействием УЗК

1 – электродная проволока; ***2*** – сварочный источник тока; ***3*** – наплавляемая пластина; ***4*** – сварочная ванна; ***5*** – наплавленное покрытие; ***6*** – волноводная проволока; ***7*** – ролики подающего механизма; ***8*** – ультразвуковой преобразователь; ***9*** – узел передачи колебаний волноводной проволоке; ***10*** – ультразвуковой генератор; ***11***, ***12*** – распределение амплитуды изгибных и продольных колебаний соответственно; λ_{ben} – длина изгибной волны; B – расстояние между волноводной и электродной проволоками; a – вылет волноводной проволоки; b – расстояние от места подвода УЗК до роликов подающего механизма; α – угол наклона волноводной проволоки; L – длина сварочной ванны; V_s – скорость наплавки

Surfacing process parameters

Технологические параметры режима наплавки

Welding current I_{wl}, A	Arc voltage U_a, V	Surfacing speed V_s, m/h	Distance between wires B, mm	Feed rate of the wave-guide wire V_{fcw}, m/h	Angle of wave-guide wire input α, deg	USV frequency f, kHz	USV amplitude ζ, µm	Shielding gas flow (Ar), l/min
290–330	25–26	14–15	17	28–29	30	20,6	11	14–16

The power source for the ultrasonic transducer was the ultrasonic generator UZG 4-2, manufactured by Ultra-resonance (Ekaterinburg). The electrical power consumed by the transducer during surfacing was 200 W. Amplitude and frequency of acoustic vibrations were monitored using non-contact laser vibrometry with the “Polytec VibroFlex Neo” vibrometer.

Surfacing was performed on steel plates measuring 200×150×12 mm with an overlap of weld beads equal to 30 % of their width. To prevent cracks in the surfaced coating, the plates were preheated to a temperature of 300 ± 20 °C and allowed to cool slowly after surfacing. The pre-surfacing temperature was monitored using a TEKHNOAS S-20.4 infrared pyrometer.

The welding current source (direct current, electrode positive) was the thyristor rectifier ESAB LAF 1001. The technological and acoustic parameters of the surfacing process (see Table) were selected experimentally to ensure the formation of a well-shaped, defect-free surfaced coating with minimal penetration into the base metal. The main parameters of the surfacing process with and without ultrasonic vibrations did not differ.

The distance (B) between the electrode wire and the filler wire, which depends on the length of the weld pool (L), is one of the most important technological parameters of this process. It affects the quality of the surfaced coating formation, the uniform melting of the filler wire, and the stability of the ultrasonic treatment of the weld pool. When using waveguide FCW with a diameter of 2 mm and a feed rate of 28–29 m/h into the weld pool, the distance B should be within 0.37–0.57 of the pool length L [28]. Introducing the wire into the pool beyond the upper limit of this range results in defects in the surfaced coating, while introducing it too close to the electric arc makes ultrasonic treatment impossible, as the waveguide wire melts above the weld pool.

Introducing the wire into the weld pool at a 30° angle to the surfaced surface ensures complete melting of the wire over a wide range of feed speeds.

Results and discussion

It was experimentally established that the influence of USV during the surfacing of the 280Cr14Mn6Ni6Mo3Ti2Nb2 alloy coating leads to significant structural changes (Fig. 2). The microstructure of the coating formed without acoustic treatment of the crystallizing alloy is hypereutectic, with large primary carbides of needle-like and plate-like shapes (Fig. 2, *a*, *b*). Combined *X*-ray microanalysis and *X*-ray phase analysis of the coatings showed that the solid solution of the carbide eutectic consists of alloyed γ-Fe, and the majority of the strengthening phase is represented by Me_7C_3 and Me_3C_2 carbides, where Me is chromium, iron, manganese, and molybdenum (Fig. 3). The structure also contains relatively uniformly distributed fine solid phases, represented by complex carbides $(Ti,Nb,Mo)_xC_y$ and monocarbides Mo_2C with an average particle size of 3.5 µm and 1.6 µm, respectively. No defects such as cracks, delamination from the base metal, pores, etc., were detected in the surfaced coating.

The influence of high-frequency acoustic vibrations leads to the disappearance of large primary Me_xC_y carbide crystals in the coating structure and some dispersion of the austenite-carbide eutectic (Fig. 2, *c*, *d*). This is accompanied by the appearance of characteristic “rosettes” consisting of plate-like carbides separated by layers of solid solution. In addition to the $(Ti,Nb,Mo)_xC_y$ and Mo_2C carbides, a small amount of $(Ti,Mo)_xC_y$ and TiC carbides also appears in the alloy.

It has been established that high-frequency vibrations of the filler wire lead to its additional heating. This helps to reduce the “chilling” effect of the weld pool, which manifests in classical surfacing processes with “cold” filler by reducing its length. In the studied process, with a wire feed rate of 28–29 m/h, the pool length decreases by no more than 4 %. At the same time, the proportion of filler metal in the surfaced coating is very small, amounting to 1.0–1.2 wt. %. Thus, the changes in the structure of the studied alloy are related specifically to the influence of acoustic vibrations on the crystallization process, rather than to supercooling of the weld pool or changes in its chemical composition.

The mechanism of microstructure transformation in the surfaced coating under the influence of USV is as follows. In the absence of acoustic vibrations, large primary Me_xC_y carbides crystallize from the weld pool,

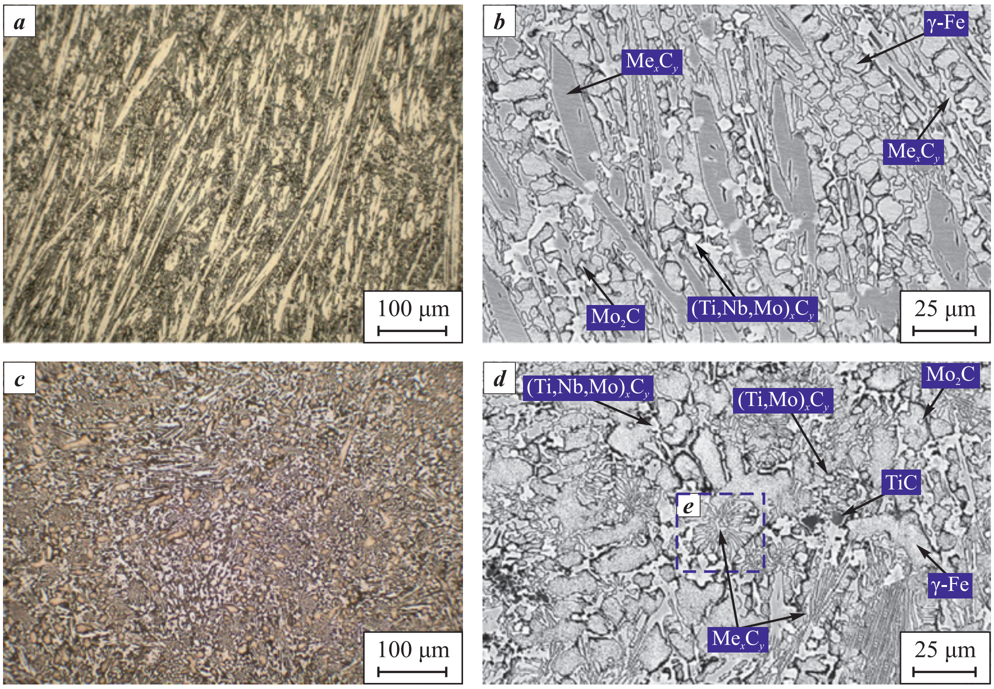

Fig. 2. Microstructure of the coating surfaced without USV (***a***, ***b***) and with USV (***c***, ***d***):
a, ***c*** – optical image; ***b***, ***d*** – electron image; ***e*** – "rosette" of Me_xC_y carbide

Рис. 2. Микроструктура покрытия, наплавленного без УЗК (***a***, ***b***) и с воздействием УЗК (***c***, ***d***)
a, ***c*** – оптическое изображение; ***b***, ***d*** – электронное изображение; ***e*** – «розетка» карбида Me_xC_y

with an austenite-carbide eutectic forming between them. When high-frequency acoustic vibrations are induced in the melt, the crystallization process occurs under the mechanical action of shock waves generated by cavitation in the melt, which destroy the growing carbide crystals. The resulting carbide fragments are carried by acoustic flows along the crystallization front and act as additional nucleation centers for further crystallization. The formation of strengthening phases on these fragments in the melt may be facilitated by reduced surface tension at the interphase boundaries under the influence of USV.

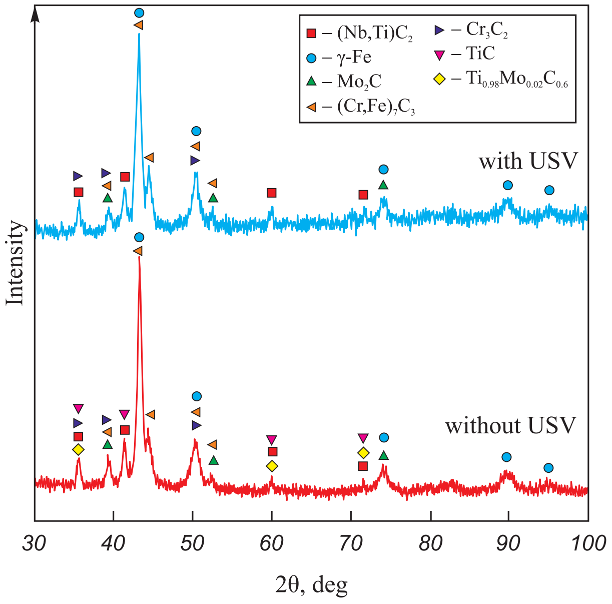

Fig. 3. Results of *X*-ray phase analysis of coatings surfaced with and without USV

Рис. 3. Результаты рентгенофазового анализа покрытий, наплавленных с воздействием УЗК и без них

The change in the crystallization kinetics of the surfaced alloy due to acoustic treatment leads to a 25 % increase in the volume fraction of austenite (Fig. 4), while the content of Me_xC_y carbides decreases proportionally, and the content of fine carbides $(Ti,Nb,Mo)_xC_y$ and Mo_2C changes insignificantly.

The change in the volume fraction of structural components in the surfaced alloy is accompanied by a redistribution of alloying elements between them (Fig. 5), which affects their mechanical properties. It was found that the molybdenum content in austenite decreases by a factor of two, while the chromium content increases by 20 %, which may improve the heat resistance of the alloy matrix. This is accompanied by a proportional decrease in the chromium content in Me_xC_y carbides and an increase in the content of iron, manganese, and molybdenum, which may reduce their microhardness. The molybdenum content in $(Ti,Nb,Mo)_xC_y$ carbides decreases almost fivefold, while the Ti/Nb ratio

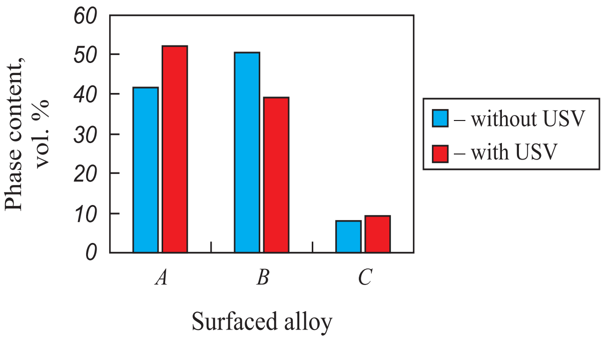

Fig. 4. Volume fraction of structural components in the surfaced alloy with and without USV

A – austenite, *B* – Me$_x$C$_y$, carbides, *C* – (Ti,Nb,Mo)$_x$C$_y$, (Ti, Mo)$_x$C$_y$, Mo$_2$C, and TiC carbides

Рис. 4. Количественное распределение фаз в структуре покрытия, наплавленного с воздействием УЗК и без него

A – аустенит, *B* – карбиды типа Me$_x$C$_y$, *C* – карбиды типа (Ti,Nb,Mo)$_x$C$_y$, (Ti, Mo)$_x$C$_y$, Mo$_2$C и TiC

(in at. %) increases from 1.05 to 1.2, which, according to [29], may improve the microhardness of these carbides.

It has been established that the structural changes in the surfaced coating caused by USV do not affect its hardness, but they result in an average 18 % increase in its resistance to high-temperature gas-abrasive wear (Fig. 6). The wear resistance of the experimental alloy 280Cr14Mn6Ni6Mo3Ti2Nb2, modified by USV, exceeds that of the more heavily alloyed industrial counterpart 600Cr23B7Mo7Si2W2F (ESAB) by 26 %. The high wear resistance of the developed coating is due to the formation of a composite structure, combining a strong and ductile nickel-manganese austenitic matrix, alloyed with chromium and molybdenum, and a strengthening phase in the form of plate-like Me$_x$C$_y$ carbides and ultra-hard fine carbides (Ti,Nb,Mo)$_x$C$_y$ and Mo$_2$C.

It was revealed (Fig. 7) that, as a result of the high-temperature gas-abrasive flow, a deformed layer forms on the surface of the coatings, which can be identified in cross-sections of worn samples obtained by ion etching. Under the impact of abrasive particles, partial destruction of large plate-like Me$_x$C$_y$ carbides occurs, accompanied by the formation of cracks that open in the direction of the gas-abrasive flow (Fig. 7, *a*–*c*). Smaller and more durable (Ti,Nb,Mo)$_x$C$_y$ carbides, with their compact shape, shift together with the matrix material without fracturing, limiting its plastic deformation and reducing the coating's wear rate. The primary wear mechanism appears to be the chipping of relatively large Me$_x$C$_y$ carbide fragments followed by the shearing of micro-volumes of austenite.

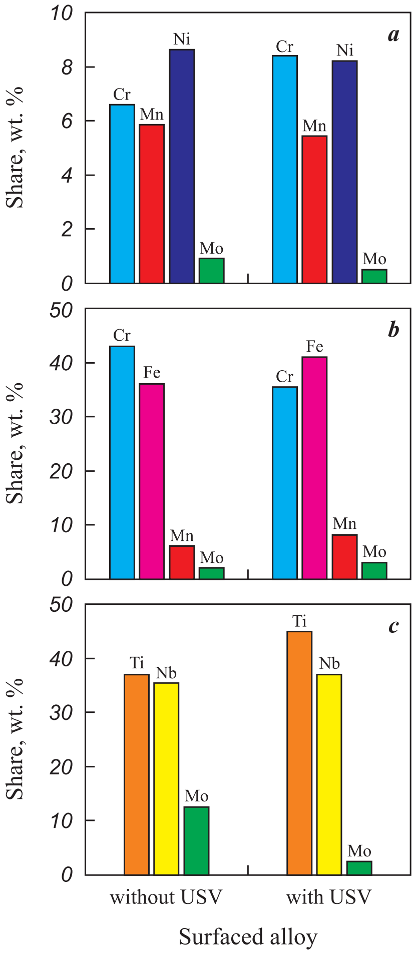

Fig. 5. Chemical composition of austenite (***a***), Me$_x$C$_y$ carbides (***b***), and (Ti,Nb,Mo)$_x$C$_y$ (***c***) in the coating surfaced with and without USV

Рис. 5. Химический состав аустенита (***а***), карбидов Me$_x$C$_y$ (***b***) и (Ti,Nb,Mo)$_x$C$_y$ (***c***) в покрытии, наплавленном с УЗК и без них

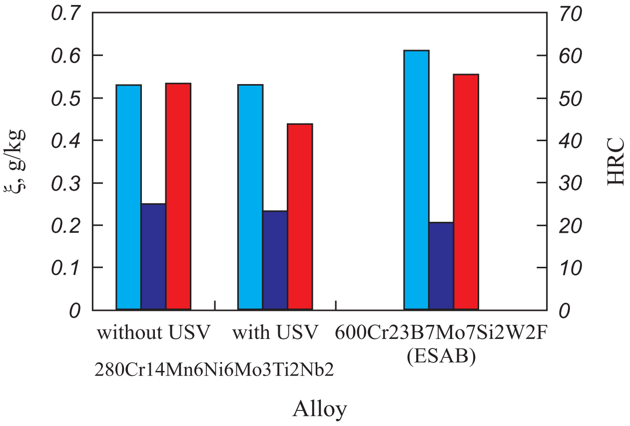

Fig. 6. Hardness (HRC) and specific wear (ξ) of the experimental and industrial alloys

🟦 – HRC hardness; ■ – ξ at 20 °C; 🟥 – ξ at 600 °C

Рис. 6. Твердость (HRC) и удельный износ (ξ) экспериментального и промышленного сплавов

🟦 – твердость HRC; ■ – ξ при 20 °C; 🟥 – ξ при 600 °C

The study of the cross-section of the worn coating surfaced with USV showed (Fig. 7, *d*) that the processes of intense plastic deformation in the alloy extend to a depth of about 10 µm. Under the impact of abrasive particles, thin Me_xC_y carbide plates crack, and the fragments shift in the direction of impact. At the same time, the solid solution layers dampen shear deformations, and the plastic flow of the austenitic matrix forms a metallic binder around the resulting carbide fragments, reducing the likelihood of their chipping. This is likely also facilitated by the increase in the austenite volume in the structure of the modified coating, as well as the enhancement of its heat resistance due to the increased chromium content.

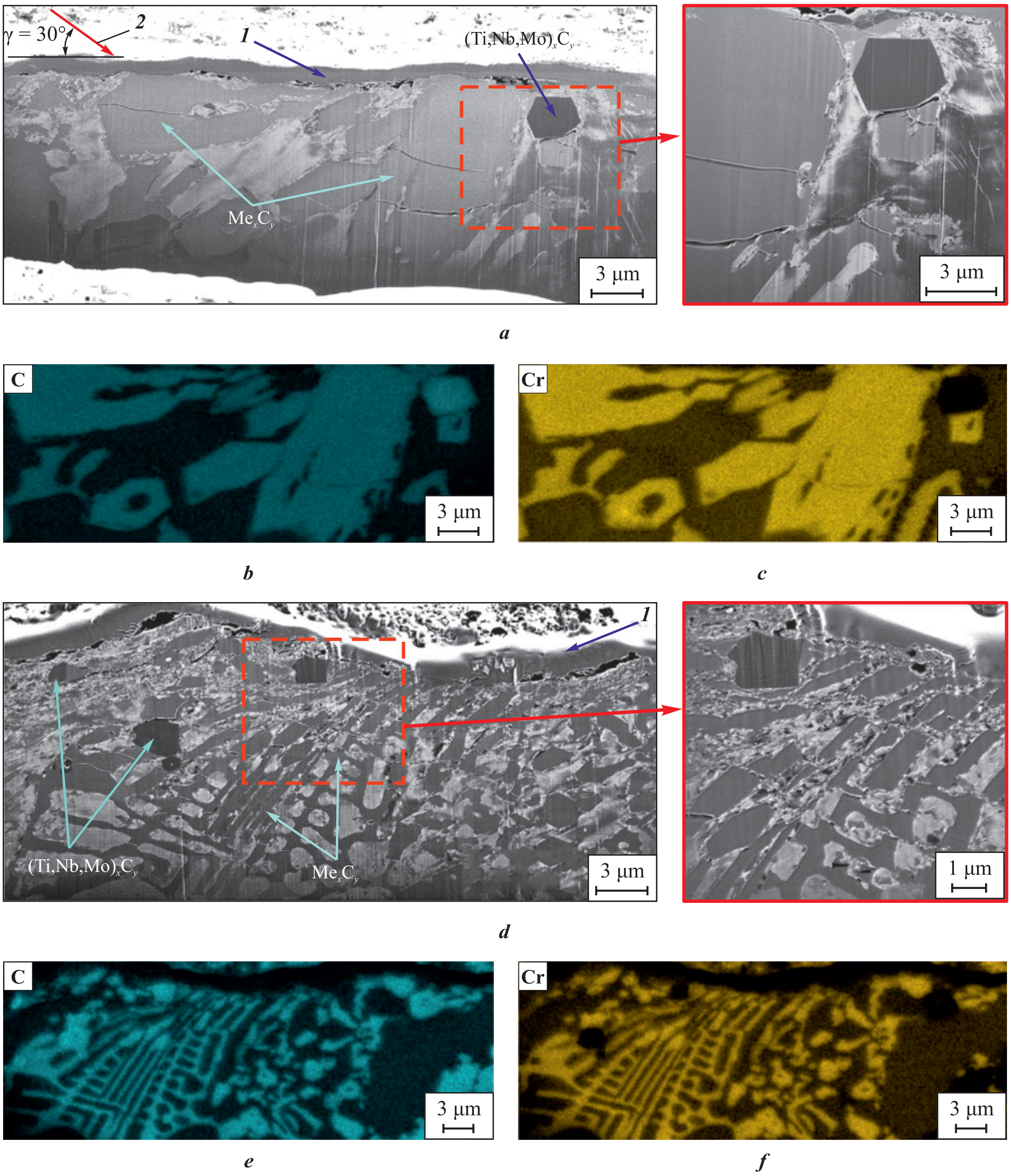

a

b ***c***

d

e ***f***

Fig. 7. Cross sections of the surface layer of coatings surfaced without USV (***a***) and with USV (***d***), after gas-abrasive wear testing at 600 °C; carbon (***b***, ***e***) and chromium (***c***, ***f***) distribution maps across the cross-sections

1 – platinum layer; ***2*** – direction of the gas-abrasive flow

Рис. 7. Сечения поверхностного слоя покрытий, наплавленных без воздействия УЗК (***a***) и с УЗК (***d***), после испытаний на газоабразивное изнашивание при температуре 600 °C; карты распределения углерода (***b***, ***e***) и хрома (***c***, ***f***) по сечению покрытий

1 – слой платины; ***2*** – направление газоабразивного потока

Conclusions

1. It has been established that ultrasonic treatment of the weld pool during electric arc surfacing affects the crystallization processes of the wear-resistant coating, contributing to the reduction in volume fraction and refinement of primary and eutectic Me_xC_y carbides, increasing the volume of the austenitic matrix by 25 %, and leading to the appearance of $(Ti,Mo)_xC_y$ and TiC carbides in the structure. This is accompanied by the redistribution of alloying elements between the strengthening phases and the austenite, which affects their mechanical properties. The chromium content in austenite increases by 20 %, while it decreases in Me_xC_y carbides. Meanwhile, the concentrations of molybdenum and manganese in austenite decrease, while they increase in Me_xC_y carbides. Additionally, the titanium content increases in $(Ti,Nb,Mo)_xC_y$ carbides, and the molybdenum content decreases significantly.

2. The structural changes in the coating caused by USV lead to an 18 % increase in its resistance to gas-abrasive wear at 600 °C, exceeding the performance of international industrial counterparts. This is explained by the formation of a fine lamellar carbide eutectic reinforced with ultra-hard $(Ti,Nb,Mo)_xC_y$ carbides, which limits the intense plastic deformation of the alloy during wear, confining it to a depth of 10 μm. The negative effect of Me_xC_y carbide cracking under the impact of abrasive particles is mitigated by the increased volume and heat resistance of the austenite, whose plastic flow forms a metallic binder around the carbide fragments, reducing the likelihood of their chipping.

References / Список литературы

1. Sokolov G.N., Lysak V.I. Surfacing of wear-resistant alloys on press dies and tools for hot deformation of steels. Volgograd: Politekhnik, 2005. 284 p. (In Russ.).

   Соколов Г.Н., Лысак В.И. Наплавка износостойких сплавов на прессовые штампы и инструмент для горячего деформирования сталей. Волгоград: Политехник, 2005. 284 с.
2. Pawar S., Jha A.K., Mukhopadhyay G. Effect of different carbides on the wear resistance of Fe-based hardfacing alloys. *International Journal of Refractory Metals and Hard Materials*. 2019;78:288–295. https://doi.org/10.1016/j.ijrmhm.2018.10.014
3. Jindal C., Sidhu B.S., Kumar P., Sidhu H.S. Performance of hardfaced/heat treated materials under solid particle erosion: A systematic literature review. *Materials Today: Proceedings*. 2022;50(5):629–639. https://doi.org/10.1016/j.matpr.2021.03.441
4. Kleis I., Kulu P. Solid particle erosion: occurrence, prediction and control. London: Springer, 2008. 206 p. https://doi.org/10.1016/10.1007/978-1-84800-029-2
5. Fortini A., Suman A., Zanini N. An experimental and numerical study of the solid particle erosion damage in an industrial cement large-sized fan. *Engineering Failure Analysis*. 2023;146:107058. https://doi.org/10.1016/j.engfailanal.2023.107058
6. Roy M. Elevated temperature erosive wear of metallic materials. *Journal of Physics D: Applied Physics*. 2006;39(6): 101–124. https://doi.org/10.1088/0022-3727/39/6/R01
7. Ricardo G.A.N., Sommerfeld M. Comprehensive Euler/Lagrange modelling including particle erosion for confined gas-solid flows. *Particuology*. 2024; 84:209–235. https://doi.org/10.1016/j.partic.2023.06.010
8. Zhou L., Li T., Liu Z., Ma H., Xu C., Dong Y., Zhao Y. An impact energy erosion model with an energy allocation rule for the discrete element method. *Wear*. 2024;540–541: 205233. https://doi.org/10.1016/j.wear.2023.205233
9. Tarodiya R., Levy A. Surface erosion due to particle-surface interactions – A review. *Powder Technology*. 2021;387:527–559. https://doi.org/10.1016/j.powtec.2021.04.055
10. Krupicz B., Tarasiuk W., Barsukov V.G., Sviridenok A.I. Experimental evaluation of the influence of mechanical properties of contacting materials on gas abrasive wear of steels in sandblasting systems. *Journal of Friction and Wear*. 2020; 41(1):5–11. https://doi.org/10.3103/S1068366620010110

    Крупич Б., Тарасюк В., Барсуков В.Г., Свириденок А.И. Экспериментальная оценка влияния механических свойств контактирующих материалов на газоабразивное изнашивание сталей в системах пескоструйного типа. *Трение и износ*. 2020;41(1):5–11.
11. Varga M. High temperature abrasive wear of metallic materials. *Wear*. 2017; 376–377(A):443–451. https://doi.org/10.1016/j.wear.2016.12.042
12. Priyatkin D.V., Artem'ev A.A., Lysak V.I., Loiko P.V. Analysis of hardfacing alloys for work in conditions of gas-abrasive wear at elevated temperatures. *Izvestiya Volgogradskogo gosudarstvennogo tekhnicheskogo universiteta*. 2020; 10(245):49–55. (In Russ.). https://doi.org/10.35211/1990-5297-2020-10-245-49-55

    Прияткин Д.В., Артемьев А.А., Лысак В.И., Лойко П.В. Анализ наплавочных сплавов для работы в условиях газоабразивного изнашивания при повышенных температурах. *Известия Волгоградского государственного технического университета*. 2020;10(245):49–55. https://doi.org/10.35211/1990-5297-2020-10-245-49-55
13. Qin Z., He D., Ma L., He C., Wu X., Wang, G. Influence of Ni additions on microstructure, non-magnetic properties, and wear resistance of Fe–Mn–Cr alloy deposited by metal-cored arc welding. *Welding in the World*. 2024; 68:699–714. https://doi.org/10.1007/s40194-024-01694-9
14. Chernyshov G.G., Kobernik N.V., Orlik A.G., Chernyshova T.A. The influence of the structure of the deposited coatings on the resistance to abrasive wear. *Fizika i khimiya obrabotki materialov*. 2011;(5):44–50. (In Russ.).

    Чернышов Г.Г., Коберник Н.В., Орлик А.Г., Чернышова Т.А. Влияние структуры наплавленных покрытий на стойкость к абразивному износу. *Физика и химия обработки материалов*. 2011;(5):44–50.

15. Eremin E.N., Losev A.S., Borodikhin S.A., Matalasova A.E., Ponomarev I.A. Powder wire for surfacing corrosion-resistant and wear-resistant steel. *Vestnik mashinostroeniya*. 2018;(7):66–68. (In Russ.).

Еремин Е.Н., Лосев А.С., Бородихин С.А., Маталасова А.Е., Пономарев И.А. Порошковая проволока для наплавки коррозионно-стойкой и износостойкой стали. *Вестник машиностроения*. 2018;(7):66–68.

16. Saraev Yu.N., Lebedev V.A., Novikov S.V. Analysis of existing methods for controlling the structure of the weld metal. *Russian Internet Journal of Industrial Engineering*. 2016;4(1):16–26. (In Russ.).

Сараев Ю.Н., Лебедев В.А., Новиков С.В. Анализ существующих методов управления структурой металла сварного шва. *Машиностроение: сетевой электронный научный журнал*. 2016;4(1):16–26.

17. Fan Z., Bai K., Chen C. The application of ultrasound in Joining: Principles, processes and properties. *Journal of Manufacturing Processes*. 2023;101:269–299.
https://doi.org/10.1016/j.jmapro.2023.05.094

18. Mohsan A.U.H., Zhang M., Wang D., Zhao S., Wang Y., Chen C., Zhang J. State-of-the-art review on the Ultrasonic Vibration Assisted Laser Cladding (UVALC). *Journal of Manufacturing Processes*. 2023;107:422–446.
https://doi.org/10.1016/j.jmapro.2023.10.066

19. Zhang K., Gao G., Zhao C., Wang Y., Wang Y., Li, J. Review of the design of power ultrasonic generator for piezoelectric transducer. *Ultrasonics Sonochemistry*. 2023;96:106438.
https://doi.org/10.1016/j.ultsonch.2023.106438

20. Chang L., Yanpeng Y., Zhaotai L., Xin H., Tenghui J. Differential analysis of the influence mechanism of ultrasonic vibrations on laser cladding. *CIRP Journal of Manufacturing Science and Technology*. 2022;38:16–37.
https://doi.org/10.1016/j.cirpj.2022.03.009

21. Kudina A.V., Kurash V.V., Redin I.V., Khrolenok V.V. Obtaining wear-resistant metal coatings by electric arc surfacing with a melting electrode when exposed to ultrasound. *Agropanorama*. 2013;3(97):34–38. (In Russ.).

Кудина А.В., Кураш В.В., Редин И.В., Хроленок В.В. Получение износостойких металлопокрытий электродуговой наплавкой плавящимся электродом при воздействии на него ультразвуком. *Агропанорама*. 2013;3(97):34–38.

22. Minin S.I., Trofimov A.I., Trofimov M.A. The technology of thermal welding of the circulation piping of NPPS containing the influence of ultrasound. *Izvestiya vuzov. Yadernaya energetika*. 2016;(4):5–11. (In Russ.).
https://doi.org/10.26583/npe.2016.4.01

Минин С.И., Трофимов А.И., Трофимов М.А. Технология термической сварки циркуляционных трубопроводов АЭС с воздействием ультразвука. *Известия вузов. Ядерная энергетика*. 2016;(4):5–11.
https://doi.org/10.26583/npe.2016.4.01

23. Priyatkin D.V., Artem’ev A.A., Sokolov G.N., Lysak V.I., Odnogulov R.M., Loiko P.V. Analysis of the methods of introducing the ultrasonic vibrations in the weld pool in the process of arc surface and development devices for its implementation. *Izvestiya Volgogradskogo gosudarstvennogo tekhnicheskogo universiteta*. 2019;4(227):68–75. (In Russ.).

Прияткин Д.В., Артемьев А.А., Соколов Г.Н., Лысак В.И., Одногулов Р.М., Лойко П.В. Анализ способов введения в сварочную ванну ультразвуковых колебаний в процессе дуговой наплавки и разработка устройства для его осуществления. *Известия Волгоградского государственного технического университета*. 2019;4(227):68–75.

24. Wang Y., Yu C., Lu H., Chen J. Research status and future perspectives on ultrasonic arc welding technique. *Journal of Manufacturing Processes*. 2020;58:936–954.
https://doi.org/10.1016/j.jmapro.2020.09.005

25. Fattahi M., Ghaheri A., Arabian N., Amirkhanlu F., Moayedi H. Applying the ultrasonic vibration during TIG welding as a promising approach for the development of nanoparticle dispersion strengthened aluminum weldments. *Journal of Materials Processing Technology*. 2020;282:116672.
https://doi.org/10.1016/j.jmatprotec.2020.116672

26. Priyatkin D.V., Artemyev A.A., Lysak V.I. Investigation of the surfaced metal of the Fe–Cr–Ni–Mn–Mo–Ti–Nb–C system for operation under high-temperature gas-abrasive wear. *Voprosy Materialovedeniya*. 2022;3(111):17–28. (In Russ.).
https://doi.org/10.22349/1994-6716-2022-111-3-17-28

Прияткин Д.В., Артемьев А.А., Лысак В.И. Исследование наплавленного металла системы Fe–Cr–Ni–Mn–Mo–Ti–Nb–C для работы в условиях высокотемпературного газоабразивного изнашивания. *Вопросы материаловедения*. 2022;3(111):17–28.
https://doi.org/10.22349/1994-6716-2022-111-3-17-28

27. Artem’ev A.A., Sokolov G.N., Zorin I.V., Lysak V.I., Rykov M.A., Krutenko A.V., Shnipko M.V. Method of tested weld metal for gas-abrasive wearing. *Izvestiya Volgogradskogo gosudarstvennogo tekhnicheskogo universiteta*. 2018;3(213):112–116. (In Russ.).

Артемьев А.А., Соколов Г.Н., Зорин И.В., Лысак В.И., Рыков М.А., Крутенко А.В., Шнипко М.В. Методика испытаний наплавленного металла на газоабразивное изнашивание. *Известия Волгоградского государственного технического университета*. 2018;3(213):112–116.

28. Priyatkin D.V., Artemyev A.A., Lysak V.I., Tsyganok S.N. Electric arc cladding of wear-resistant alloys with ultrasonic action on the weld pool. *Svarka i diagnostika*. 2023;(5):20–26. (In Russ.).

Прияткин Д.В., Артемьев А.А., Лысак В.И., Цыганок С.Н. Электродуговая наплавка износостойких сплавов с ультразвуковым воздействием на сварочную ванну. *Сварка и диагностика*. 2023;(5):20–26.

29. Sun S., Fu H., Ping X., Guo X., Lin J., Lei Y., Zhou J. Formation mechanism and mechanical properties of titanium-doped NbC reinforced Ni-based composite coatings. *Applied Surface Science*. 2019;476:914–927.
https://doi.org/10.1016/j.apsusc.2019.01.171

Information about the Authors

Dmitriy V. Priyatkin – Cand. Sci. (Eng.), Senior Lecturer, Department of Equipment and Welding Production, Volgograd State Technical University (VSTU)
ORCID: 0000-0003-0001-8019
E-mail: priyatkin.dv@mail.ru

Aleksandr A. Artem'ev – Cand. Sci. (Eng.), Associate Professor, Department of Equipment and Welding Production, VSTU
ORCID: 0000-0001-6616-0427
E-mail: artspace7@ya.ru

Vladimir I. Lysak – Dr. Sci. (Eng.), Professor, Academician of the Russian Academy of Sciences, Head of the Department of Equipment and Welding Production, Scientific Director, VSTU
ORCID: 0000-0003-3066-058X
E-mail: lysak@vstu.ru

Сведения об авторах

Дмитрий Вячеславович Прияткин – к.т.н., ст. преподаватель кафедры «Оборудование и технология сварочного производства» Волгоградского государственного технического университета (ВолгГТУ)
ORCID: 0000-0003-0001-8019
E-mail: priyatkin.dv@mail.ru

Александр Алексеевич Артемьев – к.т.н., доцент кафедры «Оборудование и технология сварочного производства» ВолгГТУ
ORCID: 0000-0001-6616-0427
E-mail: artspace7@ya.ru

Владимир Ильич Лысак – д.т.н., профессор, академик РАН, заведующий кафедрой «Оборудование и технология сварочного производства», научный руководитель ВолгГТУ
ORCID: 0000-0003-3066-058X
E-mail: lysak@vstu.ru

Contribution of the Authors

D. V. Priyatkin – esponsible for the production of powder wires for surfacing, conducting experiments on electric arc surfacing of coatings with ultrasonic vibrations, durometric testing, and metallographic studies.
A. A. Artem'ev – conducted tests on samples for gas-abrasive wear, studied the mechanisms of coating wear, and analyzed changes in the chemical and structural-phase composition of coatings under the influence of ultrasonic vibrations.

V. I. Lysak – defined the goals and objectives of the research, analyzed the results obtained, and provided scientific editing of the article.

Вклад авторов

Д. В. Прияткин – изготовление порошковых проволок для наплавки, эксперименты по электродуговой наплавке покрытий с воздействием ультразвуковых колебаний, дюрометрические испытания, металлографические исследования.
А. А. Артемьев – проведение испытаний образцов на газоабразивное изнашивание, изучение механизмов изнашивания покрытий, анализ изменений химического и структурно-фазового состава покрытий под воздействием ультразвуковых колебаний.
В. И. Лысак – определение целей и задач исследования, анализ полученных результатов, научное редактирование статьи.

Received 31.05.2024
Revised 01.08.2024
Accepted 12.08.2024

Статья поступила 31.05.2024 г.
Доработана 01.08.2024 г.
Принята к публикации 12.08.2024 г.

UDC 621.762

https://doi.org/10.17073/1997-308X-2024-5-55-65

Research article
Научная статья

Investigation of the properties of WC–5TiC–10Co cutting inserts produced using a 3D-printed plastic mold

M. I. Dvornik, E. A. Mikhailenko, A. A. Burkov, E. V. Chernyakov

Institute of Materials Science of the Khabarovsk Federal Research Center
of the Far Eastern Branch of the Russian Academy of Sciences
153 Tikhookeanskaya Str., Khabarovsk 680042, Russia

mea80@list.ru

Abstract. Cutting inserts made from the WC–5TiC–10Co hard alloy were produced by sintering blanks that were pressed in a plastic mold made from polylactide on a 3D printer using a layer-by-layer deposition method. The effect of pressing pressure and plasticizer (rubber) content in the powder mixture on the density of the blanks was studied. As the pressing pressure increased from 50 to 200 MPa, the density of the blanks rose by only 2–6 %. When the plasticizer concentration in the powder mixture increased from 1 to 6 %, the blank density increased by 28–32 %. It was found that the density values of the cutting insert blanks obtained in a plastic mold differed only slightly from those of standard blanks produced in a steel mold. After sintering in a vacuum furnace at 1450 °C, the density, carbon content, porosity, microstructure, surface roughness, hardness, and fracture toughness of all the sintered cutting inserts, standard samples, and the commercial equivalent were investigated. It was shown that the formation of free carbon as a result of rubber decomposition leads to a decrease in the density of the finished products, and therefore, their hardness. The relative density (98.7 %) of the cutting insert produced in the plastic mold at a pressing pressure of 50 MPa from powder containing 1 % rubber exceeded the density of the commercial cutting insert (98.5 %). The obtained cutting insert demonstrated high hardness (1400 HV) and fracture toughness (13.5 MPa·m$^{1/2}$). The cutting insert made from the WC–5TiC–10Co alloy is not inferior to the commercial T5K10 hard alloy insert in terms of flank wear rate during turning of a steel workpiece.

Keywords: cutting insert, pressing, hard alloy, 3D printing, mold, polylactide

Acknowledgements: This research was supported by the Russian Science Foundation grant No. 23-29-00063.

For citation: Dvornik M.I., Mikhailenko E.A., Burkov A.A., Chernyakov E.V. Investigation of the properties of WC–5TiC–10Co cutting inserts produced using a 3D-printed plastic mold. *Powder Metallurgy and Functional Coatings*. 2024;18(5):55–65. https://doi.org/10.17073/1997-308X-2024-5-55-65

Исследование характеристик режущих пластин из твердого сплава WC–5TiC–10Co, полученных с применением пластиковой формы, изготовленной методом 3D-печати

М. И. Дворник, Е. А. Михайленко, А. А. Бурков, Е. В. Черняков

Институт материаловедения Хабаровского федерального исследовательского центра
Дальневосточного отделения РАН
Россия, 680042, г. Хабаровск, ул. Тихоокеанская, 153

mea80@list.ru

Аннотация. Были изготовлены режущие пластины из твердого сплава WC–5TiC–10Co спеканием заготовок, спрессованных в пластиковой форме, полученной из полилактида на 3D-принтере методом послойной наплавки. Исследовано влияние давления прессования и содержания пластификатора (каучука) в порошковой смеси на плотность заготовок. С повышением давления прессования от 50 до 200 МПа плотность заготовок возрастает только на 2–6 %. При увеличении концентрации пластификатора в порошковой смеси с 1 до 6 % происходит повышение плотности заготовок на 28–32 %. Установлено, что значения плотности заготовок режущих пластин, получаемых в пластиковой пресс-форме, незначительно отличаются от плотности стандартных заготовок, получаемых в стальной пресс-форме. После спекания в вакуумной печи при температуре 1450 °C были исследованы плотность, содержание углерода, пористость, микроструктура, шероховатость поверхности, твердость и вязкость разрушения всех спеченных режущих пластин, стандартных образцов и коммерческого аналога. Показано, что формирование свободного углерода в результате разложения каучука приводит к снижению плотности готовых изделий, а следовательно, и их твердости. Относительная плотность (98,7 %) режущей пластины, полученной в пластиковой пресс-форме при давлении прессования 50 МПа из порошка, содержащего 1 % каучука, превышает плотность коммерческой режущей пластины (98,5 %). Полученная режущая пластина имеет высокие твердость (1400 HV) и вязкость разрушения (13,5 МПа·м$^{1/2}$). Изготовленная режущая пластина из сплава WC–5TiC–10Co не уступает по скорости износа по задней грани коммерческой пластине из твердого сплава Т5К10 при точении стальной заготовки.

Ключевые слова: режущая пластина, прессование, твердый сплав, 3D-печать, пресс-форма, полилактид

Благодарности: Исследование проведено при поддержке гранта РНФ № 23-29-00063.

Для цитирования: Дворник М.И., Михайленко Е.А., Бурков А.А., Черняков Е.В. Исследование характеристик режущих пластин из твердого сплава WC–5TiC–10Co, полученных с применением пластиковой формы, изготовленной методом 3D-печати. *Известия вузов. Порошковая металлургия и функциональные покрытия*. 2024;18(5):55–65. https://doi.org/10.17073/1997-308X-2024-5-55-65

Introduction

Hard alloys based on WC and TiC are widely used in metalworking [1]. Industrial production of hard alloy products is based on sintering blanks obtained by cold pressing in steel or hard alloy molds. These molds ensure the necessary density and high precision, possess high productivity, and have a long service life, but are limited in terms of product shape and require significant costs for their manufacturing. In recent years, additive technologies have been employed to produce complex-shaped hard alloy products from structural materials [2–4]. However, these methods face certain challenges. For example, producing high-density hard alloy products using selective laser sintering is complicated by changes in chemical composition [4–15], while blanks for sintering obtained by binder jetting (BJ) [4; 16–23], fused filament fabrication (FFF) [24], and gel-based 3D printing (3DGP) [25; 26] have reduced density due to the lack of pressure.

An alternative method involves using plastic molds manufactured on a 3D printer for slip casting of hard alloy and ceramic blanks, which are later sintered using conventional methods [27; 28]. When using these methods, the volumetric fraction of the plasticizer must be significantly increased (over 50 vol. %). Removing the plasticizer from the blanks creates pores, reducing the density of the products made using these methods. Studies have shown that WC–15Co hard alloy blanks can be produced by pressing at pressures up to 120 MPa in plastic molds made by layer-by-layer deposition [29]. The resulting alloy samples match the density and characteristics of those obtained by pressing in conventional steel molds. Expanding the applicability of this method requires broadening the range of materials used and increasing pressing conditions.

The goal of this study was to investigate the effect of plasticizer concentration and pressing pressure (up to 200 MPa) in plastic molds on the density, microstructure, hardness, and fracture toughness of cutting inserts made from the WC–5TiC–10Co hard alloy. The wear resistance of the obtained samples was also compared with a commercial equivalent.

Research methodology

To assess the effect of plasticizer concentration and pressing pressure on the properties of the experimental samples, 200 g of WC–5TiC–10Co powder was prepared by mixing powders from the Kirovgrad Hard Alloy Plant: WC (73.3 %, WC3), (Ti,W)C (16.7 %, TWC3), and Co (10 %, PK1U)) in a PM-400 planetary mill (Retsch, Germany) for 120 min at 350 rpm. The ball-to-powder mass ratio was 3:1. After mixing, the powder was divided into four equal parts, each of which was supplemented with 1, 2, 4, and 6 wt. % rubber as a solution. The resulting mixtures were pressed after drying and granulation.

The plastic mold for pressing the SNUM-120408 cutting insert blanks (Fig. 1, *c*) was made of polylactide (PLA, produced by Bestfilament, Tomsk) using layer-by-layer deposition technology on a Flash Forge Dreamer 3D printer (China). The filling was 100 %, with a first layer thickness of 0.27 mm and subsequent layers of 0.1 mm. The printing temperature was 200 °C. The compressive strength, Young's modulus, and Poisson's ratio of the plastic, according to test results, were 70 MPa, 1.54 GPa, and 0.38, respectively [29; 30]. A steel shell, steel rod, and steel pusher were used to ensure high pressing pressures (up to 200 MPa) in the plastic mold (Fig. 1, *b*, *c*).

From each batch of powder, four samples weighing 8 g each were pressed in plastic molds at pressures of 50, 100, 150, and 200 MPa, and one rectangular blank measuring 24×8×8 mm was pressed in a steel mold at 200 MPa for comparison. A total of 20 different samples were obtained (Fig. 1, *e*). After pressing, the density of the obtained blanks was measured. The blanks were sintered after plasticizer removal (Fig. 1, *d*) at a maximum temperature of 1450 °C. After

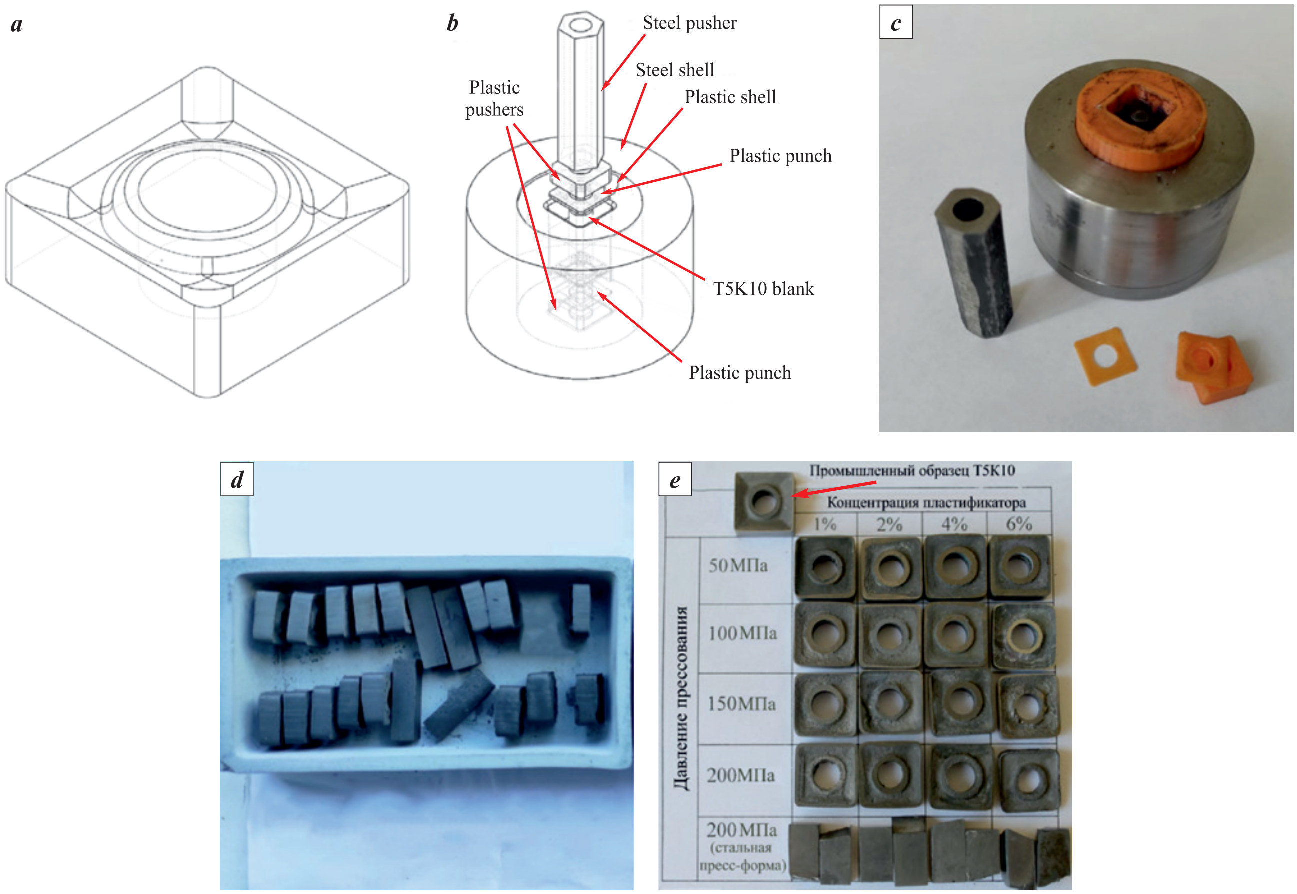

Fig. 1. 3D model of the cutter (***a***), mold diagram (***b***), mold (***c***), blanks after pressing (***d***), sintered samples and commercial T5K10 cutting insert (***e***)

Рис. 1. 3D-модель резца (***a***), схема пресс-формы (***b***), пресс-форма (***c***), заготовки после прессования (***d***), спеченные образцы и коммерческая режущая пластина T5K10 (***e***) sintering, the samples were ground and polished for microstructure analysis. Hardness, fracture toughness, and strength (only for rectangular samples) were measured, and wear resistance tests were conducted during the turning of steel 45 using the cutting insert produced at a pressing pressure of 50 MPa from a powder mixture containing 1 % rubber, compared with the commercial SNUM-120408 insert made from the T5K10 alloy by KZTS.

Pressing and testing of the punches and sintered samples were conducted on an IP-250M test press (ZIPO LLC, Armavir) at a loading rate of 0.5 kN/s. The pressing force required to achieve pressures of 50, 100, 150, and 200 MPa was calculated based on the punch area (191 mm^2) and the friction force against the walls of the matrix (11 % of the force). The density of the powder compacts and sintered samples was determined by hydrostatic weighing on Vibra scales (Shinko, Japan). The relative densities of the powder compacts and sintered samples were calculated based on the known densities of the WC–5TiC–10Co alloy (12.95 g/cm^3) and rubber (0.9 g/cm^3). Plasticizer removal and sintering were performed in a Carbolite STF vacuum furnace (Carbolite Gero, UK). Strength testing of rectangular samples was carried out according to standard methodology (ISO 3327:2009). Carbon content in the powders was measured on an EMIA 320V2 analyzer (Horiba Ltd., Japan) after the removal of the plasticizer by heating along with other samples. The microstructure of the sintered hard alloy products was examined using optical (Altami, St. Petersburg) and scanning electron microscopes (Tescan Orsay Holding, Czech Republic). The average grain diameter was calculated using standard methodology (ASTM E112-13). The Vickers hardness of all samples was determined using an HVS-50 hardness tester (Time Group Inc., China) (with an accuracy of 2 %) at a load of $P = 294$ N. Fracture toughness (K_{1c}) was calculated based on the total crack length (Σl) from the hardness tester indenter using the Palmqvist method (ISO 28079) at a load of $P = 294$ N according to the Shetty equation:

$$K_{1c} = 0.0028\sqrt{HV\frac{P}{\Sigma l}}. \qquad (1)$$

The performance characteristics of the obtained cutting insert (1 % rubber, pressure of 50 MPa) and the commercial insert were determined during rough turning (cutting speed of 100 ± 10 m/min, depth of 1.5 mm, feed of 0.2 mm/rev, duration of 3.5 min, length of 330 m) and finishing (cutting speed of 125 ± 15 m/min, depth of 0.2 mm, feed of 0.05 mm/rev, duration of 10.5 min, length of 1320 m) of a cylindrical workpiece with a diameter of 50 to 60 mm made of steel 45 on a 16K20 lathe (Krasny Proletary Plant, Moscow). The profiles of the rear surfaces of the cutting inserts and steel workpieces were examined using a Tr-200 profilometer (Time Group Inc., China).

Results and discussion

The observed ability of polylactide punches to withstand a pressing pressure of 70 MPa, exceeding the yield strength of this material, is explained by the fact that, according to the von Mises criterion, under such a load, the resulting equivalent stress decreases due to the presence of the second and third principal stresses within the steel shell (Fig. 1, *b*, *c*). Additionally, friction between the punch, the matrix walls, and the pusher leads to a reduction (by 11 ± 5 %) in the pressure exerted on the blank. The dependence of the relative density of the blanks (ρ) on the pressure (P) (Fig. 2, *a*) is well described by the known relationship [31]:

$$\rho = A + B\ln P. \qquad (2)$$

The parameter B characterizes the rate of density increase with increasing pressure. Thus, as the pressing pressure increases from 50 to 200 MPa, the density of the blanks increases by 2–6 % for different plasticizer concentrations (Fig. 2, *a*), in full agreement with the relationship (2). The relatively small density increase with increasing pressure should prevent uneven density distribution during blank pressing. The coefficient A in equation (2) shows the density achieved at the initial stage of pressing at relatively low pressure, which depends on the plasticizer content and other parameters of the mixture. The relative density of the blanks pressed at 50 MPa increases from 62 to 95 % as the plasticizer concentration increases from 1 to 6 % (Fig. 2, *b*).

An increase in the plasticizer fraction from 1 to 6 % leads to a 28–32 % increase in blank density at various pressing pressures (Fig. 2, *b*), which is significantly greater than the density increase caused by increasing the pressing pressure (Fig. 2, *a*). The density of all the obtained blanks exceeded the density of blanks manufactured using other 3D printing methods by 20–45 % [19; 21–23; 28; 32]. This is primarily due to the fact that in 3D printing, direct compaction occurs only under the influence of gravity and surface tension forces. Fig. 2, *a* and *b* show that the density of the blanks obtained in a steel mold at 200 MPa is no different from the density of the blanks obtained in a plastic mold at the same pressure and plasticizer content.

For the sintered samples, it was found that changes in pressing pressure have almost no effect on their density (Fig. 2, *c*). Increasing the rubber concentration from 1

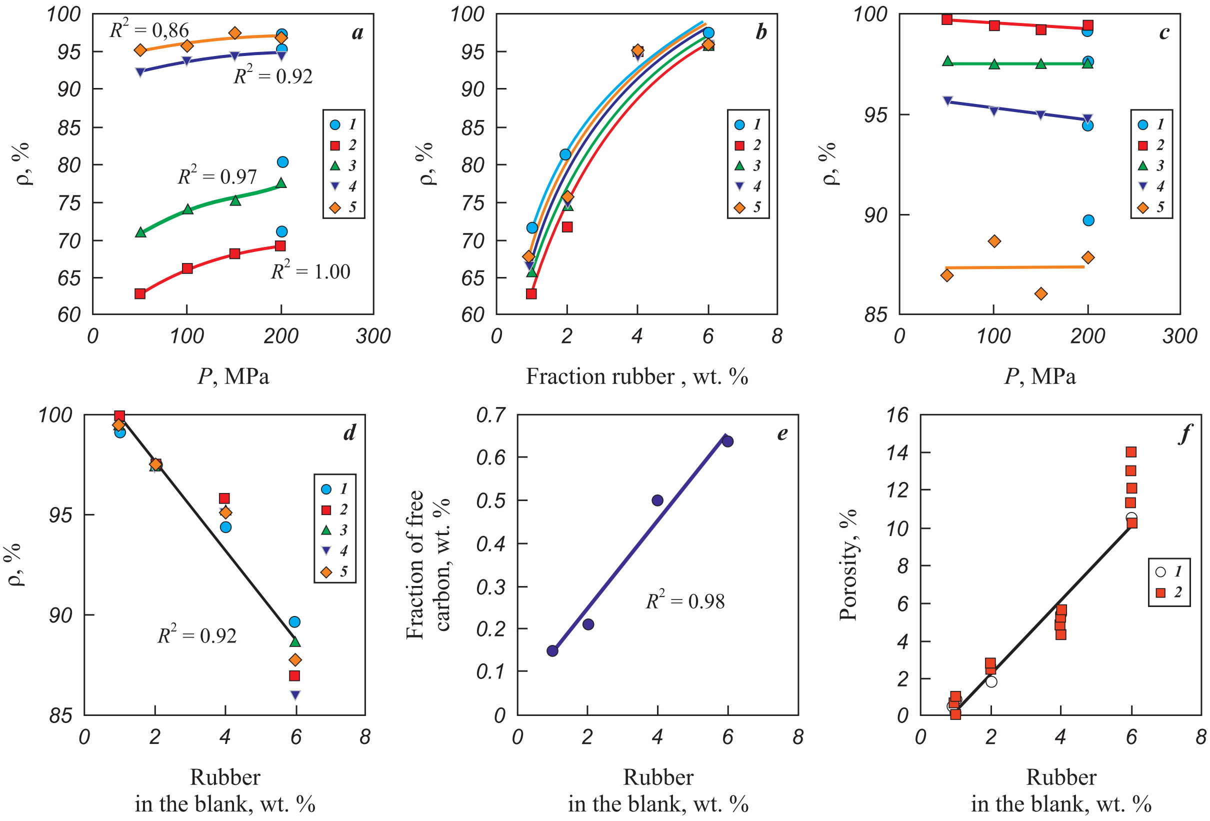

Fig. 2. Dependence of the density of compacts (***a***, ***b***) and sintered samples (***c***, ***d***) on pressure (***a***, ***c***) and rubber concentration (***b***, ***d***). Dependence of free carbon concentration (***e***) and porosity (***f***) of sintered samples on the rubber concentration of in the blank

a, ***c***: ***1*** – stell mold; ***2–5*** – PLA mold; ***2*** – 1 % rubber, ***3*** – 2 %, ***4*** – 4 %, ***5*** – 6 %
b, ***d***: ***1*** – stell mold, ***2–5*** – PLA mold; *P*, MPa – 50 (***2***), 100 (***3***), 150 (***4***), 200 (***1***, ***5***)
f: ***1*** – calculated value, ***2*** – microstructure analysis

Рис. 2. Зависимость плотности прессовок (***a***, ***b***) и спеченых образцов (***c***, ***d***) от давления (***a***, ***c***) и концентрации каучука (***b***, ***d***). Зависимость концентрации свободного углерода (***e***) и пористости (***f***) спеченных образцов от концентрации каучука в заготовке

a, ***c***: ***1*** – стальная пресс-форма; ***2–5*** – PLA-форма; ***2*** – 1 % каучука, ***3*** – 2 %, ***4*** – 4 %, ***5*** – 6 %
b, ***d***: ***1*** – стальная пресс-форма, ***2–5*** – PLA-форма; *P*, МПа – 50 (***2***), 100 (***3***), 150 (***4***), 200 (***1***, ***5***)
f: ***1*** – расчетное значение, ***2*** – анализ микроструктуры

to 6 % leads to a decrease in the density of the products from 99.3–99.8 to 86.0–88.6 % (Fig. 2, *d*), which is due to the increase in free carbon concentration formed during rubber decomposition. Analysis showed that the amount of free carbon in the sintered samples increases linearly from 0.15 to 0.64 % as the rubber concentration in the blanks rises from 1 to 6 % (Fig. 2, *e*), corresponding to the formation of approximately 0.1 % free carbon per 1 % rubber. The increase in the porosity of the samples correlates well with the increase in free carbon content (Fig. 2, *f*), meaning the pores detected in the microstructure are actually inclusions of free carbon. The porosity values obtained by analyzing their share in the microstructure surface area (Fig. 3, *a*–*e*) also fit this pattern (Fig. 2, *f*). It should be noted that the relative density (99.8 %) of the sample pressed at 50 MPa from powder containing 1 % rubber is equal to the density of the commercial cutting insert (99.8 %).

The sintered samples also do not fall behind in relative density compared to the best WC–Co alloy samples with cobalt content up to 15 %, obtained by direct SLM and SLS methods (densities, %: 96 [5], 96.1 [11], 97.3 [16], 92.4 [17], 98 [33], 97.4 [34]). There is a slight lag in relative density compared to the samples produced by sintering blanks obtained by BJ (100 % [23], 100 % [24]) and FFF methods (>99 % [35]). Considering that the density of the blanks obtained by BJ and FFF methods (20–45 %) is significantly lower than the density of the blanks obtained in this study (65–95 %) (Fig. 2, *a*, *b*), it can be assumed that the slight lag in density of the obtained sintered samples (1 %) is due to the lower sinterability of the WC–TiC–Co alloy compared to WC–Co alloys and the less advanced sintering method (LPS).

The projections of the obtained and commercial cutting inserts are similar to each other (Fig. 4, *a*, *d*).

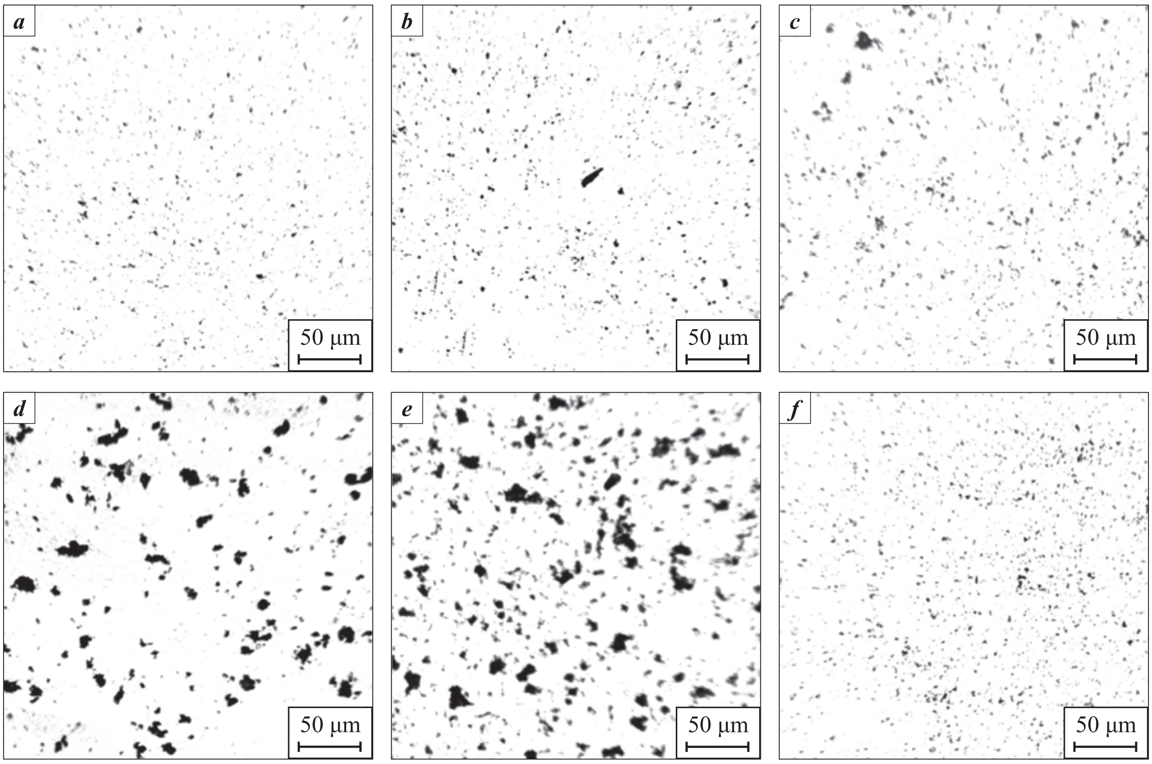

Fig. 3. Microstructures of samples sintered after pressing at pressing at 50 MPa (***a***, ***c***–***e***) and 200 MPa (***b***) with varying plasticizer content, and the microstructure of the commercial sample (***f***)

Rubber content, wt. % – 1 (***a***, ***b***), 2 (***c***), 4 (***d***), 6 (***e***)

Рис. 3. Микроструктуры образцов, спеченных после прессования при давлении 50 МПа (***a***, ***c***–***e***) и 200 МПа (***b***) при различном содержании пластификатора и микроструктура коммерческого образца (***f***)

Доля каучука, мас. % – 1 (***a***, ***b***), 2 (***c***), 4 (***d***), 6 (***e***)

The surface of the insert sintered after pressing in a plastic mold is distinguished by the characteristic traces of layers obtained during 3D printing. In addition, the microstructure of the obtained sample shows defects formed during the separation of the plastic punch from the blank. The side surface does not have such defects. There are no large defects on the polished section that would differentiate the obtained sample (Fig. 4, *b*) from the commercial counterpart (Fig. 4, *e*). Microstructure analysis showed that the obtained sample (Fig. 4, *c*) has a larger carbide grain size (average WC grain diameter d_{avg} = 1.26 μm) compared to the commercial counterpart (Fig. 4, *f*) (d_{avg} = 0.88 μm). It can be expected that the other samples also have a larger average grain diameter.

The hardness of the samples pressed in the plastic mold increases from 1010 to 1400 HV as their density rises from 85.0 to 98.7 % (Fig. 5, *a*). Measurements showed that the fracture toughness of these samples is largely independent of their density (Fig. 5, *b*). The presented dependencies (Fig. 5, *a*, *b*) show that the commercial cutting insert has higher hardness (1450 ± 10 HV) and lower fracture toughness (12.1 ± 0.4 MPa·m$^{1/2}$). According to the analysis of sintered samples obtained by pressing in a steel mold, their strength increases with rising density (Fig. 5, *c*).

Profile measurements of the cutting inserts (Fig. 6) showed that the roughness of the experimental tool was predictably higher than that of the commercial cutting insert (see Table), due to surface micro-irregularities formed during pressing. These irregularities resulted from the adhesion of plastic to the blank and the replication of imperfections in the plastic mold's surface, which were introduced during 3D printing.

Hardness and roughness are the primary factors influencing the performance of both the experimental (Fig. 7, *a*, *b*) and commercial (Fig. 7, *c*, *d*) cutting inserts, made from the same material, during rough (Fig. 7, *a*, *c*) and finishing (Fig. 7, *b*, *d*) turning. The increased roughness and lower hardness of the experimental insert resulted in 5–7 % higher surface roughness on the workpieces after both rough and finishing turning compared to the commercial insert (see Table).

Adhesive wear of the WC–5TiC–10Co alloy cutting inserts during carbon steel turning, where continuous chips are formed (Fig. 7, *a*, *c*), predominates over other types of wear. In this process, the composition

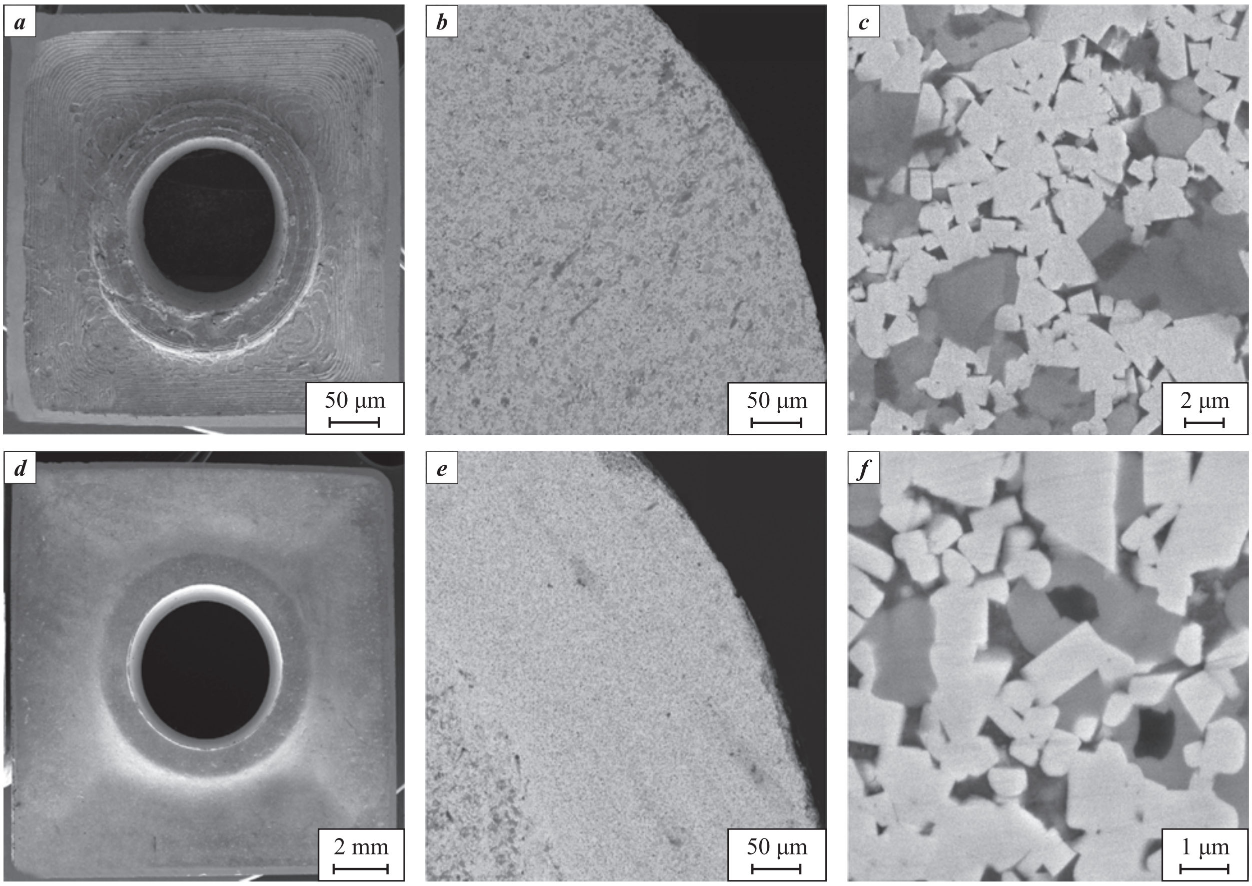

Fig. 4. Macrostructures (***a***, ***d***) and microstructures (***b***, ***c***, ***e***, ***f***) of the WC–5TiC–10Co hard alloy insert (***a***–***c***) sintered after pressing the powder in a plastic mold (*P* = 50 MPa, 1 % rubber), and the commercial cutting insert SNUM 120408 made from T5K10 alloy (***d***–***f***)

Рис. 4. Макроструктуры (***a***, ***d***) и микроструктуры (***b***, ***c***, ***e***, ***f***) твердосплавной вставки WC–5TiC–10Co (***a***–***c***), спеченной после прессования порошка в пластиковой пресс-форме (*P* = 50 МПа, 1 % каучука), и коммерческой режущей пластины SNUM 120408 из сплава T5K10 (***d***–***f***)

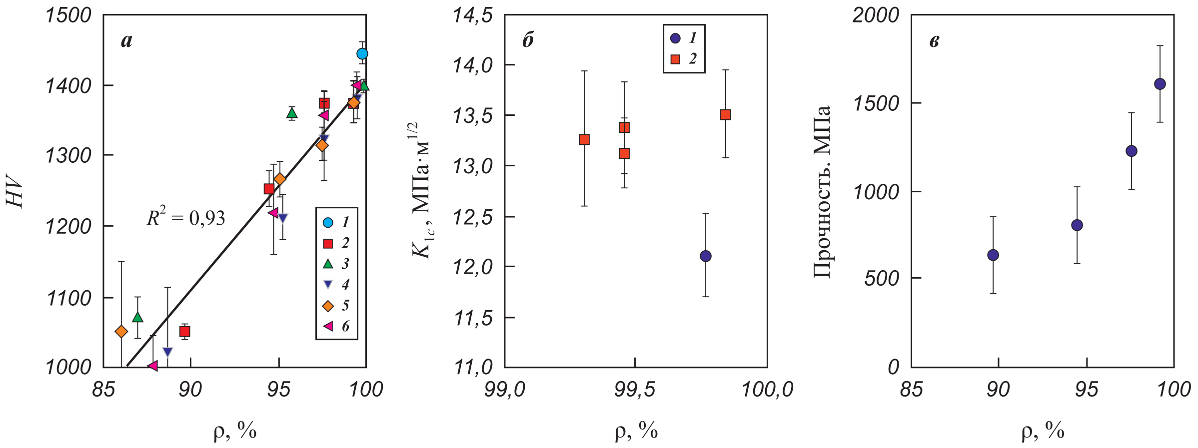

Fig. 5. Dependence of hardness (***a***), fracture toughness (***b***), and strength (***c***) of the obtained samples on their density

a: ***1*** – commercial T5K10 insert; ***2*** – steel mold; ***3–6*** – PLA form
P, MPa: 200 (***2***), 50 (***3***), 100 (***4***), 150 (***5***), 200 (***6***)
b: ***1*** – commercial T5K10 insert; ***2*** – experimental samples

Рис. 5. Зависимость твердости (***a***), вязкости разрушения (***b***) и прочности (***c***) полученных образцов от их плотности

a: ***1*** – коммерческая пластина T5K10; ***2*** – стальная пресс-форма; ***3–6*** – PLA-форма
P, МПа: 200 (***2***), 50 (***3***), 100 (***4***), 150 (***5***), 200 (***6***)
b: ***1*** – коммерческая пластина T5K10; ***2*** – экспериментальные образцы

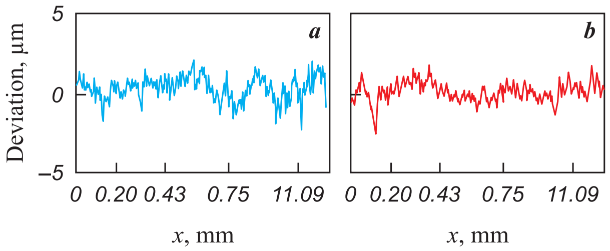

Fig. 6. Profile of the side surface of the experimental (***b***) and the commercial (***a***) cutting inserts

Рис. 6. Профиль боковой поверхности экспериментальной (***b***) и коммерческой (***a***) режущих пластин

of the cutting inserts plays the most significant role, and since the composition is the same in both cases, differences in hardness have less impact. The wear on the rear edge of the experimental cutting insert during both rough and finishing turning was 5–6 % higher than that of the commercial counterpart. In this case, the main cause was the difference in hardness.

Conclusions

The experimental results confirmed that using a polylactide mold produced by additive manufactu-

Results of testing cutting inserts when turning steel 45

Результаты испытания режущих пластин при точении стали 45

Sample	Roughness of the rear surface of the insert, R_a, µm	Roughness of the workpiece, R_a, µm		Wear on the rear edge, µm	
		after rough turning	after finishing turning	after rough turning	after finishing turning
Experimental	0.64 ± 0.08	3.90 ± 0.43	2.34 ± 0.23	101	149
Commercial	0.55 ± 0.10	3.68 ± 0.18	2.19 ± 0.19	96	141

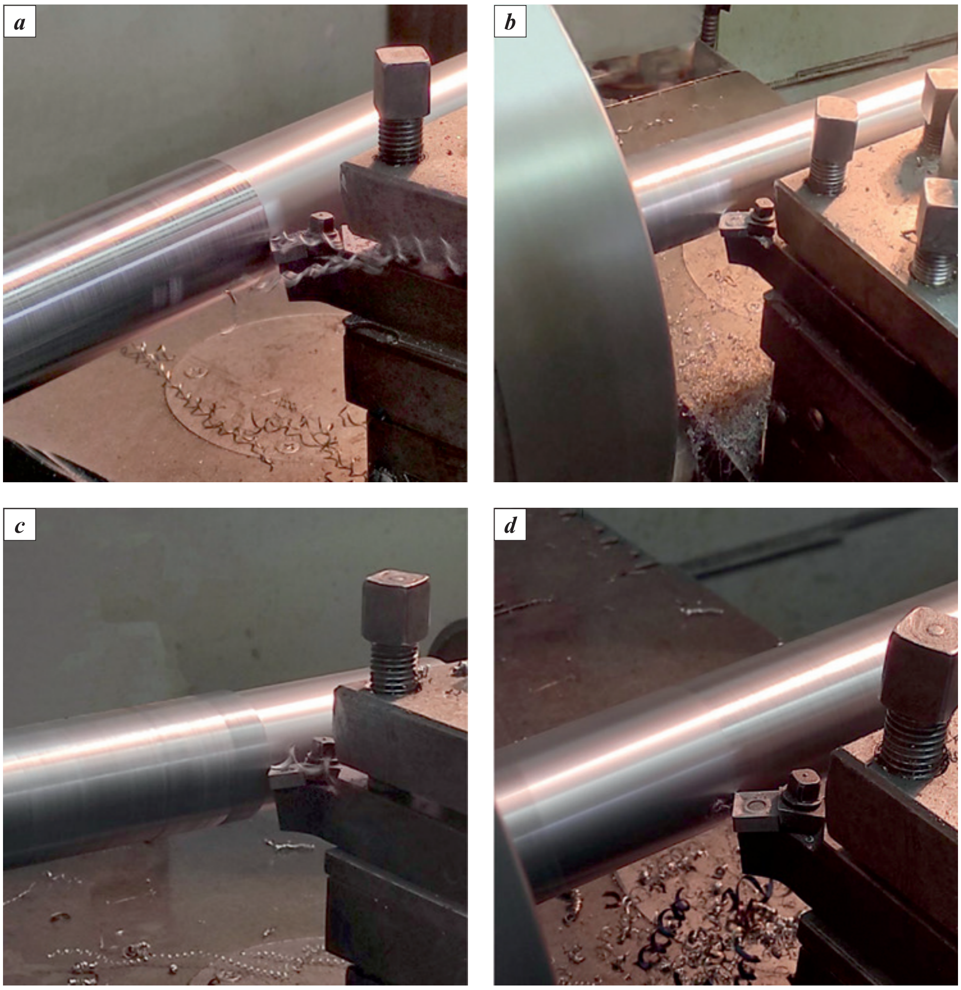

Fig. 7. Rough (***a***, ***c***) and finishing (***b***, ***d***) turning using the experimental (***a***, ***b***) and a commercial (***c***, ***d***) cutting insert

Рис. 7. Черновое (***a***, ***c***) и чистовое (***b***, ***d***) точение экспериментальной (***a***, ***b***) и коммерческой (***c***, ***d***) режущих пластин ring, complemented by a steel shell and pusher, enables the pressing of hard alloy blanks at pressures up to 200 MPa. The density of the cutting insert blanks pressed in these molds from WC–5TiC–10Co is only slightly different from the density of blanks produced in steel molds at the same pressure. As pressing pressure increases, the density of the blanks grows only by 2–6 %, while increasing the plasticizer concentration in the initial powder mixture by 1 to 6 % results in a more significant density increase of 28–32 %.

The pressing pressure has little impact on the density of sintered cutting inserts. As the plasticizer concentration increases (from 1 to 6 %), the free carbon concentration rises (from 0.15 to 0.64 %), which leads to a decrease in the relative density, hardness, and strength of the samples. Cutting inserts made from WC–5TiC–10Co powder with 1 % plasticizer have similar density and porosity to commercial T5K10 inserts. However, they exhibit lower hardness (1400 ± 10 HV) and higher fracture toughness (135 ± 0.4 MPa·m$^{1/2}$) compared to commercial samples (1447 ± 15 HV and 121 ± 0.4 MPa·m$^{1/2}$) of the same alloy, primarily due to the larger average WC grain size. The wear rate of the experimental cutting insert is 5–7 % higher than that of the commercial tool, due to its lower hardness and higher surface roughness.

References / Список литературы

1. Anisimenko G.E., Lopatin Yu.M. New hard alloys for indexable multifaceted inserts. *Obrabotka metallov (Tekhnologii, oborudovanie, instrumenty)*. 2008;4(41):25–33. (In Russ.).

Анисименко Г.Е., Лопатин Ю.М. Новые твердые сплавы для сменных многогранных пластин. *Обработка металлов (Технология, оборудование, инструменты)*. 2008;4(41):25–33.

2. Aramian A., Razavi N., Sadeghian Z., Berto F. A review of additive manufacturing of cermets. *Additive Manufacturing*. 2020;33:101130.
https://doi.org/10.1016/j.addma.2020.101130

3. Yang Y., Zhang C., Wang D., Nie L., Wellmann D., Tian Y. Additive manufacturing of WC–Co hardmetals: A review. *The International Journal of Advanced Manufacturing Technology*. 2020;108:1653–1673.
https://doi.org/10.1007/s00170-020-05389-5

4. Chen C., Huang B., Liu Z., Li Y., Zou D., Liu T., Chang Y., Chen L. Additive manufacturing of WC–Co cemented carbides: Process, microstructure, and mechanical properties. *Additive Manufacturing*. 2023:10341.
https://doi.org/10.1016/j.addma.2023.103410

5. Chen J., Huang M., Fang Z.Z., Koopman M., Liu W., Deng X., Zhao Z., Chen S., Wu S., Liu J., Qi W., Wang Z. Microstructure analysis of high density WC–Co composite prepared by one step selective laser melting. *International Journal of Refractory Metals and Hard Materials*. 2019;84:104980.
https://doi.org/10.1016/j.ijrmhm.2019.104980

6. Li C.W., Chang K.C., Yeh A.C. On the microstructure and properties of an advanced cemented carbide system processed by selective laser melting. *Journal of Alloys and Compounds*. 2019;782:440–450.
https://doi.org/10.1016/j.jallcom.2018.12.187

7. Gu D., Meiners W. Microstructure characteristics and formation mechanisms of in situ WC cemented carbide based hardmetals prepared by Selective Laser Melting. *Materials Science and Engineering: A*. 2010;527(29–30):7585–7592.
https://doi.org/10.1016/j.msea.2010.08.075

8. Domashenkov A., Borbély A., Smurov I. Structural modifications of WC/Co nanophased and conventional powders processed by selective laser melting. *Materials and Manufacturing Processes*. 2017;32(1):93–100.
https://doi.org/10.1080/10426914.2016.1176195

9. Fortunato A., Valli G., Liverani E., Ascari A.. Additive manufacturing of WC–Co cutting tools for gear production. *Lasers in Manufacturing and Materials Processing*. 2019;6:247–262.
https://doi.org/10.1007/s40516-019-00092-0

10. Khmyrov R.S., Shevchukov A.P., Gusarov A.V., Tarasova T.V. Phase composition and microstructure of WC–Co alloys obtained by selective laser melting. *Mechanics & Industry*. 2017;18(7):714.
https://doi.org/10.1051/meca/2017059

11. Ku N., Pittari III J.J., Kilczewski S., Kudzal A. Additive manufacturing of cemented tungsten carbide with a cobalt-free alloy binder by selective laser melting for high-hardness applications. *Journal of the Minerals, Metals and Materials Socity (JOM)*. 2019;71(4):1535–1542.
https://doi.org/10.1007/s11837-019-03366-2

12. Zhang L., Hu C., Yang Y., Misra R.D.K., Kondoh K., Lu Y. Laser powder bed fusion of cemented carbides by developing a new type of Co coated WC composite powder. *Additive Manufacturing*. 2022;55:102820.
https://doi.org/10.1016/j.addma.2022.102820

13. Suzuki A., Shiba Y., Ibe H., Takata N., Kobashi M. Machine-learning assisted optimization of process parameters for controlling the microstructure in a laser powder bed fused WC/Co cemented carbide. *Additive Manufacturing*. 2022;59:103089.
https://doi.org/10.1016/j.addma.2022.103089

14. Maurya H.S., Kosiba K., Juhani K., Sergejev F., Prashanth K.G. Effect of powder bed preheating on the crack formation and microstructure in ceramic matrix composites fabricated by laser powder-bed fusion process. *Additive Manufacturing*. 2022;58:103013.
https://doi.org/10.1016/j.addma.2022.103013

15. Padmakumar M. Additive manufacturing of tungsten carbide hardmetal parts by selective laser melting (SLM), selective laser sintering (SLS) and binder jet 3D printing (BJ3DP) techniques. *Lasers in Manufacturing and Materials Processing*. 2020;7(3):338–371.
https://doi.org/10.1007/s40516-020-00124-0

16. Mostafaei A., De Vecchis P.R., Kimes K.A., Elhassid D., Chmielus M. Effect of binder saturation and drying time on microstructure and resulting properties of sinter-HIP binder-jet 3D-printed WC–Co composites. *Additive*

Manufacturing. 2021;46:102128.
https://doi.org/10.1016/j.addma.2021.102128

17. Mariani M., Goncharov I., Mariani D., De Gaudenzi G.P., Popovich A., Lecis N., Vedani M. Mechanical and microstructural characterization of WC–Co consolidated by binder jetting additive manufacturing. *International Journal of Refractory Metals and Hard Materials*. 2021;100:105639.
https://doi.org/10.1016/j.ijrmhm.2021.105639
18. Cramer C.L., Wieber N.R., Aguirre T.G., Lowden R.A., Elliott A.M. Shape retention and infiltration height in complex WC–Co parts made via binder jet of WC with subsequent Co melt infiltration. *Additive Manufacturing*. 2019;29:100828.
https://doi.org/10.1016/j.addma.2019.100828
19. Cramer C.L., Nandwana P., Lowden R.A., Elliott A.M. Infiltration studies of additive manufacture of WC with Co using binder jetting and pressureless melt method. *Additive Manufacturing*. 2019;28:333–343.
https://doi.org/10.1016/j.addma.2019.04.009
20. Enneti R.K., Prough K.C., Wolfe T.A., Klein A., Studley N., Trasorras J.L. Sintering of WC–12%Co processed by binder jet 3D printing (BJ3DP) technology. *International Journal of Refractory Metals and Hard Materials*. 2018;71:28–35.
https://doi.org/10.1016/j.ijrmhm.2017.10.023
21. Kim H., Kim J.I., Do Kim Y., Jeong H., Ryu S.S. Material extrusion-based three-dimensional printing of WC–Co alloy with a paste prepared by powder coating. *Additive Manufacturing*. 2022;52:102679.
https://doi.org/10.1016/j.addma.2022.102679
22. Tang J.Y., Lu L.M., Li Z., Za X., Wu Y.C. Shape retention of cemented carbide prepared by Co melt infiltration into un-sintered WC green parts made via BJ3DP. *International Journal of Refractory Metals and Hard Materials*, 2022;107:105904.
https://doi.org/10.1016/j.ijrmhm.2022.105904
23. Wolfe T., Shah R., Prough K., Trasorras J.L. Coarse cemented carbide produced via binder jetting 3D printing. *International Journal of Refractory Metals and Hard Materials*. 2023;110:106016.
https://doi.org/10.1016/j.ijrmhm.2022.106016
24. Lengauer W., Duretek I., Fürst M., Schwarz V., Gonzalez-Gutierrez J., Schuschnigg S., Kukla C., Kitzmantel M., Neubauer E., Lieberwirth C., Morrison V. Fabrication and properties of extrusion-based 3D-printed hardmetal and cermet components. *International Journal of Refractory Metals and Hard Materials*. 2019:82:141–149.
https://doi.org/10.1016/j.ijrmhm.2019.04.011
25. Carreño-Morelli E., Alveen P., Moseley S., Rodriguez-Arbaizar M., Cardoso K. Three-dimensional printing of hard materials. *International Journal of Refractory Metals and Hard Materials*. 2020;87:105110.
https://doi.org/10.1016/j.ijrmhm.2019.105110
26. Zhang X., Guo Z., Chen C., Yang W. Additive manufacturing of WC–20Co components by 3D gel-printing. *International Journal of Refractory Metals and Hard Materials*. 2018;70:215–223.
https://doi.org/10.1016/j.ijrmhm.2017.10.005
27. Kim H., Kim J.I., Ryu S.S., Jeong H. Cast WC–Co alloy-based tool manufacturing using a polymeric mold prepared via digital light processing 3D printing. *Materials Letters*. 2022;306:130979.
https://doi.org/10.1016/j.matlet.2021.130979
28. Liu K., Zhou C., Chen F., Sun H., Zhang K. Fabrication of complicated ceramic parts by gelcasting based on additive manufactured acetone-soluble plastic mold. *Ceramics International*. 2020;46(16):25220–25229.
https://doi.org/10.1016/j.ceramint.2020.06.313
29. Dvornik M.I., Mikhailenko E.A., Burkov A.A., Kolzun D.A., Shichalin O.O. 3D printed plastic molds utilization for WC–15Co cemented carbide cold pressing. *International Journal of Refractory Metals and Hard Materials*. 2023;106312.
https://doi.org/10.1016/j.ijrmhm.2023.106312
30. Dvornik M.I., Mikhailenko E.A., Burkov A.A., Kol'zun D.A. Dependence of the density, hardness, strength and sizes of WC–15Co hard alloy samples on the plasticizer content in samples got using a 3D printed mold. *Perspektivnye materialy*. 2024;(3):33–44. (In Russ.).
https://doi.org/10.30791/1028-978X-2024-3-33-44

Дворник М.И., Михайленко Е.А., Бурков А.А., Кользун Д.А. Зависимость плотности, твердости, прочности и размеров образцов твердого сплава WC–15Co от содержания пластификатора в заготовках, полученных при использовании пластиковой пресс-формы, изготовленной методом 3D-печати. *Перспективные материалы*. 2024;(3):33–44.
https://doi.org/10.30791/1028-978X-2024-3-33-44

31. Niesz D.E. A review of ceramic powder compaction. *KONA Powder and Particle Journal*. 1996;14:44–51.
https://doi.org/10.14356/kona.1996009
32. Xu Z.K., Meenashisundaram G.K., Ng F.L. High-density WC–45Cr–18Ni cemented hard metal fabricated with binder jetting additive manufacturing. *Virtual and Physical Prototyping*. 2022;17(1):92–104.
https://doi.org/10.1080/17452759.2021.1997006
33. Konyashin I., Hinners H., Ries B., Kirchner A., Kloeden B., Kieback B., Nilen R.W.N., Sidorenko D. Additive manufacturing of WC–13%Co by selective electron beam melting: Achievements and challenges. *International Journal of Refractory Metals and Hard Materials*. 2019;84:105028.
https://doi.org/10.1016/j.ijrmhm.2019.105028
34. Fries S., Vogelpoth A., Kaletsch A., Broeckmann C. Influence of post heat treatment on microstructure and fracture strength of cemented carbides manufactured using laser-based additive manufacturing. *International Journal of Refractory Metals and Hard Materials*. 2023;111:106085.
https://doi.org/10.1016/j.ijrmhm.2022.106085
35. Zhao Z., Liu R., Chen J., Xiong X. Additive manufacturing of cemented carbide using analogous powder injection molding feedstock. *International Journal of Refractory Metals and Hard Materials*. 2023;111:106095.
https://doi.org/10.1016/j.ijrmhm.2022.106095

Information about the Authors

Maksim I. Dvornik – Cand. Sci. (Eng.), Senior Researcher, Head of the Laboratory of Powder Metallurgy, Institute of Materials Science, Khabarovsk Federal Research Center, Far Eastern Branch of the Russian Academy of Sciences (IMS KhFRC of FEB RAS)
ORCID: 0000-0002-1216-4438
E-mail: maxxxx80@mail.ru

Elena A. Mikhailenko – Cand. Sci. (Phys.-Math.), Senior Researcher, Laboratory of Powder Metallurg, IMS KhFRC FEB RAS
ORCID: 0000-0002-4515-9109
E-mail: mea80@list.ru

Aleksandr A. Burkov – Cand. Sci. (Phys.-Math.), Senior Researcher, Head of the Laboratory “Physical and Chemical Bases of Materials”, IMS KhFRC FEB RAS
ORCID: 0000-0002-5636-4669
E-mail: burkovalex@mail.ru

Evgeny V. Chernyakov – Laboratory Assistant, Laboratory of Powder Metallurgy, IMS KhFRC FEB RAS
E-mail: tchernyakoffevgeny@yandex.ru

Сведения об авторах

Максим Иванович Дворник – к.т.н., ст. науч. сотрудник, заведующий лабораторией порошковой металлургии, Институт материаловедения Хабаровского федерального исследовательского центра Дальневосточного отделения РАН (ИМ ХФИЦ ДВО РАН)
ORCID: 0000-0002-1216-4438
E-mail: maxxxx80@mail.ru

Елена Альбертовна Михайленко – к.ф.-м.н., ст. науч. сотрудник лаборатории порошковой металлургии ИМ ХФИЦ ДВО РАН
ORCID: 0000-0002-4515-9109
E-mail: mea80@list.ru

Александр Анатольевич Бурков – к.ф.-м.н., ст. науч. сотрудник, заведующий лабораторией «Физико-химические основы материалов» ИМ ХФИЦ ДВО РАН
ORCID: 0000-0002-5636-4669
E-mail: burkovalex@mail.ru

Евгений Витальевич Черняков – лаборант лаборатории порошковой металлургии ИМ ХФИЦ ДВО РАН
E-mail: tchernyakoffevgeny@yandex.ru

Contribution of the Authors

M. I. Dvornik – defined he research objectives, conducted experiments, developed the plastic molds, authored the article, and formulated the study’s conclusions.

E. A. Mikhailenko – prepared the mixtures and initial samples, participated in the discussion of the results, and contributed to writing the article.

A. A. Burkov – conducted experiments and contributed to the discussion of the results.

E. V Chernyakov – prepared the mixtures and initial samples, and pressed the cutting inserts.

Вклад авторов

М. И. Дворник – определение цели работы, разработка пластиковых пресс-форм, проведение экспериментов, анализ результатов, написание статьи, формулировка выводов исследования.

Е. А. Михайленко – приготовление смесей и исходных образцов, участие в обсуждении результатов, написание статьи.

А. А. Бурков – проведение экспериментов, участие в обсуждении результатов.

Е. В. Черняков – приготовление смесей и исходных образцов, прессование режущих пластин.

Received 11.03.2024
Revised 27.04.2024
Accepted 30.04.2024

Статья поступила 11.03.2024 г.
Доработана 27.04.2024 г.
Принята к публикации 30.04.2024 г.

Application of Powder Materials and Functional Coatings
Применение порошковых материалов и функциональных покрытий

UDC 669.13

https://doi.org/10.17073/1997-308X-2024-5-66-74

Research article
Научная статья

Prospects for the use of graphite-containing sludge for the production of composite coatings

S. A. Khudonogov

Siberian Federal University
79 Svobodny Prosp., Krasnoyarsk 660041, Russia

shudonogov@sfu-kras.ru

Abstract. Modern technologies must meet the criteria of sustainable development, taking into account economic, environmental, and social indicators. In this study, the potential use of graphite-containing sludge from the gas purification aspiration system during cryptocrystalline graphite production was investigated for its inclusion in composite anti-burn coatings for cast iron casting. The graphite-containing sludge consists of carbon, sulfur, sodium, aluminum, and silicon, with a phase composition that includes graphite, calcite, pyrite, quartz, halite, and others. The sludge is a dispersed material with an average particle size of 3.64 μm, a total surface area of 36,506 cm^2/cm^3, and a main fraction size of 1–8 μm. Sludge particles exhibit various shapes, ranging from irregular to isometric. Larger isometric particles can reach sizes of 1 mm or more. On the surfaces of larger particles, smaller dispersed particles are present. The structural parameters of the sludge correspond to those of hexagonal graphite. The analysis of the composition and properties of graphite-containing sludge suggests its suitability for use in composite anti-burn coating formulations. However, due to the presence of large graphite aggregates and acicular impurities in the sludge, sieving is required before use. Complete replacement of natural graphite with sludge increases the coating density from 1220 to 1750 kg/m^3, viscosity from 34 to 105 s, and abrasion resistance from 175 to 245 g/mm. Due to its high dispersity, the sludge-based coating nearly completely penetrates the pores of the sand-resin mixture mold without forming a cover layer. This does not ensure consistent reduction of burn-on defects on casting surfaces. Therefore, the full substitution of graphite with graphite-containing sludge in composite coating formulations is not recommended.

Keywords: self-drying coating, graphite-containing sludge, cast iron, burn-on, density, viscosity, thickness of the coating layer, depth of the penetrating layer, abrasion resistance

For citation: Khudonogov S.A. Prospects for the use of graphite-containing sludge for the production of composite coatings. *Powder Metallurgy and Functional Coatings*. 2024;18(5):66–74. https://doi.org/10.17073/1997-308X-2024-5-66-74

Перспективы применения графитсодержащего шлама для изготовления композиционных покрытий

С. А. Худоногов

Сибирский федеральный университет
Россия, 660041, г. Красноярск, пр. Свободный, 79

shudonogov@sfu-kras.ru

Аннотация. Современные технологии должны соответствовать критериям устойчивого развития, учитывающим экономические, экологические и социальные показатели. Поэтому в работе исследовали возможность вовлечения графитсодержащего шлама из аспирационной системы очистки газов при производстве скрытокристаллического графита в состав композиционных противопригарных покрытий для чугунного литья. Графитсодержащий шлам представлен углеродом, серой, натрием, алюминием и кремнием, фазовый состав – графитом, кальцитом, пиритом, кварцем, галитом и др. Шлам – дисперсный материал со средним размером частиц 3,64 мкм, общей поверхностью 36 506 см^2/см^3 и основной фракцией 1–8 мкм. Для частиц шлама характерны различные формы – от неправильных до изометрических. Размеры крупных частиц изометрической формы могут достигать 1 мм и более. На поверхности крупных частиц присутствуют более мелкие дисперсные частицы. Параметры структуры шлама соответствуют параметрам гексагональной формы графита. Анализ состава и свойств графитсодержащего шлама позволяет рекомендовать его применение в составах композиционных противопригарных покрытий. Однако из-за наличия в составе шлама крупных агрегатов графита и примесей игольчатого характера его перед использованием необходимо просеивать. Полная замена природного графита на шлам позволяет повысить плотность покрытия с 1220 до 1750 кг/м^3, вязкость – с 34 до 105 с и прочность к истиранию – с 175 до 245 г/мм. Из-за высокой дисперсности покрытие на основе шлама практически полностью проникает в поры формы из песчано-смоляной смеси, не образуя при этом покровного слоя. Это не обеспечивает стабильного снижения пригара на поверхности отливок. Поэтому полная замена графита на графитсодержащий шлам в составах композиционных покрытий не рекомендуется.

Ключевые слова: самовысыхающее покрытие, графитсодержащий шлам, чугун, пригар, плотность, вязкость, толщина покровного слоя, глубина проникающего слоя, прочность к истиранию

Для цитирования: Худоногов С.А. Перспективы применения графитсодержащего шлама для изготовления композиционных покрытий. *Известия вузов. Порошковая металлургия и функциональные покрытия*. 2024;18(5):66–74. https://doi.org/10.17073/1997-308X-2024-5-66-74

Introduction

In the last decade, the criteria for product quality have changed, as modern technologies must meet the criteria of sustainable development, which take into account economic, environmental, and social indicators [1–4]. As a result, increasing attention is being paid to the potential for incorporating industrial powder waste into various sectors of industry [5–13].

The experience of using carbon-containing slags from various productions in the compositions of different products has been described in works [14–16]. The advantages of using carbon-containing waste not only enhance the quality of products based on them but also reduce the volume of sludge fields surrounding enterprises, thus contributing to environmental preservation. For example, the processing of graphite-containing dust from metallurgical production allows for the production of high-quality raw materials for a wide range of applications, while also generating additional profit by lowering production costs. On the other hand, the variable composition of the waste, which determines the nature of its thermal degradation, along with insufficient development of technologies, results in the majority of the waste currently being sent to landfills.

In the Krasnoyarsk region, there is a graphite processing enterprise working with the Kureiskoye deposit, which primarily produces cryptocrystalline graphite of the GLS grade, carburizer of the NSGK grade, and sorbent of the SGN-30 grade [17]. After graphite processing, sludge remains, which is stored at the enterprise and subsequently either disposed of or partially recycled.

The purpose of this study was to investigate the composition and properties of graphite-containing sludge and to develop graphite-based coatings for casting molds.

Research methodology

The graphite-containing sludge used in this research was sourced from the gas purification aspiration system during the production of cryptocrystalline graphite (Fig. 1).

The elemental and phase compositions of the sludge were assessed using an XRD-7000 *X*-ray diffractometer (Shimadzu, Japan) [18]. The elemental composition of the sludge particles was also determined through energy-dispersive microanalysis, using an energy-dispersive spectrometer from Oxford Instruments (UK), mounted on the column of a JSM-7001F scanning electron microscope (JEOL, Japan) [19]. The spectra of cha-

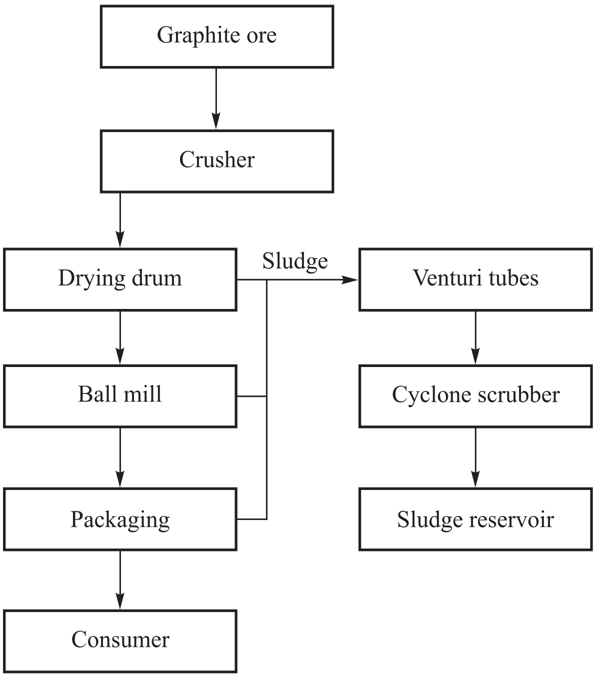

Fig. 1. Schematic of cryptocrystalline graphite production at JSC “Krasnoyarskgrafit”

Рис. 1. Схема производства скрытокристаллического графита на предприятии «АО Красноярскграфит» racteristic *X*-ray emissions from the chemical elements present in the powders were determined at specific points.

The size and total surface area of the sludge particles, as well as their size distribution, were analyzed using the light-scattering method with the Fritsch Analysette 22 MicroTec PLUS laser particle size analyzer (Germany).

The graphite-containing sludge was tested as part of a self-drying composite coating [20; 21].

The properties of the coatings were determined according to GOST 17022–78. The thickness of the cover layer and the depth of the penetrating layers were measured using an Observer.D1m microscope (Carl Zeiss, Germany), and the burn-on level was evaluated using the step test described in [22].

Results and discussion

The elemental composition of the sludge (wt. %) assessed using the XRD-7000 *X*-ray diffractometer is presented below:

O	26.00	S	1.95
C	45.85	Si	13.10
H	0.24	Mg	4.51
Na	0.61	Ca	5.10
Cl	0.94	Fe	1.70

The elemental composition of the sludge particles was also determined using the JSM-7001F scanning electron microscope, and the results are shown in Fig. 2.

The obtained data indicate that the sludge is mainly composed of carbon, sulfur, sodium, aluminum, and silicon.

The phase composition of the sludge (Table 1) includes graphite (up to 47 %), calcite (up to 13 %), pyrite (up to 4 %), quartz (up to 21 %), halite (up to 2 %), with other impurities making up to 17 %.

The reduced pyrite content compared to natural graphite will help decrease burn-on defects on casting surfaces, as discussed in detail in [23]. Calcite, halite, and quartz are materials whose presence increases the coating's refractoriness (due to their high melting points) and prevents interaction between the melt and the molding mixture. Clay minerals (kaolinite, montmorillonite, etc.), present among other phases in the sludge, will act as binders, providing the coatings with higher strength.

The sludge is a dispersed material with an average particle size of 3.64 µm and a total surface area of 36,506 cm^2/cm^3. The study of particle size distribution showed that the majority of particles fall within the range of 1–8 µm (Fig. 3).

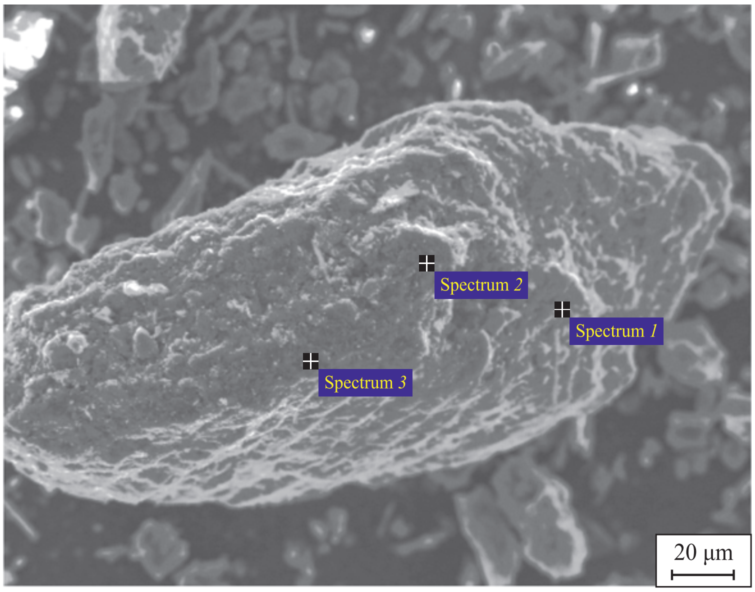

Spectrum	C	O	Na	Mg	Al	Si	Cl	K	Ca	Fe
1	80.82	8.77	2.27	0.19	0.65	0.84	4.41	0.63	0.96	0.46
2	75.27	15.45	1.21	0.57	1.09	1.72	2.10	0.36	0.56	1.22
3	85.47	6.70	0.72	–	1.92	2.30	1.32	0.25	1.32	–

Fig. 2. Elemental composition (wt. %) of sludge particles

Рис. 2. Элементный состав (мас. %) частиц шлама

Table 1. **Phase composition of GLS-2 graphite and graphite-containing sludge**

Таблица 1. **Фазовый состав графита ГЛС-2 и графитсодержащего шлама**

Phase	Phase content, wt. %	
	GLS-2 graphite	Graphite-containing sludge
Graphite	67.23	43.0–46.56
Quarz	9.99	20.12–21.05
Calcite	10.60	11.70–12.70
Pyrite	4.72	3.65–3.79
Halite	4.37	1.56–1.57
Other inclusions (kaolinite, montmorillonite, etc.)	3.09	17.10–17.20

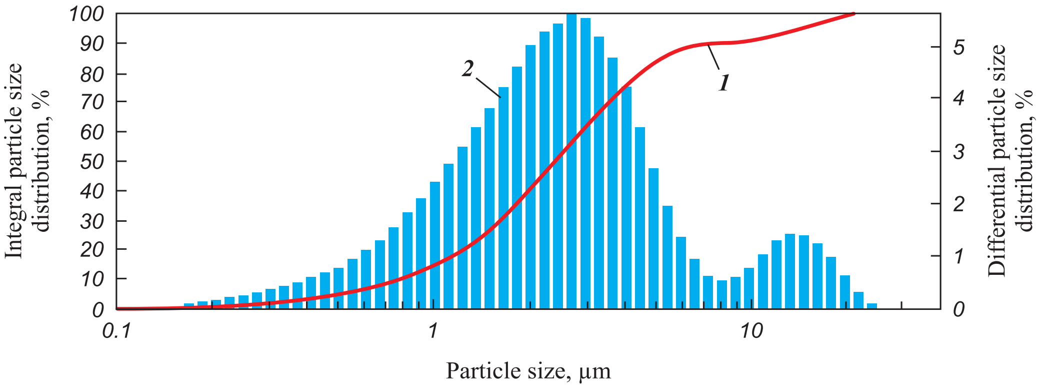

Fig. 3. Fractional composition of the sludge

1 – integral particle distribution; *2* – differential particle distribution

Рис. 3. Фракционный состав шлама

1 – интегральное распределение частиц; *2* – дифференциальное

Morphological analysis of the particles (Fig. 4) revealed that the sludge contains particles of various sizes and shapes, ranging from irregular to isometric.

The majority of the material is uniform, but there are large graphite aggregates and cylindrical inclusions. Smaller dispersed particles are observed on the surface of larger particles. Large inclusions can reach sizes of ≥1 mm. The cylindrical inclusions are impurity phases.

The analysis of the sludge structure showed that its parameters correspond to the hexagonal form of graphite. This suggests that the sludge can be recommended

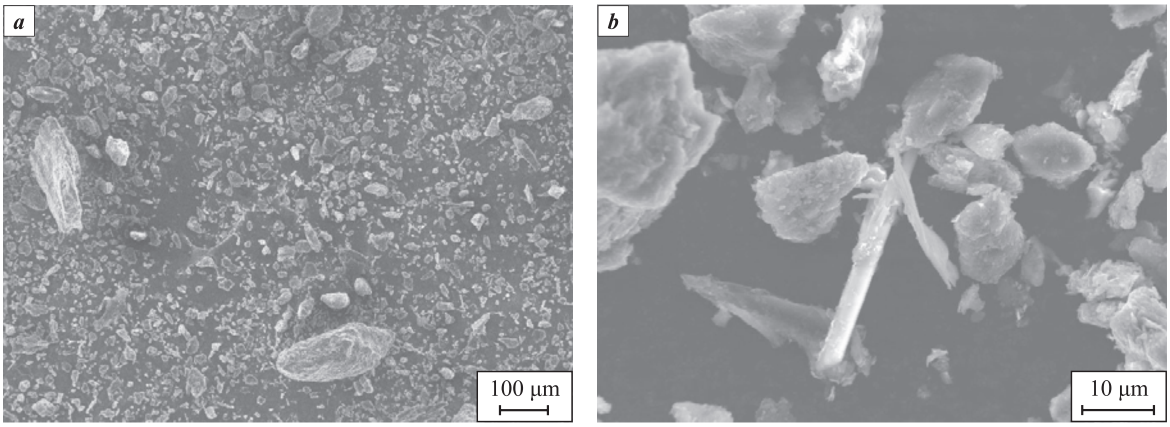

Fig. 4. Sludge images from the JSM-7001F microscope

Рис. 4. Съемки шлама на микроскопе JSM-7001F

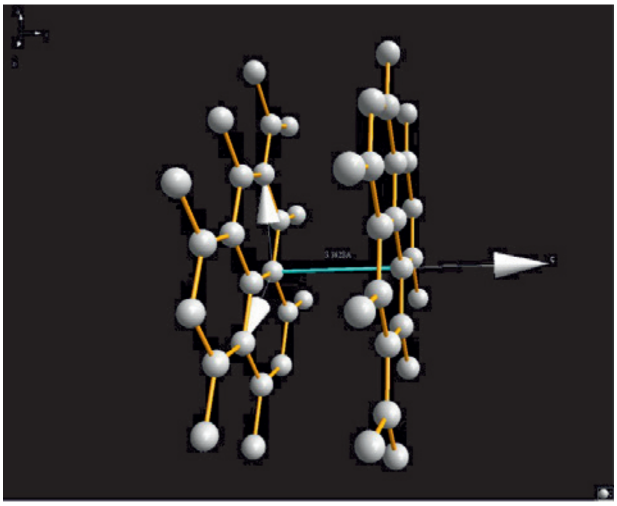

Fig. 5. Simulated graphite structure in the TOPAS 3 program

Рис. 5. Смоделированная структура графита в программе TOPAS 3

for use in composite coatings, provided the large graphite aggregates and cylindrical impurities are removed by sieving. Fig. 5 presents a 3D model of the graphite structure, simulated in the TOPAS 3 program.

The study examined the feasibility of using graphite-containing sludge in the composition of anti-burn coatings for cast iron casting.

To study the thickness of the covering and depth of the penetrating layers of the coating, a cold-setting mixture with the following composition (wt. %) was used: 97.2 – quartz sand $2K_1O_303$; 2.4 – alphabond resin; 0.4 – T-01 hardener. The working life of this mixture is 3.2 min, and the tensile strength (after 1 h) is 0.19 MPa.

The properties of composite anti-burn coatings based on graphite-containing sludge are shown in Fig. 6.

The composite coating based on graphite-containing sludge has a higher density and requires addi-

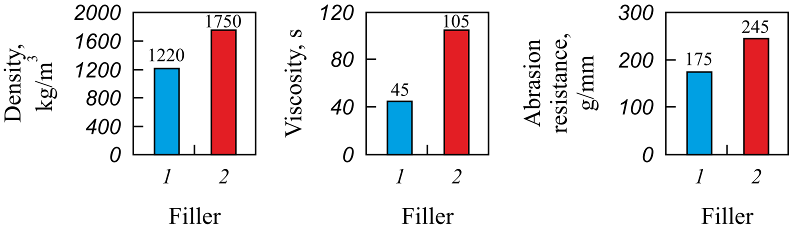

Fig. 6. Properties of anti-burn coatings based on GLS-2 graphite (*1*) and graphite-containing sludge (*2*)

Рис. 6. Свойства противопригарных покрытий на основе графита ГЛС-2 (*1*) и графитсодержащего шлама (*2*)

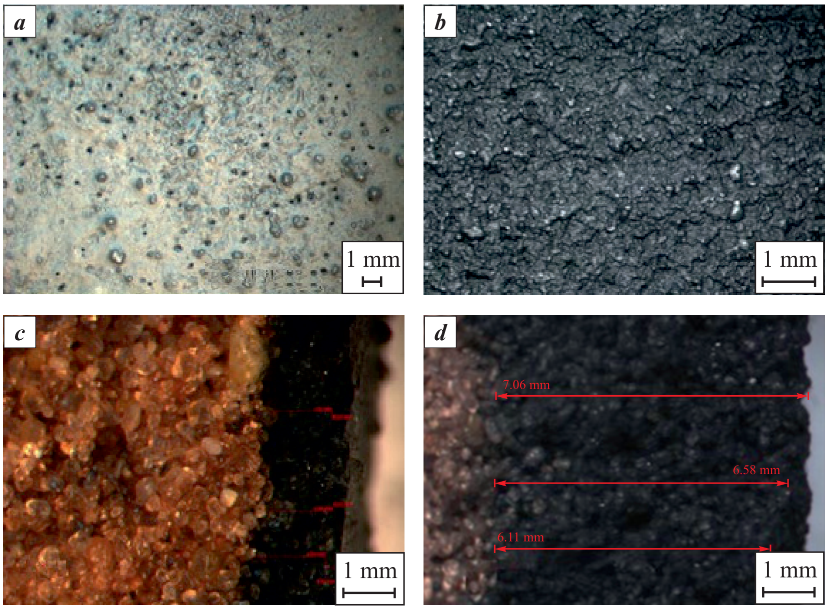

Fig. 7. Covering (***a***, ***b***) and penetrating (***c***, ***d***) layers of the coating
a, ***c*** – natural GLS-2graphite; ***b***, ***d*** – graphite-containing sludge

Рис. 7. Покровный (***a***, ***b***) и проникающий (***c***, ***d***) слои покрытия
a, ***c*** – природный графит ГЛС-2; ***b***, ***d*** – графитсодержащий шлам

tional dilution with PVB lacquer, which may reduce the sludge content.

The thickness of the covering and the depth of the penetrating layers of the coating are shown in Figs. 7 and 8.

The composite coating based on graphite-containing sludge does not form a covering layer, while the depth of the penetrating layer can reach 6.0–6.5 mm. This is because the sludge particles (~3.6 μm) are significantly smaller than the pores of the mold (~230 μm, Fig. 9).

In the study of burn-on magnitude on casting surfaces, a step sample was used. A cold-setting mixture was selected for the research.

During the tests at a temperature of 1400 °C, gray cast iron of the SCH20 grade was poured, with the following composition (wt. %):

C	2.90–2.97	Ni	0.084–0.086
Mn	0.92–0.93	Cu	0.12–0.13
P	0.019–0.021	V	0.049–0.052
S	0.042–0.044	Ti	0.021–0.024
Cr	0.10–0.11	Sn	<0.01
Si	2.41–2.60		

The effect of casting wall thickness on burn-on magnitude is shown in Tables 2 and 3.

When graphite is replaced with graphite-containing sludge in the coating, the average burn-on thickness on the casting surfaces decreases. This is due to changes in the phase composition and the smaller particle size of the sludge, which oxidizes more quickly during the heating of the mold surface layers, creating a reducing atmosphere.

However, the variation in burn-on values is significantly higher in the case of graphite-containing sludge. This is due to the higher sulfur content in the form of pyrite, which contributes to an increase in burn-on thickness.

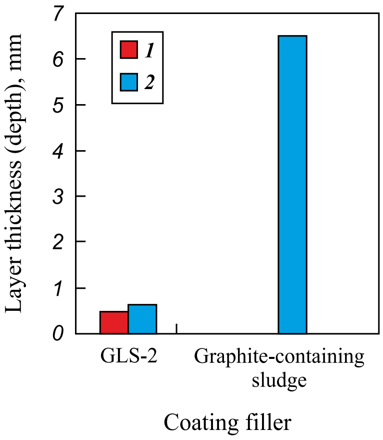

Fig. 8. Thickness of the covering (***1***) and depth of the penetrating (***2***) layers of anti-burn coating

Рис. 8. Толщина покровного (***1***) и глубина проникающего (***2***) слоев противопригарного покрытия

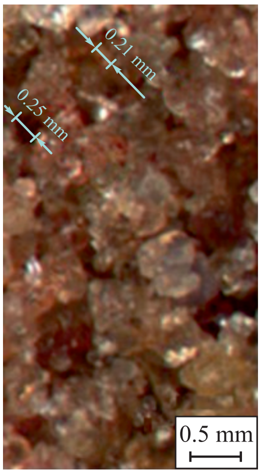

Fig. 9. Pores of the mold

Рис. 9. Поры формы

Thus, the results indicate that it is not possible to completely replace natural graphite in the composite coating with graphite-containing sludge. Therefore,

Table 2. **Burn-on thickness on the surface of castings obtained using coatings based on GLS-2 graphite**

Таблица 2. **Значение толщины пригара на поверхности отливок, полученных с применением покрытий на основе графита ГЛС-2**

Casting wall thickness, mm	Casting side	Burn-on thickness, μm			
		minimum	maximum	average	standard deviation
25	Side	40.77	66.31	53.54	9.09
	Bottom	39.88	171.71	105.80	42.55
50	Side	60.77	170.81	115.79	49.98
	Bottom	64.71	265.97	165.34	70.04
75	Side	78.77	223.83	151.30	55.44
	Bottom	82.56	276.84	179.70	82.07

Table 3. **Burn-on thickness on the surface of castings obtained using coatings based on graphite-containing sludge**

Таблица 3. **Значение толщины пригара на поверхности отливок, полученных с применением покрытий на основе графитсодержащего шлама**

Casting wall thickness, mm	Casting side	Burn-on thickness, μm			
		Minimum	Maximum	Average	Standard deviation
25	Side	1.20	69.10	15.98	26.28
	Bottom	10.37	180.03	66.80	51.85
50	Side	4.02	190.72	49.83	66.21
	Bottom	13.02	270.01	64.97	91.03
75	Side	15.46	353.83	95.36	118.63
	Bottom	32.58	420.25	128.94	132.17

further research is required to explore the partial replacement of natural graphite with graphite-containing sludge.

Conclusion

This study has demonstrated the potential for using graphite-containing sludge from the gas purification aspiration system in cryptocrystalline graphite production as part of composite anti-burn coatings. The results of the sludge's elemental composition analysis show that it consists of carbon, sulfur, sodium, aluminum, and silicon. The phase composition of the sludge includes graphite (up to 47 %), calcite (up to 13 %), pyrite (up to 4 %), quartz (up to 21 %), halite (up to 2 %), and other impurities (up to 17 %). The sludge is a dispersed material with an average particle size of 3.64 μm (total surface area – 36,506 cm^2/cm^3); most particles range from 1 to 8 μm. The sludge contains particles of various shapes: the bulk of them measure between 1 and 8 μm, with shapes ranging from irregular to isometric. Larger isometric particles can reach sizes of 1 mm or more. Smaller dispersed particles are present on the surfaces of larger particles. Acicular impurity phases are also present in the sludge. Analysis of the sludge's parameters indicates that it can be used in composite coatings, provided that large graphite aggregates and cylindrical impurities are removed by sieving. In composite anti-burn coatings where natural graphite is replaced with sludge, it is possible to increase the density from 1220 to 1750 kg/m^3, viscosity from 34 to 105 s, and relative strength from 175 to 245 g/mm. However, due to the high dispersity of the sludge, the coating completely penetrates the pores of the sand-resin mold mixture without forming a surface layer. With complete replacement of graphite with graphite-containing sludge in the coating, the average burn-on thickness on the surface of the castings decreases, depending on the wall thickness, from 53.54–151.30 to 15.98–95.36 μm (on the side surface of the castings) and from 105.80–179.70 to 66.80–128.94 μm (on the bottom surface of the castings). However, the variation in burn-on thickness is significantly higher, which is attributed to the higher sulfur content in the graphite-containing sludge, contributing to increased burn-on thickness. Therefore, further research should focus on the partial replacement of graphite with graphite-containing sludge, which would reduce the cost of the coatings and improve the quality of cast iron products.

References / Список литературы

1. Yakovleva E.A. Opportunities and barriers of a cyclical economy in government regulation. In: *Mechanisms of development of socio-economic systems of the region:* Collection of articles of the 12th International Scientific and Practical Conference (18 April 2019). Voronezh: Volmi, 2019. P. 57–61. (In Russ.).

Яковлева Е.А. Возможности и барьеры циклической экономики в государственном регулировании. В сб.: *Механизмы развития социально-экономических систем региона:* Сб. статей 12 междунар. науч.-практ. конференции (18 апреля 2019 г.). Воронеж: Волми, 2019. С. 57–61.

2. Romanova O.A., Sirotin D.V. Environmental and economic efficiency of recycling industrial waste in the Urals. *Economy of Regions*. 2021;17(1):59–71. (In Russ.). https://doi.org/10.17059/ekon.reg.2021-1-5

Романова О.А., Сиротин Д.В. Методы определения эколого-экономической эффективности переработки техногенных образований Урала. *Экономика региона*. 2021;17(1):59–71. https://doi.org/10.17059/ekon.reg.2021-1-5

3. Gilmanshina T.R., Kovaleva A.A., Khudonogov S.A., Kritsky D.Yu. Use of graphite-containing sludge in the composition of non-stick coatings. *Chernye Metally*. 2022;(4):23–26. (In Russ.). https://doi.org/10.17580/chm.2022.04.04

Гильманшина Т.Р., Ковалева А.А., Худоногов С.А., Крицкий Д.Ю. Использование графисодержащего

шлама в составе противопригарных покрытий. *Черные металлы*. 2022;(4):23–26.
https://doi.org/10.17580/chm.2022.04.04

4. Federal law of 21 July 2014, No. 219-FZ “On amendments to the Federal law “On environmental protection” and certain legislative acts of the Russian Federation” (as amended and supplemented on 26 July 2019). (In Russ.).

   Федеральный закон от 21.07.2014 г. № 219-ФЗ «О внесении изменений в Федеральный закон «Об охране окружающей среды» и отдельные законодательные акты Российской Федерации» (с изм. и доп. от 26 июля 2019 г.).

5. Vlasova V.V., Fomina E.Yu. The technology of the processing CHP-plant ash and slag wastes with obtaining ferrous raw materials for iron and steel industry. *Chernye Metally*. 2019;(7):67–72. (In Russ.).

   Власова В.В., Фомина Е.Ю. Технология переработки золошлаковых отходов ТЭС с получением железосодержащего сырья для черной металлургии. *Черные металлы*. 2019;(7):67–72.

6. Lee W.-H., Wu Y.-F., Ding Y.-C., Cheng T.-W. Fabrication of ceramic moulds using recycled shell powder and sand with geopolymer technology in investment casting. *Applied Sciences*. 2020;10(13):4577.
https://doi.org/10.3390/app10134577

7. Moiz Khan M., Jadhav G.N., Mahajani S.M., Singh M. Comparative study of waste foundry sand reclamation techniques. In: *Proceedings of 73rd World Foundry Congress WFC 2018* (Poland, Krakow, 23–27 September 2018). Poland, Krakow, 2018. P. 119–120.

8. Drozyński D., Bobrowski A., Holtzer M. Influence of the reclaim addition on properties of moulding sands with the geopol binder. *Archives of Foundry Engineering*. 2015;15(1):138–142.
https://doi.org/10.1515/afe-2015-0025

9. Kvashevaya E., Ushakova E., Ushakov A. Carbon-containing waste of coal enterprises in magnetic sorbents technoligy. *E3S Web of Conferences*. 2017;21:01003.
https://doi.org/10.1051/e3sconf/20172101003

10. Kuz’min M.P., Larionov L.M., Kondratiev V.V., Kuz’mina M.Yu., Grigoriev V.G., Kuz’mina A.S. Use of the burnt rock of coal deposits slag heaps in the concrete products manufacturing. *Construction and Building Materials*. 2018;179:117–124.
https://doi.org/10.1016/j.conbuildmat.2018.05.222

11. Taha Y., Benzaazoua M., Hakkou R., Mansori M. Coal mine wastes recycling for coal recovery and eco-friendly bricks production. *Minerals Engineering*. 2017;107:123–138.
https://doi.org/10.1016/j.mineng.2016.09.001

12. Agrawal A., Sahu K.K., Pandey B.D. Solid waste management in non-ferrous industries in India. *Resources, Conservation and Recycling*. 2004;42(2):99–120.
https://doi.org/10.1016/j.resconrec.2003.10.004

13. Yildiz T.D., Tombal T.D. Challenges and recovery opportunities in waste management during the mining and enrichment processes of ores containing uranium and thorium – A review. *Gospodarka Surowcami Mineralnymi – Mineral Resources Management*. 2024;40(1):25–62.
https://doi.org/10.24425/gsm.2024.149305

14. Bagryantsev V.I., Kazimirov S.A., Kutsenko A.I., Podolskiy A.P., Rybushkin A.A., Temlyancev M.V. The practice and prospects of using solid carbon-containing waste as fuel for thermal power units. *Bulletin of the Siberian State Industrial University*. 2013;3(5):33–37. (In Russ.).

    Багрянцев В.И., Казимиров С.А., Куценко А.И., Подольский А.П., Рыбушкин А.А., Темлянцев М.В. Практика и перспективы использования твердых углеродсодержащих отходов в качестве топлива для теплоэнергетических агрегатов. *Вестник Сибирского государственного индустриального университета*. 2013;3(5):33–37.

15. Fadeeva N.V., Orekhova N.N., Gorlova O.E. Experience of graphite-containing dust of metallurgycal plants processing. *Ferrous Metallurgy. Bulletin of Scientific*. 2019;75(5):632–640. (In Russ.).
https://doi.org/10.32339/0135-5910-2019-5-632-639

    Фадеева Н.В., Орехова Н.Н., Горлова О.Е. Опыт переработки графитсодержащей пыли металлургического производства. *Черная металлургия. Бюллетень научно-технической и экономической информации*. 2019;75(5):632–640.
https://doi.org/10.32339/0135-5910-2019-5-632-639

16. Mulyavko V.I., Oleinik T.A., Lyashenko V.I., Oleinik M.O. The improvement in the efficiency of the utilization of the graphite containing dust formed in the metallurgical production. *Ferrous Metallurgy. Bulletin of Scientific*. 2015;(11):67–76. (In Russ.).

    Мулявко В.И., Олейник Т.А., Ляшенко В.И., Олейник М.О. Повышение эффективности утилизации графитсодержащей пыли металлургического производства. *Черная металлургия. Бюллетень научно-технической и экономической информации*. 2015;(11):67–76.

17. Company “KrasnoyarskGrafit”. URL: https://www.graphite-ore.com/en/ (accessed: 08.04.2024).

18. Shimadzu. Excellence in Science. URL: https://www.shimadzu.ru (accessed: 08.04.2024).

19. Product Jeol. URL: https://jeol.com (accessed: 08.04.2024).

20. Amelchenko V.N., Illarionov I.E., Gilmanshina T.R., Borisyuk V.A. Graphite as a prospective material for metallurgical application. *CIS Iron and Steel Review*. 2018;16:29–32.
https://doi.org/10.17580/cisisr.2018.02.06

21. Illarionov I.E., Gilmanshina T.R., Kovaleva A.A., Bratukhina N.A. Understanding the effect of structural defects in graphite on the properties of foundry coatings. *CIS Iron and Steel Review*. 2018;16:63–66.
https://doi.org/10.17580/cisisr.2018.02.13

22. Illarionov I.E., Kaftannikov A.S., Nuraliev F.A., Gilmanshina T.R. Evaluation of burn value on surface of iron castings. *Chernye Metally*. 2018;(8):23–28.

    Илларионов И.Е., Кафтанников А.С., Нуралиев Ф.А., Гильманшина Т.Р. Оценка величины пригара на поверхности чугунных отливок. *Черные металлы*. 2018;(8):23–28.

23. Gilmanshina T.R., Dubova I.V., Vasyunina N.V., Kovaleva A.A. Analysis of physical-chemical processes occurring on the boundary between the melt and non-stick coating. *CIS Iron and Steel Review*. 2021;21:38–42.
https://doi.org/10.17580/cisisr.2021.01.06

Сведения об авторе

Сергей Александрович Худоногов – ст. преподаватель кафедры прикладной механики Политехнического института Сибирского федерального университета
ORCID: 0009-0007-1740-2021
E-mail: shudonogov@sfu-kras.ru

Information about the Author

Sergei A. Khudonogov – Senior Lecturer, Departament of applied mechanics, Polytechnic Institute, Siberian Federal University
ORCID: 0009-0007-1740-2021
E-mail: shudonogov@sfu-kras.ru

Статья поступила 08.04.2024 г.
Доработана 04.07.2024 г.
Принята к публикации 09.07.2024 г.

Received 08.04.2024
Revised 04.07.2024
Accepted 09.07.2024

Зарегистрирован Федеральной службой по надзору
в сфере связи, информационных технологий
и массовых коммуникаций.
Свидетельство о регистрации **ПИ № ФС77-79230**

Журнал распространяется агентством «Урал-Пресс»
Подписной индекс: 80752 (печатная версия)
05108 (электронная версия)